Title	Study on the planetary lightning detection based on the development of dual-band photometer installed at ground telescope and its data analysis
Author(s)	大野, 辰遼
Degree Grantor	北海道大学
Degree Name	博士(理学)
Dissertation Number	甲第16746号
Issue Date	2026-03-25
DOI	https://doi.org/10.14943/doctoral.k16746
Doc URL	https://hdl.handle.net/2115/99591
Type	doctoral thesis
File Information	Tatsuharu_Ono.pdf, 全文

博士学位論文

Study on the planetary lightning detection based on the development of dual-band photometer installed at ground telescope and its data analysis
(地上望遠鏡搭載二波長同時測光観測装置の開発とデータ解析に基づく惑星雷検出に関する研究)

Ono Tatsuharu
大野辰遼

北海道大学大学院理学院
宇宙理学専攻

2026 年 03 月

Abstract

Planetary lightning observations can serve as a valuable source of information for planetary atmospheric research, providing insights into convective activity associated with cumulonimbus clouds, atmospheric composition, and volcanic activity. However, the light curves and time constants of lightning discharges on Venus and Jupiter remain unexplained, and their precise occurrence frequency and discharge scale remain undetermined. On Jupiter, spacecrafts like Galileo observed deep lightning discharges of approximately 10^9 J occurring at an altitude where the atmospheric pressure is 5 bar. However, due to the long exposure times measured in seconds, it remains unclear whether these represent a single large-scale discharge or a series of lightning events comparable in scale to the 10^7 J lightning observed at higher altitudes by Juno. Ground-based observations also struggle to detect lightning and estimate its occurrence frequency, as Jupiter's dayside light obscures it. On Venus, there is still no consensus on whether Venusian lightning even exists. Although the LAC onboard the Akatsuki recorded long-duration light curves exceeding 50 msec, and ground-based telescopes observed images of lightning discharges on Venus's nightside, constraints on exposure time and sample size mean it remains inconclusive whether these observations captured scattered light from short-duration discharges lasting hundreds of microseconds or from long-duration discharges lasting hundreds of milliseconds. Thus, the lack of information on the light curves and time constants of Jupiter and Venus lightning prevents the accurate determination of lightning discharge energy and occurrence frequency, making it difficult to elucidate charge-separation mechanisms and to conduct comparative studies with meteorological parameters.

The purpose of this study is to detect lightning discharges on Venus and Jupiter through photometric curve observations. Therefore, we newly developed a photometric observation device (PLD) with a time resolution of 2 msec, surpassing the 50 msec exposure time of CCDs mounted on ground-based telescopes in previous studies, and installed it on the 1.6-meter Pirka Telescope owned by Hokkaido University. The PLD simultaneously recorded photometric curves at two wavelengths. It used their waveform correlation to enable high-precision discrimination between daytime background light and noise versus lightning flashes. That is not easy with a single wavelength. Assuming that statistical noise follows a normal distribution, we extracted signals exhibiting statistically significant deviations (4σ or greater). To analyze the observed waveforms, we developed a new three-dimensional light-scattering model that incorporates distributions of cloud particle size and composition. In this model, we reproduced the light curves by incorporating, for the first time, the time-delay process of photon scattering within cloud structures, based on the vertical cloud particle number density and size distribution estimated from numerical simulations of Jupiter's cumulonimbus clouds and typical Venusian clouds. These results were compared with Earth lightning observation data from the JEM-GLIMS instrument aboard the International Space Station (ISS) to verify the model's validity and to examine the time constants and characteristics of lightning discharges in interplanetary space.

First, we evaluated the reproducibility of the lightning luminous intensity curve using

the model developed in this study by applying it to lightning on Earth. The typical FWHM value for the Earth's lightning light curve was approximately 5 msec. For lightning strikes where the discharge type could be identified, the duration was approximately 0.6 msec. The Earth model of this study reproduced a light curve with an average summer thunderstorm occurrence altitude of 2 km and a full width at half maximum (FWHM) of approximately 0.6 msec. The FWHM of the light curve in this model was consistent with typical observational values. Comparing the waveform shapes of the model and the observed results yielded a high correlation coefficient of 0.98. Furthermore, the model showed a trend consistent with observations of the relationship between the altitude of lightning occurrence, as suggested by JEM-GLIMS imaging data, and the FWHM of the light curve. Based on the above results, we confirmed that the model developed in this study possesses a certain degree of validity in reproducing the photoluminescence curve of lightning.

On Venus, we compared PLD observations with model results and examined the long-duration light curves of 50 msec reported in previous studies. We observed Venus for 8 nights in 2022, totaling approximately 300 minutes by PLD. The observation results identified four events exceeding 4.8 times the standard deviation σ in the peak value of the lightning observation wavelength light curve, which were considered lightning candidates. The FWHM of these event waveforms was a spike-like waveform with a time resolution of 2 msec or less on the PLD. Although we were unable to perform waveform comparisons with the Venus model used in this study, the results were consistent with the light curve, which shows a maximum FWHM of 1.5 msec at altitudes above 10 km on Venus. The energy of the spike-shaped waveform was approximately 10^9 J, consistent with previous studies. The frequency of detected events was approximately twice that of lightning occurrence rates suggested in previous studies based on ground-based telescope observations and of the same order of magnitude. Even considering cosmic ray-induced waveforms, the energy level was sufficiently high, and based on the comparison of the two wavelengths, the possibility of it being a meteorite was low. Observations and modeling in this study suggest that the typical time constant for Venusian lightning is less than 2 msec. This time constant is significantly shorter than the 50 msec FWHM observed by LAC. Using this model to explain LAC observations as scattered light from single discharges lasting hundreds of microseconds revealed that a cloud density 700 times the nominal value would be required. Given the range of fluctuations in number density inferred from prior infrared observations and the required energy of the light source, it was difficult to explain the LAC observations solely in terms of cloud scattering. According to data from Earth's JEM-GLIMS, lightning with a time constant of 50 msec or longer accounted for 4% of the measured results. Among these, the identified lightning discharge type was cloud-to-ground positive-polarity discharge (+CG). +CG may exhibit a sustained luminous duration of several hundred milliseconds due to a continuous discharge current known as spider lightning. Based on the above, the waveform observed by LAC was not typical lightning but instead suggested the possibility of a prolonged discharge.

On Jupiter, we compared PLD observations with model results and examined 10^9 J class lightning discharges observed in previous studies. PLD observed Jupiter for 26 nights, totaling approximately 880 min, in 2021 and 2022. Observations detected multiple events in the lightning observation wavelength photometric curve, with peak values exceeding 5.2σ. These event waveforms had a full width at half maximum (FWHM) of approximately 3.5 msec and a peak value of about 10^9 J. The observed FWHM was 0.4 times the maximum FWHM of 8 msec in the light curve of the cumulonimbus structure according to this model. In comparison, it was 1.8 times the maximum FWHM of 2 msec in the light curve of the typical Jupiter cloud structure. If we assumed a discharge time of approximately 1 msec, which we did not consider in this model, the time constant of the scattered light would increase accordingly. Therefore, the lightning with an energy of 10^9 J can be interpreted as either lightning flashes generated deep within the early cumulonimbus cloud or light leakage from a region of thin optical thickness within the developing cumulonimbus cloud or from the cloud around the cumulonimbus. Furthermore, the estimated occurrence frequency of 10^9 J class lightning events from this observation was lower than that reported in previous studies. We considered that the low detection count was more due to constraints in the detection threshold settings than to the local time dependence of Jupiter's lightning occurrence frequency. The local time of 12:00 observed by the PLD corresponds to a period when lightning occurrence frequency decreases on Earth. However, previous radio observations have not indicated a strong local time dependence in the occurrence frequency of Jupiter lightning. Therefore, the low number of detections was not due to a decrease in lightning occurrence frequency. Instead, since observations of Jupiter from Earth can only capture its daytime side, we had no choice but to set the detection threshold high to prevent signals from being buried in noise. When we set the event detection threshold to 4.5σ, the detection frequency became comparable to that of previous studies. Furthermore, the statistically low number of waveform detections observed with the PLD this time suggested that Jupiter's 10^9 J lightning event may have produced a prolonged light curve. That is, even with high total energy, if the peak luminosity falls below the PLD's sensitivity, we estimated that the time constant would extend to 13 msec or longer. This understanding is consistent with previous radio observations, which detected approximately 10 lightning discharges within 16 msec. It suggests that lightning with energies exceeding 10^9 J may not be a single discharge, but rather multiple overlapping discharges in the 10^7 to 10^8 J range.

Acknowledgement

First and foremost, I express my deepest gratitude to my supervisor, Professor Yukihiro Takahashi, for his invaluable guidance, patient mentorship, and constant encouragement throughout my doctoral studies. His profound insights into Planetary science and rigorous approach to scientific inquiry have fundamentally shaped my development as a researcher. I am truly grateful for the freedom he gave me to explore my research interests while providing the necessary direction to keep this project on track.

I also extend my sincere thanks to Professor Mitsuteru Sato, Lecturer Seiko Takagi, and Specially Appointed Associate Professor Hisayuki Kubota for their insightful comments and constructive criticism during our group seminars. Their expertise in lightning, Meteorology, and observational works was instrumental in refining this study. I am deeply grateful for the many instructions by Professor Kiyoshi Kuramoto, Professor Masaki Ishiwatari, and Associate Professor Shunichi Kamata.

Special thanks go to the senior members of the laboratory, especially Dr. Masataka Imai. I am deeply indebted to them for teaching me the fundamentals of observational data analysis and planning when I first joined the group. Their willingness to share their knowledge and engage in late-night discussions saved me from numerous technical deadlocks. My life in the laboratory would not have been the same without my wonderful colleagues and friends. In particular, I want to thank Mr. Ko Hamamoto, Ms Yuki Futamura, Mr. Yuki Sato, Mr. Haruki Sugiyama, and the Pirka telescope team. We have shared countless hours of struggle and joy. These shared experiences gave me the emotional resilience to complete this study.

I am also grateful to the staff and researchers at the Nayoro City Observatory, including the following people: Mr. Yasuo Sano, the ex-director of the observatory; Mr. Yasuhiko Murakami, the director of the observatory; Mr. Fumitake Watanabe; Dr. Hiroyuki Naito; Ms. Yuko Kato; and Mr. Ryoma Nagayoshi. Access to the facility and the technical support provided were essential for the success of my research. The collaborative environment and the opportunity to interact with experts from different backgrounds greatly broadened my scientific perspective.

Finally, I would like to express my heartfelt appreciation to my family. To my parents, thank you for your unconditional love and for supporting my education over many years without hesitation. Your belief in my potential has been my greatest source of strength. Thank you for being a constant source of joy and for reminding me of the world beyond my research. This thesis is as much a result of your support as it is of my own efforts.

Contents

List of Tables

List of Figures

1 Introduction

1.1 Lightning and Transient Luminous Event (TLE)

Lightning is an electrical discharge phenomenon associated with atmospheric activity. Most lightning occurs within cumulonimbus clouds. Cumulonimbus clouds develop as a result of moist convection in the atmosphere. Atmospheric air containing condensable components, such as water vapor, is transported upward by convective updrafts. Then they condense into raindrops and ice crystals that become cloud particles. The size of cloud particles increases as condensation continues. If cloud particles reach a certain size, they fall due to their own weight. Collisions between descending and ascending cloud particles cause the transfer of electric charge between their surfaces. Cloud particles become fixed to a specific polarity of charge depending on their chargeability. The separation of charged cloud particles into the upper and lower regions of the cumulonimbus creates charge separation. This charge separation creates localized charge instability. To resolve this charge instability, charge transfer occurs, leading to lightning discharges. Recent studies have advanced our understanding of the correlation between lightning and cumulonimbus cloud activity on Earth (e.g., Belo-Pereira (2025)) and its relationship with typhoons (e.g., LIN et al. (2025)), revealing these correlations. The more active the convective activity becomes, the greater the intensity and frequency of lightning. Lightning and electrically charged cloud particles are closely related to convection.

Lightning discharge involves several steps. First, a phenomenon called step leader discharge occurs, creating a discharge path. The step leader begins when the electric field generated by charge separation exceeds the atmospheric breakdown threshold, partially breaking the air's insulation. After the initial discharge persists for a certain time, a highly conductive plasma channel begins to propagate from the charged region within the cloud. It advances toward the opposite charged body in a step-like pattern, alternating between progression and pause, hence the name stepped leader. Next, the actual charge discharge, the return stroke, occurs. The return stroke is the instantaneous flow of current when the stepped leader makes direct contact with the charged body, or when the electric field generated by the charge within the stepped leader causes contact with a leader from the opposite charged body. When this return stroke discharge occurs between the ground and the cloud, it is called CG. Specifically, when positively polarized charge discharges, it is called +CG, and when negatively polarized charge discharges, it is called -CG. Discharges occurring within the cloud are classified as IC, and those occurring between clouds are classified as CC. The return stroke neutralizes the atmosphere charged to one polarity by the stepped leader. Consequently, an average current of 30 kA flows for 50 –100 µsec. Furthermore, if the charge in the cumulonimbus cloud cannot be neutralized in a single return stroke, the remaining charge potential difference causes charge transfer to occur again. After a certain period elapses and sufficient charge transfer occurs, the plasma channel advances similarly to the generation of the first stepped leader. At this point, the discharge path formed by the stepped leader advances without interruption. If electrical coupling occurs, multiple return strokes may occur along the same discharge path as the first return stroke. On average, the time interval between the first return stroke and subsequent return strokes is approximately 10 msec. Lightning discharges are complex processes and time-varying discharge phenomena.

Observations and research on the Transient Luminous Event (TLE) phenomenon as a discharge event have advanced, revealing its relationship with lightning discharges. The charge neutralized and dissipated by lightning discharges can secondarily generate a quasi-electric field in the mesosphere. This electric field, when exceeding the atmospheric breakdown critical value, causes the observed phenomenon called sprites, which emit light. Elves, luminous phenomena with diameters of several hundred kilometers in the ionosphere, have also been observed. Their formation mechanism is thought to involve electromagnetic pulses emitted by vertical currents flowing during lightning strikes. When these pulses reflect off the lower ionosphere, they cause atmospheric breakdown, resulting in the observed light. Additionally, phenomena occurring in the stratosphere, including those called jets, are also classified as TLEs. It has been established that various luminous phenomena are generated by lightning.

Research on lightning and TLEs has advanced alongside improvements in observational instruments. Lightning discharges and TLEs can be observed using visible light and electromagnetic waves. Visible light is produced by intense luminous effects caused by Joule heating from the discharge. The atmosphere acts as an insulator, creating resistance during the discharge. The discharge path is extremely narrow, typically less than a few centimeters. A high current of 30 kA flows through this narrow discharge path. Consequently, the atmosphere heats up during discharge, reaching up to 30,000 K instantaneously on Earth. This superheated air emits visible light. While the emission is close to blackbody radiation with peaks across the visible spectrum, the bright emission lines depend on atmospheric composition since the light originates from atmospheric heating. On Earth, emission lines from oxygen and nitrogen appear in the 740 – 820 nm wavelength range. Conversely, lightning discharge light is absorbed by the atmosphere when occurring in the lower stratosphere or troposphere. Consequently, lightning discharge light is darkened by absorption near 762 nm by nitrogen molecules. On the other hand, since most TLEs occur in the mesosphere, they are less affected by atmospheric absorption. Observations using narrowband filters centered at 762 nm have been employed to distinguish high-altitude luminous phenomena like sprites from low-altitude emissions (Sato et al., 2015). The duration of the luminous phenomenon varies from several milliseconds to several seconds. The average is about 5 msec. This is due to various reasons, including multiple return strokes overlapping in multiple lightning events, longer discharge times, and cloud structures that scatter and absorb the light. Visible light observations of lightning enable the determination of discharge energy and the horizontal structure of the discharge. The relationship between light intensity and discharge current is claimed to be linear or close to quadratic, as reported in Quick & Krider (2013) and others. By determining the horizontal positions of lightning discharges and TLEs, it is possible to study how changes in the electromagnetic field generated by the discharge contribute to TLE occurrence. Since lightning emissions are affected by cloud scattering, confirming the scattered waveforms of lightning emissions also aids in elucidating cloud structures and discharge characteristics.

Electromagnetic waves generated by lightning discharge currents span a wide frequency range from 1 Hz to 1 GHz. The primary components are VLF (Very Low Frequency) in the 3 – 30 kHz band and ELF (Extremely Low Frequency) in the 1–100 Hz band. When generated near the strike point, these electromagnetic waves are observed as direct waves or ground waves. At distances exceeding several hundred kilometers, they propagate as a waveguide between the Earth's surface and the ionosphere or along the Earth's magnetic field lines. Electromagnetic wave observations primarily measure electric fields using field mills, monopole antennas, and loop antennas. Field mills observe changes in the electric field within the cloud immediately before a lightning strike, capturing the initial stages of the process. These changes exhibit magnitudes comparable to those observed in the return stroke as direct waves or reflected waves from the ground. High-frequency observation devices, such as monopole antennas, detect changes in the electric field generated by the stepped leader and return stroke. The stepped leader exhibits a bipolar pulse with a rise time of approximately 0.5 µsec. The return stroke produces a waveform with a rise time of a few µsec and a duration of about 10 µsec. Furthermore, it is possible to estimate different characteristics of lightning discharges depending on the observed frequency band(Salut et al. (2013)). VLF band observations have revealed that the amplitude of the observed signal is proportional to the peak discharge current. It is also considered to be in good proportional relation to the current waveform, which is the time variation of current, in the ELF band, and estimation of the current waveform is performed even in magnetic field observations. However, it should be noted that due to the presence of a time derivative term in Maxwell's equations for the electromagnetic field emitted by lightning discharges, the current waveform and the magnetic field waveform will differ.

Electromagnetic waves observed during thunderstorms exhibit characteristic waveforms known as Whistlers and Sferics. Whistlers are electromagnetic waveforms with a characteristic frequency-time characteristic, exhibiting a descending pitch pattern from high frequencies in the several kHz range to lower frequencies. They penetrate the ionosphere, propagate along the Earth's magnetic field lines above the ionosphere, and then re-penetrate the ionosphere to reach the Earth's surface. Sferics are electromagnetic waves that propagate thousands of kilometers without being absorbed by the ionosphere. They exhibit a spike-like waveform in their frequency-time characteristics, with frequencies ranging from several to several hundred kHz. Detecting these characteristic waveforms provides evidence of lightning occurrence, serving as a trigger for detection. The time difference allows for locating the lightning source. Since these waves are absorbed by the ionosphere, they are used for ionospheric research.

1.2 Exploration of planetary lightning

Lightning discharge is a widespread phenomenon beyond Earth. Similar investigations of visible light and electromagnetic waves, as conducted on Earth, have been carried out on other planets in our solar system, such as Venus and Jupiter.

1.2.1 Venus

Venus shares similar physical parameters with Earth, such as mass, size, and density. As an inner planet, Venus experiences dramatic changes in its phase angle relative to Earth and the Sun. From Earth, it is possible to observe the phases of Venus, specifically its illuminated and darkened sides. Unlike Earth, Venus is entirely shrouded in thick clouds. These clouds extend from an altitude of approximately 50 to 70 kilometers. Venus' clouds are thought to consist of approximately 96% H_2SO_4 raindrops. The primary constituent of Venus' atmosphere is carbon dioxide CO_2, with the remainder being N_2, CO, H_2, Ar, and SO_2. The potent greenhouse effect of CO_2 and the dense atmosphere cause Venus's surface temperature and atmospheric pressure to reach 700 K and 90 bar, respectively. Figure 1.1 shows the typical temperature profile and pressure distribution with altitude in Venus's atmosphere.

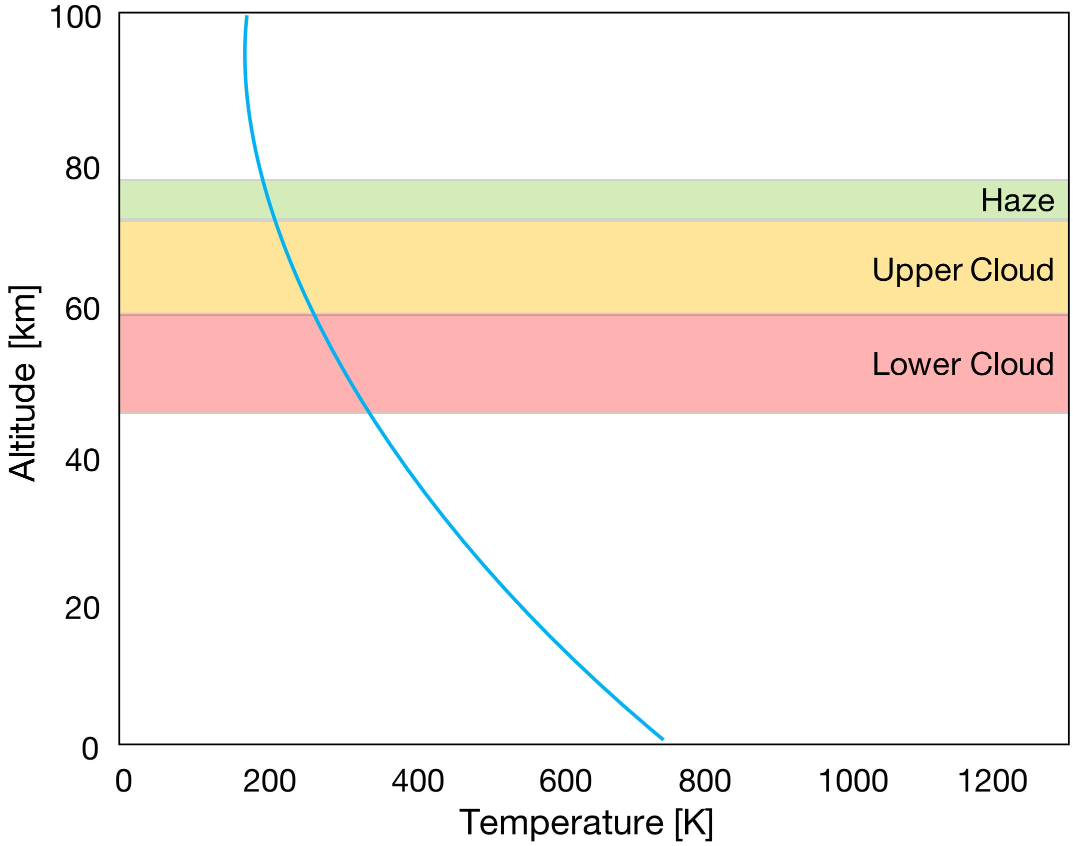

Figure 1.1: Vertical profiles of atmospheric temperature and cloud-haze structure on Venus. The blue solid line indicates the temperature profile as a function of altitude. The three shaded regions represent the vertical distribution of aerosols: the upper haze layer (above ∼70 km) (green), the main sulfuric acid cloud deck (∼ 47 – 70 km)(orange and red), distinguished by different colors.

Venus's troposphere lies near the surface, maintaining equilibrium through convection, with temperatures decreasing with altitude. Unlike Earth, which possesses an ozone layer, Venus's stratosphere lacks localized temperature increases and exhibits stable stratification. In regions near the cloud-top altitude where radiative equilibrium is established, photochemical reactions occur, and a haze layer is believed to exist.

Venusian lightning is thought to occur at altitudes of 60 km or less, below the altitude where its convective cells exist (Michael et al. (2009), Kumar et al. (2021)). Results from laboratory experiments replicating Venus's atmosphere in ground-based laboratories suggest Venusian lightning emits its brightest light at 777.4 nm, the emission line of carbon dioxide, the primary component of Venus's atmosphere (W. Borucki et al. (1996)). Furthermore, based on Pérez-Invernón et al. (2017), it is believed that when the energy of Venusian lightning discharges exceeds 10^{10} J, Transient Luminous Events (TLEs) such as sprites also occur in the ionosphere of Venus. Their wavelengths extend into the near-infrared region.

Venusian lightning has been observed using spacecrafts and ground-based telescopes. In visible light observations, there are earlier examples such as observations by the spectrometers aboard Venera 9 and Venera 10 (Krasnopolskii (1983), Krasnopolsky (1983)), Observations by the Pioneer Venus Orbiter's Star Tracker(W. J. Borucki et al. (1991), W. J. Borucki et al. (1981)), Observations using a silicon PIN diode light detector installed on both the Vega 1 and Vega 2 balloons (Sagdeev et al. (1986)), Observations by the CCD camera during the Galileo's flyby of Venus (Belton et al. (1991), W. Borucki et al. (1985)), Observations using a CCD camera mounted on a 1.54-meter aperture reflecting ground-based telescope (Hansell et al. (1995)), Observations by the Near-Infrared Spectrometer onboard the Venus Express (Cardesín Moinelo et al. (2016)), Observations by the LAC instrument onboard the Akatsuki (Takahashi et al. (2020)), Near-infrared observations at 2.2 μm using the IR2 instrument onboard the Akatsuki (Ksanfomality (2024)).

Observations of electromagnetic waves include examples such as measurements of the magnetic field by Venera 11, 12, 13, and 14, and observations using acoustic sensors (Ksanfomaliti et al. (1980), Ksanfomaliti et al. (1982), Ksanfomaliti et al. (1983)), Observations using the 100 Hz electric field meter onboard Pioneer Venus(Scarf et al. (1987), Scarf et al. (1980)), Electric Field Sensor during the Venus Flyby of the Galileo (Gurnett et al. (1991)), Electric Field Sensor during the Cassini's Venus Flyby(Gurnett et al. (2001)), Observations by the Magnetometer (MAG) aboard Venus Express(C. T. Russell et al. (2007), C. Russell et al. (2008)). From these observational examples, the luminous energy of Venusian lightning is estimated to be approximately $10^8 - 2 \times 10^9$ J. Its occurrence frequency is estimated to be 2.7×10^{-12} [/km^2/sec].

However, signals considered to originate from lightning were not detected in all observational examples. In visible light observations, no signals were detected during flybys by Pioneer Venus, the VEGA balloon, or the Galileo. Similarly, radio observations from Pioneer Venus and Cassini flybys did not detect signals thought to originate from lightning. Regarding visible light, observations showing and not showing lightning detection are particularly mixed, leaving its existence open to debate. Furthermore, signals considered to be lightning-derived include some that could arguably be explained as noise originating from the spacecraft or probe itself.

The discharge duration of lightning is under study; the waveforms observed by Lightning and Atmospheric Correlation (LAC) show a FWHM of 50 msec or more, significantly longer than the typical duration of lightning flashes on Earth. The LAC onboard the Akatsuki was developed to investigate the presence of lightning in the Venusian nightside and the distribution of airglow. It used an 8×8 pixel Avalanche Photodiode (APD). By lowering the spatial resolution, it enables high-speed sampling at 50 kHz. High-speed sampling allows for the acquisition and investigation of light curves. The specifications are summarized in the Table 1.1 below. Details are described in Takahashi et al. (2008). Observations began in 2010.

Table 1.1: List of specifications and performance capabilities of LAC onboard Akatsuki

Parameter	Value
Wavelength [nm]	777.4 (Lightning) 480 - 605 (Airglow) 557.7 (Airglow) 545.0 (Background)
Image Sensor	Hamamatsu Si Avalanche photodiode (APD)
Pixel size	2.0 mm × 2.0 mm
Image sensor format	8 pixels × 8 pixels
Field of View	16.0 degree
Spatial resolution	32 km at 1000 km
F-number	2.5

From Takahashi et al. (2020), the waveform detected by LAC that was considered to originate from Venus is shown in Figure 1.2.

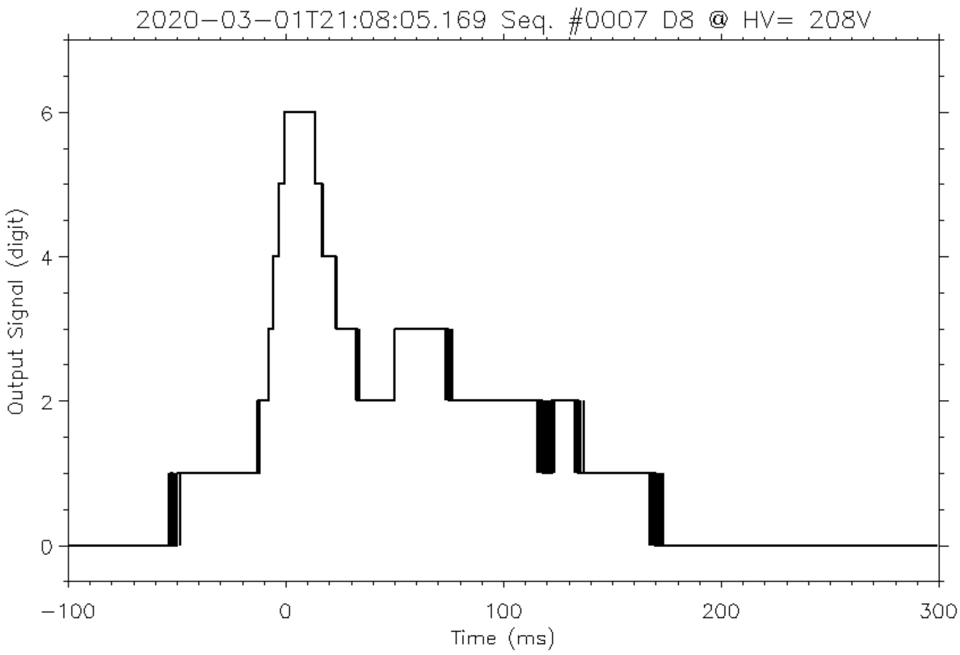

Figure 1.2: Light curve recorded in March 2020 by the Lightning and Airglow Camera (LAC) onboard the spacecraft Akatsuki (Takahashi et al. (2020)). The maximum intensity corresponds to 4.5 times larger than that of typical lightning on Earth. The time is given in milliseconds relative to the trigger points.

The FWHM of this waveform was approximately 50 msec. Furthermore, the duration was approximately 200 msec. Although the exposure time is comparable to that of 50 msec for visible light observations using ground-based telescopes (Hansell et al. (1995)), the energy was not consistent. The optical energy of lightning observed by ground-based telescopes was 10^9 J, while observations by LAC yielded values of approximately 10^7 J. The previous ground-based observation could not detect changes occurring in less than 50 msec. They didn't consider lightning events longer than 50 msec for the lightning detection. Observations by Venera 9 yielded results suggesting a duration of approximately 210 msec, though the possibility of false detection of the instrument's response cannot be completely ruled out. According to electric field observations, the typical duration was approximately 100 msec (Daniels et al. (2012)). Similar to terrestrial lightning, it is important to note that magnetic field observation waveforms and electric field observation waveforms are not equal to the discharge duration, as the effects of the ionosphere and the time-dependent terms in Maxwell's electromagnetic equations cannot be ignored. Unfortunately, this was the only waveform observed by LAC, and it remains unclear whether it represents a typical lightning waveform or a special one.

1.2.2 Jupiter

Recent observations by spacecraft have begun to reveal Jupiter's lightning alongside its atmospheric structure. Jupiter is the largest planet in the solar system and a gas giant with no solid surface. Jupiter is an outer planet orbiting beyond Earth. Its atmosphere consists primarily of 89.8% hydrogen and 10.2% helium, with trace amounts of methane, ammonia, and water present at levels below several thousand parts per million. Condensation of these minor atmospheric components results in Jupiter being shrouded in thick clouds.

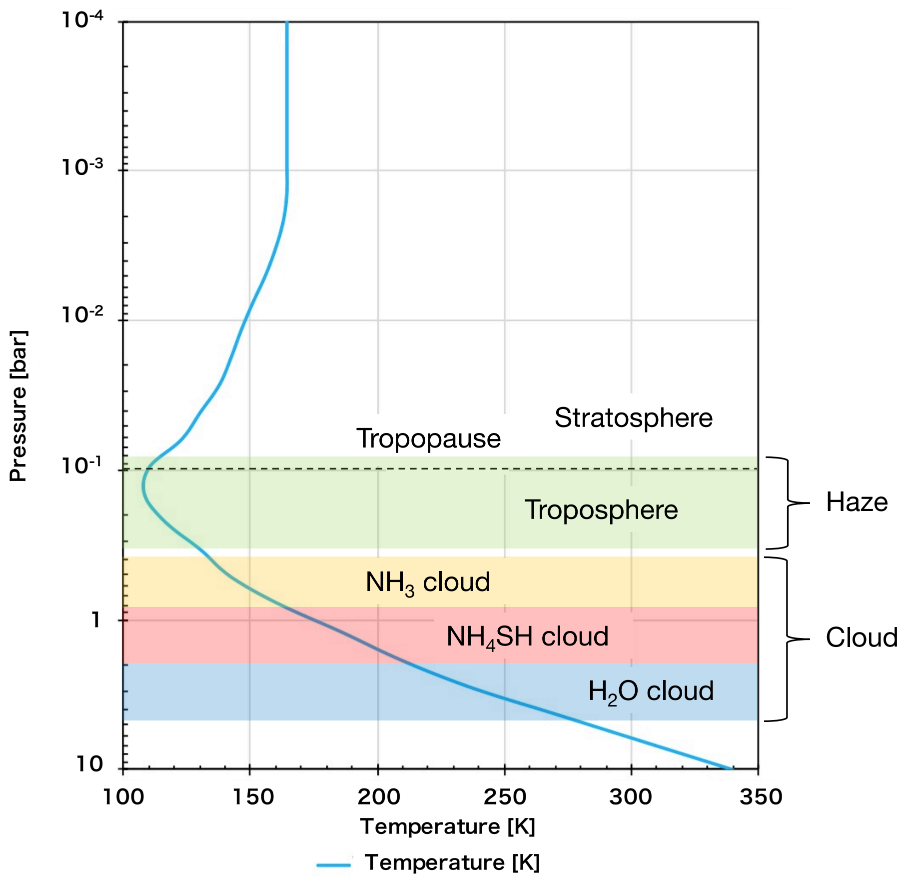

Figure 1.3: Vertical profiles of atmospheric temperature and cloud-haze structure on Jupiter. The blue solid line indicates the temperature profile as a function of altitude. The four shaded regions represent the vertical distribution of aerosols: the upper haze layer (green), the ammonia cloud deck (orange), the ammonium hydrosulfide cloud deck (red), and the water cloud deck (blue).

Since it lacks a solid surface, atmospheric pressure of 1 bar is defined at an altitude of 0 km. The troposphere is considered to extend below approximately 0.15 bar atmospheric pressure. Cloud layers are thought to exist at 0.4 – 1 bar (ammonia), 1 – 2 bar (ammonium sulfide), and 2 – 5 bar (water condensation cloud particles). One of Jupiter's defining features is its large-scale, global banded structure. Many gas giants develop east-west jet streams due to their meridional circulation and the Coriolis force from rotation. Jupiter possesses over a dozen such jet streams, forming a banded structure. Within this banded structure exist elliptical vortex systems. The largest vortex, known as the Great Red Spot, has persisted for centuries, exhibiting atmospheric dynamics distinct from Earth's. The mechanisms forming and sustaining these dozen or more jets and large-scale structures remain under study, utilizing shallow models considering only the upper troposphere, deep models accounting for convection near the core, and combined models.

Based on results from laboratory experiments replicating Jupiter's atmosphere in terrestrial laboratories, it is believed that the 656 nm emission line—a hydrogen emission line, the primary component of Jupiter's atmosphere—shines most brightly(W. Borucki et al. (1996)). Numerous instances of Jupiter's lightning have been detected through visible light observations of the night side by spacecrafts. Visible light has been observed by Voyager 1 and 2 (Cook et al. (1979)), Gallileo (Little et al. (1999)), Cassini (Dyudina et al. (2004)), New Horizons (Baines et al. (2007)), and Stellar Reference Unit (SRU) onboard Juno (Becker et al. (2020)), Additionally, observations from the Ultraviolet Spectrometer (UVS) aboard the Juno spacecraft have detected emissions that appear to be TLEs (Giles et al. (2020)).

The duration of the emission from the observation instrument onboard Juno is estimated to be approximately 5.4 msec (Becker et al. (2020)). Prior to the Juno, even with exposure times of several milliseconds, the intervals between frames exceeded 10 msec, rendering them insufficient for acquiring light curves.

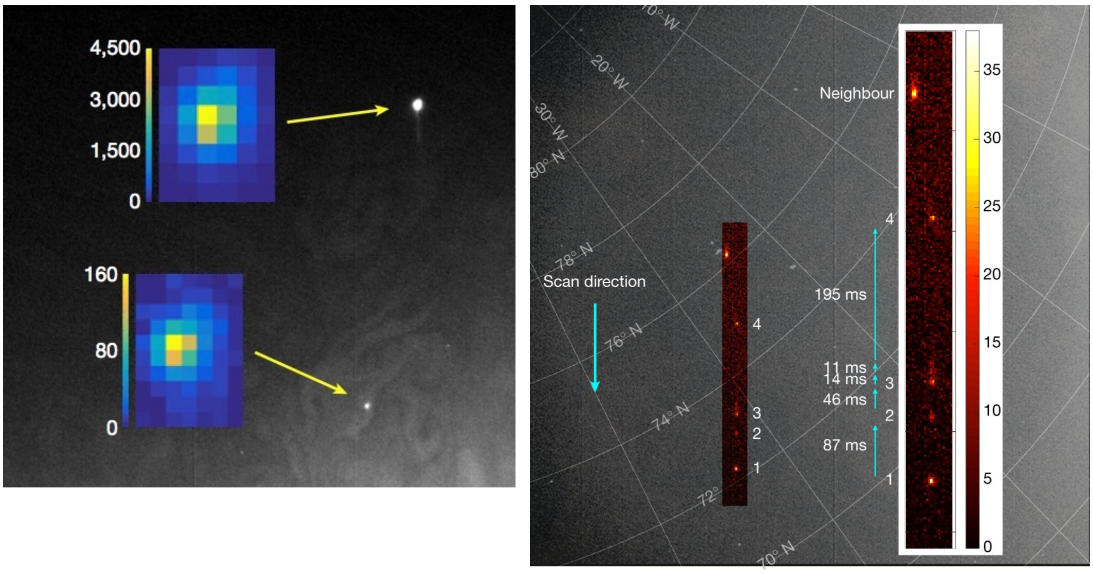

Figure 1.4: Images from Juno Stellar Reference Unit (SRU) Jovian lightning survey(Becker et al. (2020)). Both images' color scales show pixel signal levels in analogue-to-digital units. (Left) Yellow arrows point to flashes of Jovian lightning on Jupiter's dark side. (Right) Main panel showing image without motion compensation.

The waveforms related to Jupiter's TLE were observed through ultraviolet measurements(Giles et al. (2020)). Figure 1.5 shows the observed light curve. Previous studies reconstructed the light curves of TLEs by plotting UVS data with a 1 msec temporal resolution. Nevertheless, due to a lack of verification through simultaneous observations, the relationship between TLE light curves and the scattered light curves of lightning on Jupiter remains poorly understood. Research continues, including verification that the observed waveform was Jupiter's TLE.

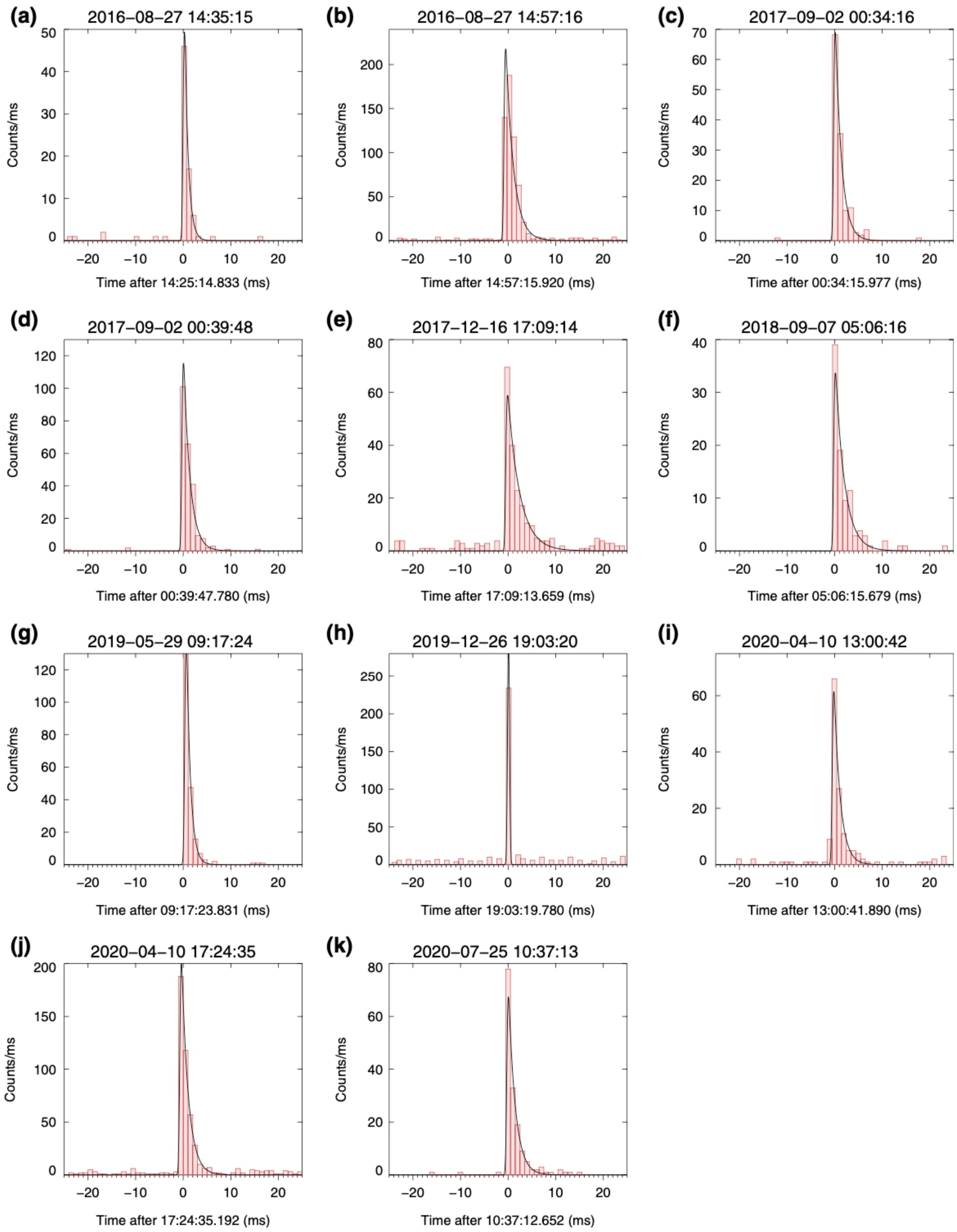

Figure 1.5: Time series data of possible transient luminous events observed by the Juno ultraviolet spectrograph (Giles et al. (2020)). A histogram of the photon detections has been shown in red; bin widths were chosen to produce a smooth distribution and vary slightly between the different frames. The black solid line shows a fitted Gaussian-exponential convolution.

Regarding the electric field observations of Jupiter's lightning, there are numerous results observed by observation of sferics in VLF and LF (Rinnert et al. (1998), Rinnert & Lanzerotti (1998)), Whistlers observation (Imai et al. (2018), Kolmašová et al. (2018), Imai et al. (2020)), observation of UHF sferics(Imai et al. (2018), Brown et al. (2018), Wong et al. (2019)), observation of Jupiter Disperesed Pulses (Imai et al. (2019, 2020)).

Previous studies have estimated characteristics of Jupiter lightning, including its occurrence frequency, distribution, and energy. After detecting lightning during nightside exploration, subsequent visible light observations of the same region revealed that lightning was observed near clouds with cloud tops higher than the surrounding clouds. These high-altitude clouds were thought to form similarly to cumulonimbus clouds, where vertical convection lifts lower-level water vapor and condensation components like ammonia to altitudes above 1 bar. The observation of lightning near cumulonimbus clouds suggested that Jupiter's lightning likely originates through a mechanism similar to that on Earth. It was thought that, as in Earth's cumulonimbus clouds, charge separation occurs within the cloud due to collisions between cloud particles, leading to lightning. However, for Jupiter, it remains unclear at what specific altitude this charge separation actually occurs and at what height the discharges take place. The relationship between the horizontal width of the scattered light (HWHM) and the depth d of thunderstorm formation was considered to be HWHM = 1.5 d based on a three-dimensional Monte Carlo scattering model (Dyudina et al. (2002)). Visible light observations by Juno suggested that thunderstorms are forming at altitudes shallower than 2 bar, originate from NH_3 clouds. The luminous energy of this lightning was approximately 10^7 J. On the other hand, observations from spacecraft such as Galileo suggested that these phenomena, which occur at pressures of several bars, originate from water clouds. The luminous energy of this lightning was estimated to be around 10^{10}, comparable to the optical energy of large-scale lightning discharges on Earth. Previous studies suggested that Jupiter's lightning originates from multiple mechanisms across different cloud components and altitudes. Recent electromagnetic wave observations by Juno have revealed that lightning occurs even in thin regions of clouds other than cumulonimbus clouds (Imai et al. (2020)). Although numerous pieces of evidence from previous studies and observations indicate the existence of lightning on Jupiter, research continues to this day.

1.3 Contribution of lightning and planetary atmosphere

Optical and electromagnetic observations of lightning and TLEs provide critical insights into discharge physics and cloud characteristics. In particular, the optical light curve contains essential information about the discharge current waveform and the surrounding cloud structure, as light undergoes multiple scattering as it passes through the cloud.

Lightning is deeply linked to atmospheric activity in its generation mechanism. If the mechanism by which lightning occurs within cumulonimbus clouds formed by moist convection is the same on Jupiter and Venus, lightning could potentially be utilized as an observational monitor for planetary atmospheric activity on these planets. The observation of lightning suggests the presence of moist convection. In the case of Jupiter, moist convection is thought to play a crucial role in transporting energy from the lower to upper layers, thereby maintaining the banded structure (Rostami et al. (2025)). Observing vertical moist convection from Earth via satellite orbit is extremely difficult for both Venus and Jupiter due to their thick cloud cover, making detection through conventional multi-wavelength observations challenging. Therefore, monitoring lightning activity is expected to enable the observation of moist convection—including its presence, occurrence frequency, and distribution—thereby facilitating the monitoring of moist convective activity. This approach can provide information on vertical convection for planetary atmospheric dynamics, thereby advancing research in this field.

Lightning activity is also significant in studies of atmospheric composition. It has been suggested that the formation of cumulonimbus clouds, which generate thunderstorms, requires a localized increase in water and other condensation components. In the case of Jupiter, it is thought that water equivalent to the mass of the Sun, or locally even more, is necessary (Yair et al. (1995); Gibbard et al. (1995)). Water plays a crucial role in the formation of giant planets (Niemann et al. (1998)). Estimating the amount of water vapor in the lower atmosphere based on lightning occurrence frequency is also expected, potentially providing useful information for research on planetary formation. Lightning is considered a candidate energy source for generating trace components in planetary atmospheres (e.g., C_2H_2 , HCN, NO_x and CO)(Bar-Nun & Podolak (1985)). Trace components are important factors in evaluating solar radiation absorption and scattering, as well as the heat balance in the atmosphere. Therefore, when estimating their production rates, if lightning is one of the sources, understanding lightning occurrence frequency may yield new insights into the production rates and distribution of atmospheric composition.

Another mechanism for lightning generation is known as volcanic lightning. When water vapor, volcanic ash, and volcanic rock particles are thrown into the air by a volcanic eruption, collisions and friction between them cause charge separation. Volcanic lightning occurs to discharge this accumulated charge. On Venus, volcanic features has been observed, but it is unknown whether these are active volcanoes. If frequent lightning is observed near volcanic terrain, it is possible that volcanic lightning is being detected. Observational data comparing the distribution and characteristics of Venusian lightning would provide new insights into the activity of Venusian volcanoes if we could determine whether it is cumulonimbus-type or volcanic.

Compared to Earth, Jupiter and Venus have significantly different atmospheric structures. Therefore, it cannot be ruled out that lightning occurs through mechanisms distinct from those on Earth. By comparing observational data of lightning on Venus and Jupiter with Earth's observational results, it may be possible to gain new insights into the mechanisms of lightning generation.

1.4 Limitations of the previous studies

Previous studies have examined the energy, spatial extent, altitudes, and flash rates of lightning on Venus and Jupiter using visible-light observations and imaging data. However, the temporal characteristics of lightning-generated light curves remain insufficiently understood. Observations indicate that terrestrial lightning involves multiple processes ranging from microseconds to hundreds of milliseconds, yielding light-emission time constants on the order of milliseconds or longer. In contrast, the processes and temporal characteristics of lightning light curves on Venus and Jupiter remain poorly constrained, leaving significant uncertainties.

These problems have not been adequately resolved to date because previous studies focused on two-dimensional images, and there were limited observations with high temporal resolution and models to evaluate them. The previous ground-based observations had an exposure time of approximately 50 msec, making it impossible to capture changes occurring on shorter timescales. The ground-based telescopes observing Jupiter in visible light had not detected signals believed to originate from lightning (Luque et al. (2015)). Because Jupiter orbits the Sun further out than Earth, observations from Earth can only capture Jupiter's daytime side. Therefore, when using ground-based telescopes, lightning emissions become obscured by brightness fluctuations on Jupiter's daytime side caused by atmospheric turbulence. They had only conducted observations at the lightning wavelength of 656 nm, and thus did not perform observations at other wavelengths that could yield differences with diurnal brightness variations.

High time resolution was achieved in LAC observations. The LAC instrument onboard the spacecraft Akatsuki performed Venusian lightning observations at 50 µsec, but only one waveform example was successfully acquired. For Jupiter, imaging with CCDs aboard spacecraft such as Galileo, with exposure times of 6 to 60 seconds, makes it unclear whether multiple lightning events occurred or whether a single large-energy discharge was observed. Radio observations suggest that on Jupiter, discharges occur at a frequency similar to that of intracloud discharges on Earth (Kolmašová et al. (2023)). It is still unknown whether all lightning observed in visible light is similar to intracloud discharges or to cloud-to-ground discharges, or what their respective occurrence rates are. Cameras prior to Juno had insufficient temporal resolution, with time intervals exceeding several seconds, making it difficult to observe the waveforms of visible light emissions. Juno's SRU has a relatively short time resolution of 2.7 msec, but the 10^{10} J energy emission observed in previous studies has not been detected. It has been suggested that Jupiter's lightning may be generated by multiple mechanisms. There has been insufficient discussion regarding the time constants possessed by each type of Jovian lightning.

Observational instruments with insufficient time resolution cannot distinguish cosmic-ray and meteorite detections. Specifically, research indicates that luminous phenomena similar to Venusian lightning can reach the same brightness as light caused by meteorites (Blaske et al. (2023)). While it is difficult to distinguish based solely on two-dimensional images or brightness, the typical brightness changes of Earth's shooting stars often differ from lightning waveforms. For example, the increase in brightness over time is often gradual, and the rate of increase and decrease around the peak may be symmetrical. By comparing them to typical lightning light curves or the luminous changes of meteors, it is expected that lightning and meteors can be distinguished.

Simulation models that explicitly account for temporal brightness changes originating from visible emission from lightning discharges have not been sufficiently developed. Previous theoretical studies, such as scattering models, neglected the temporal dimension, specifically the time-delay effects arising from multiple scattering within a three-dimensional cloud structure and distribution of cloud particles. There are virtually no existing lightning scattering light models for Venus in prior research. Models that examine the visible-light range within standard radiative transfer models exist. For Jupiter, there is a Monte Carlo scattering model that assumes a three-dimensional structure (Dyudina et al. (2002)). However, the output results show two-dimensional images assuming zenith observations from a satellite orbit, and no results are presented for light curves. Furthermore, it is not a cloud structure model that considers the actual nature of cumulonimbus. While it can examine optically thick regions in three dimensions, such as spheres, it does not account for cloud layers below the light-emitting points. It was strictly a model considering optical thickness. It has not been simulated whether lightning scattering exhibits different characteristics under conditions where the cloud structure directly beneath the cumulonimbus differs from the average cloud structure. The results of the scattered light model are used to estimate the altitude at which lightning occurs. Even in the models of previous studies, methods for evaluating the time constant of lightning were lacking.

1.5 Purpose of this study

The purpose of this study is to get new findings on the light curves of lightning discharge by observing and analyzing the light curves of lightning on Jupiter and Venus. This also aims to provide guidelines for efficient observation conditions regarding the characteristics and diversity of discharges, differences in cloud structures, and future planetary lightning observations. By clarifying the light curve of lightning, it becomes possible to understand the temporal characteristics of lightning discharges. The light emitted by lightning originates from Joule heating induced by the discharge current, and its temporal variation shows a strong correlation with that of the discharge current. Therefore, by analyzing the light curve, this study can discuss differences in discharge patterns—whether multiple discharges occurred consecutively or a single discharge persisted for an extended period. Since the observed light curves are affected by cloud scattering, their characteristics are also expected to provide constraints on the vertical structure of the clouds. Based on the results of this study, it can also contribute to discussions that advance understanding of the lightning discharge process and inform appropriate observation conditions for future measurements.

To address these observational and theoretical gaps, we developed a two-band simultaneous photometer and a scattering simulation model for the lightning light curve. This study developed an observational instrument to measure the light curves of lightning on Venus and Jupiter. It was named the Planetary Lightning Detector (PLD). The PLD was designed for installation on ground-based telescopes, which can secure significantly longer observation times compared to spacecraft. By simultaneously observing at two wavelengths, the PLD distinguishes lightning waveforms from variations in the brightness of the day side, Earth's atmospheric brightness, meteors, cosmic rays, and other sources. Furthermore, we developed a lightning-induced light scattering model for estimating and evaluating typical light curve waveforms. The base model was CloudScat.jl (Luque et al. (2020)), a terrestrial lightning-induced light scattering model. This model can simulate light curves considering cloud number density, particle size, and composition information, which previous studies for Venus and Jupiter could not simulate. Since the base model could only simulate cloud particles with a single composition, we modified it to allow random composition consideration based on the number density.

The Venusian cloud model employed a standard Venusian cloud structure model with H_2SO_4 as the primary constituent. The Jupiter model utilized results from numerical simulations of cumulonimbus cloud formation composed of three types of clouds: H_2O, NH_3, NH_4SH. We compare the light curves observed by PLD with the waveforms and characteristics obtained from the model, along with prior research. To evaluate this model, we compared it with Earth lightning photometric curve data observed from 2012 to 2015 by the JEM-GLIMS photometer PH onboard the ISS.

2 Method

2.1 Development of Planetary Lightning Detector (PLD)

We developed an optical two-band photometer. It was named Planetary Lightning Detector (PLD). We designed the PLD for mounting on the 1.6-m Pirka telescope (see Figure 2.1) at the Nayoro Observatory, Faculty of Science, the Hokkaido University at Nayoro in Hokkaido. We conducted the observation with a short interval of a day over more than a month. In this chapter, we present this instrument's design, construction integration, and performance.

2.1.1 Design overview of Planetary Lightning Detector (PLD)

The PLD was mounted at the Nasmyth focus (f/12.0) of the Pirka Telescope. An exterior photograph of the PLD mounted on the Nasmyth focus mount is shown in Figure 2.1. An overview diagram of the optical layout from the folding mirror to the Nasmyth focus is shown in Figure 2.3. The optical layout is also shown in Figure 2.2. Table 2.1 lists the main specifications of the device. A dichroic filter is used to split

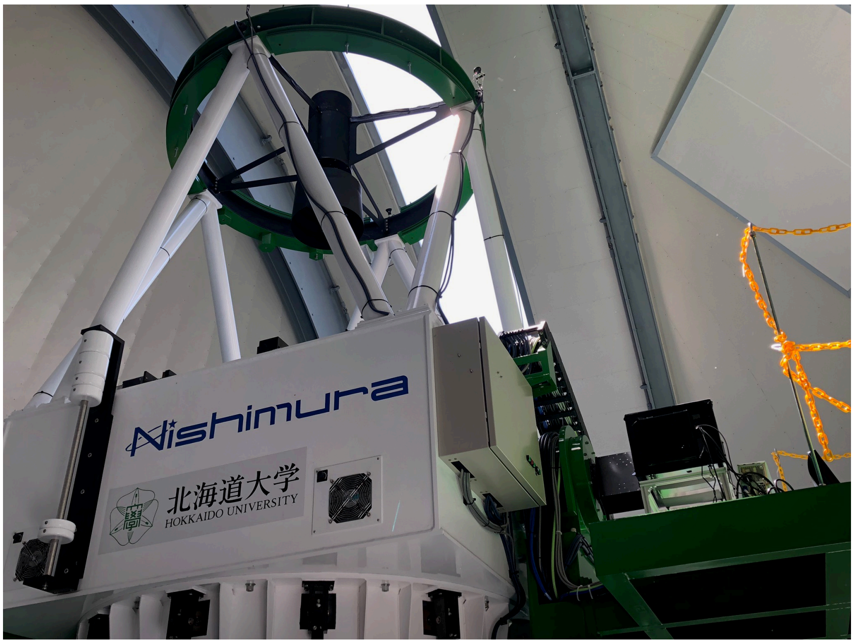

Figure 2.1: Overview of the 1.6-m ground-based telescope, Pirka telescope, and the installation of the Planetary Lightning Detector (PLD). The external view of the Pirka telescope at Nayoro observatory, Hokkaido, Japan. The PLD black box is mounted at the Nasmyth focus.

the optical path. Light on the short-wavelength side (400 – 580 nm) passes straight through the filter. A CCD for confirming the PLD's position is placed at the focal plane of the telescope on this straight optical path. Light on the long-wavelength side (625 – 795 nm) is reflected by the dichroic filter, bending the optical path by 90 degrees. The layout employs a Keplerian optical system on the short-wavelength side of the split

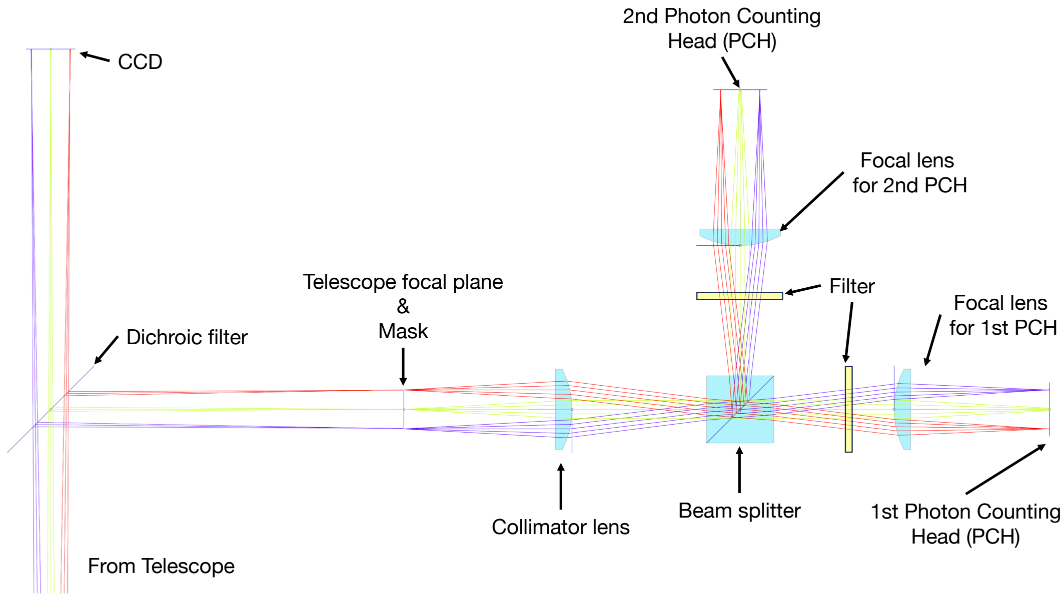

Figure 2.2: Optical layout of the Planetary Lightning Detector (PLD).

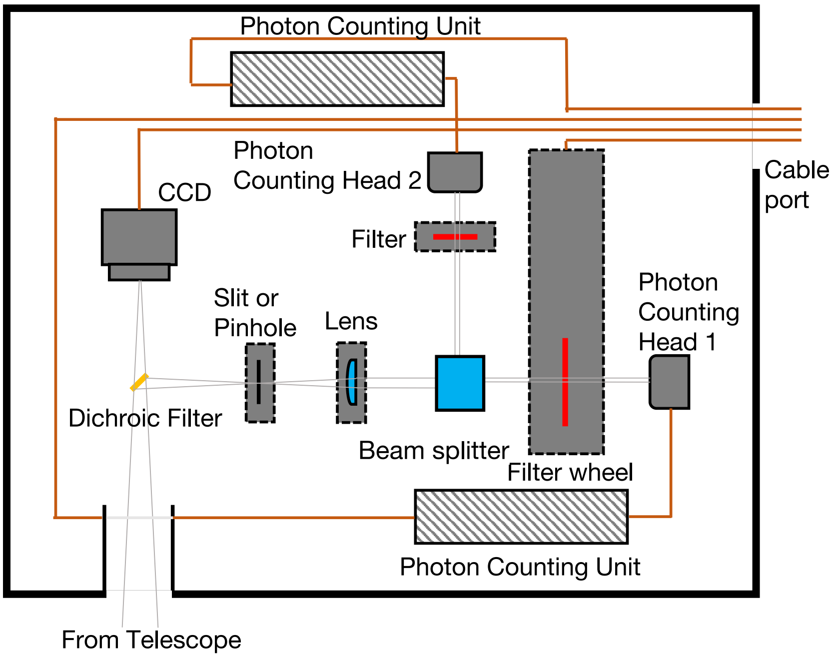

Figure 2.3: Opto-mechanical layout of the inside of the Planetary Lightning Detector (PLD).

optical path. The collimated beam from the Keplerian optical system is further split by a beam splitter. The transmission-to-reflection ratio of the beam splitter is 9:1. Filters for specific wavelengths are installed in each of the split optical paths. A filter wheel is mounted on the transmission side of the beam splitter. The filter wheel is used to switch between filters. The wheel holds one filter each for Venus and Jupiter lightning observation wavelengths. The remaining positions hold a clear optical element and a light-blocking mask. A fixed filter is installed in the optical path on the reflection side

Table 2.1: List of specifications and performance capabilities of the Planetary Lightning Detector (PLD)

CCD	WTEC WAT-100N
Array format	1/2inch interline transfer CCD image sensor 768 × 494 pixel (Effective)
Photon Counting Head (PMT)	HAMAMATSU Photonics H12386-01
Effective area	Diameter 8 mm
Spectral Response	230 – 870 nm
Filter	
for PCH1	656 nm (FWHM = 1 nm) 777 nm (FWHM = 1 nm)
for PCH2	700 nm (FWHM = 10 nm)
Dichroic filter	625 - 795 nm (Reflection >0.97) 400 – 580 nm (Transmission >0.85)
Filed of view	40 arcsec × 50 arcsec (CCD) 5”, 10”, 30”, 1’, 2×11” (PMT)
Shutter speed	1/100, 1/250, 1/500,1/1000,1/2000, 1/5000, 1/100000 sec (CCD) Minimum 50 µsec, Maximum 100 sec (PMT)

of the beam splitter. After passing through the filters, the light is focused by a lens. The collimating lens has a focal length of 50 mm, and the focusing lens also has a focal length of 50 mm. The maximum field of view angle of the optical system without a field stop aperture mask is approximately 3.33 arcminutes, matching the telescope's field of view angle. A sensor is placed behind the camera lens. The sensor aperture is 8 mm, and the maximum field of view angle without the PLD mask is about 1 arcminute.

A mask for field stop is installed on the objective lens focal plane of the Kepler optical system. By restricting the field of view, fluctuations in light outside the observation target are eliminated. The mask design is separate for Venus and Jupiter. Details are explained in Section 2.1.3.

The PLD is a box-shaped enclosure. The main unit measures 424 × 250 × 320 mm. It is not directly attached to the telescope and does not rotate with the telescope. An image rotator is installed between it and the telescope; rotating the rotator adjusts the field of view in the right ascension and declination directions.

The PLD filter simultaneously observes at two wavelengths: one for lightning wavelengths and another for detecting background light and other non-lightning variations. The wavelengths for lightning observation are 777 nm and 656 nm, chosen as the central wavelengths based on emission line wavelengths obtained from indoor experiments (W. Borucki et al. (1985)). To maximize the signal-to-noise ratio (S/N ratio) as much as possible, the wavelength bandwidth is narrowed to 1 nm. At this point, it is necessary to consider the effect of blue shift due to the angle of incidence. The maximum incidence angle of the collimated beam is approximately 3.4 degrees, determined from the focal lengths of the collimator lens and the imaging lens, and the maximum diameter of the field-of-view aperture mask. Filters were selected considering the shift in the center wavelength caused by blue shift at this angle. For the fixed filter used for background light, we considered wavelengths where no emission lines appear in the lightning emission spectrum, while also avoiding atmospheric absorption wavelengths prone to fluctuations due to meteorological conditions in the atmospheres of Jupiter and Venus. As a result, a filter with a center wavelength of 700 nm and a wavelength bandwidth of 10 nm was adopted.

The alignment CCD employs the WATEC WAT-100N. This monochrome camera, equipped with a 1/2-inch CCD, was developed for astronomical imaging. It has an effective pixel count of 768 × 494 pixels, with a pixel size of 8.4 × 9.8 μm. The CCD's field of view is approximately 40 arcminutes × 50 arcminutes. The alignment CCD does not have a filter. Exposure time equivalent shutter speed and gain are manually controlled using the remote control supplied with the camera.

2.1.2 Detector and controller

The sensor for detecting lightning waveforms and background fluctuations employs photon counting. Photon counting using a photomultiplier tube (PMT) was adopted to observe lightning waveforms. Compared to CCDs, PMTs sacrifice spatial resolution but enable measurement with high temporal resolution due to reduced readout time. Furthermore, since they are less susceptible to dark current effects, shot noise proportional to the number of received photons becomes the primary noise source, allowing for a high S/N ratio. For the photon counting sensor, PLD adopted the Photon Counting Head (PCH) model H12386-01 manufactured by Hamamatsu Photonics. Table 2.2 summarizes the specification of H12386-01. Figure 2.4 shows the wavelength sensitivity spectrum.

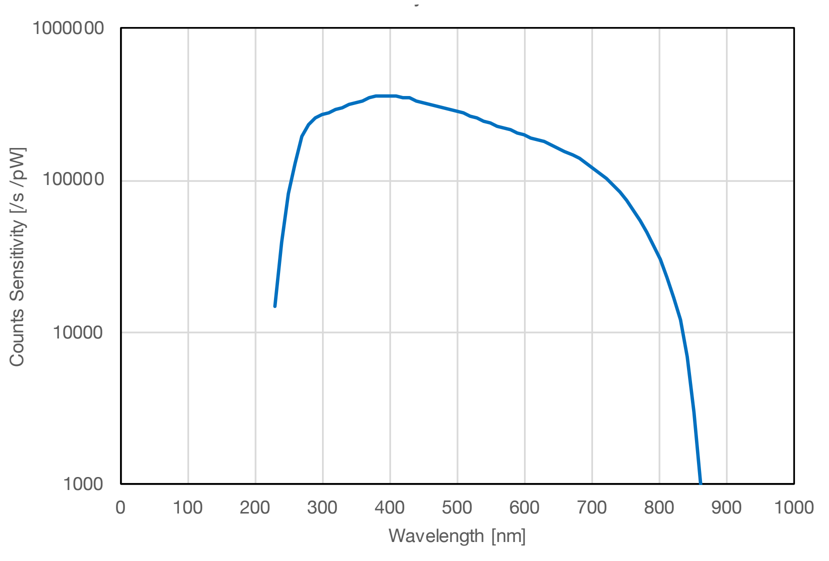

Figure 2.4: Spectral count sensitivity of the photometer (H12386-01, Hamamatsu) as a function of wavelength. The blue solid line indicates the sensitivity as a function of wavelength.

PCH (H12386-01) is a device consisting of a metal-cased photomultiplier tube (metal-packaged photomultiplier tube), a circuit for high-speed photon counting, and a circuit

Table 2.2: List of specifications of photometer, H12386-01

Effective area (Diameter) [mm]	8
Peak sensitivity wavelength [nm]	400
Count linearity [s^{-1}]	5×100^6
Dark count (Typical) [s^{-1}]	600
Weight [g]	60

Table 2.3: List of specifications of controller, C8855-01

Maximum count	2^{32} counts/counter gate
Maximum count frequency	50 MHz
Counter gate	50 μ – 10 sec
Size [mm]	120 × 30 × 96
Power	+7 V/ 500 mA Max.

for power supply. The photomultiplier tube's photocathode surface has wavelength sensitivity from ultraviolet to near-infrared. A multi-alkali (Sb-Na-K-Cs) type was selected. Furthermore, within this series, the model with higher sensitivity (quantum efficiency) at 656 nm and 777 nm was adopted. The device's effective aperture is 8 mm. The collimating beam and imaging lens, along with the optical system, are designed to match this effective aperture. The C8855-01 controller manufactured by Hamamatsu Photonics is used to control the H12386-01. The specifications for the C8855-01 are summarized in Table 2.3. The counter gate controlled by the controller is nearly equal to the exposure time of the PLD. The time interval per counter gate is on the order of tens of nanoseconds. The two PCHs are each controlled by an identical controller, and the controllers are connected to the control PC via USB.

2.1.3 Mask

The mask is located at the focal plane of the Pirka telescope after being reflected by a Dichroic filter. PLD has an 4 pinhole masks with the diameter 5, 10, 30, and 60 arcsec and a slit with 2 arcsec × 11 arcsec. We can select one of them depending on the target. Figure 2.5 shows a picture of the mask. Photomultiplier tubes lack spatial resolution, necessitating proper adjustment of the desired field of view. For PLD, a mask is placed at the point where the telescope forms an image to restrict the field of view. The mask size depends on the PLD optical system and the combined focal length of the Pirka telescope.

Prepare multiple masks for Venus. Due to its orbital position relative to Earth, Venus's distance varies from approximately 38 km to 261 km. Consequently, its apparent diameter changes significantly, ranging from 66 arcseconds to 9.7 arcseconds. Additionally, circular masks were created to observe only the night side of Venus, avoiding the day side. For Venus, prepare masks with field of view (FOV) of 5, 10, 30, and 60 arcseconds. Given the focal length f =19238 mm, the mask diameter D_{mask} can be

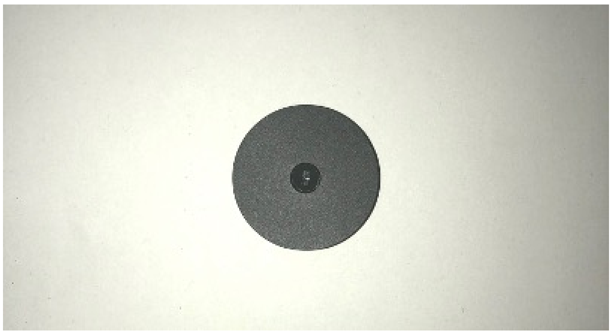

Figure 2.5: Picture of the photometers' mask (slit) onboard PLD. The slit width is 0.2 mm. The slit height is 1.1 mm.

calculated using the following formula.

$$D_{mask} = 2 \cdot f \cdot \tan(\frac{\text{FOV}}{2}) \tag{1}$$

As a result, the mask sizes are 0.47, 0.93, 2.8, and 6.0 mm, respectively.

The mask for Jupiter employs slits. Jovian lightning is frequently observed in regions called belts, which appear dark in visible light due to their striped patterns, as indicated by prior research. The PLD was designed with a vertical width to primarily observe the belt regions: the North Equatorial Belt (NEB), South Equatorial Belt (SEB), and South Temperate Belt (STB), located around 30 degrees latitude. The horizontal width was designed to observe a 60-degree longitude span, minimizing the effects of atmospheric limb darkening. The result was a slit of 2 × 11 arcseconds (0.2 × 1.0 mm).

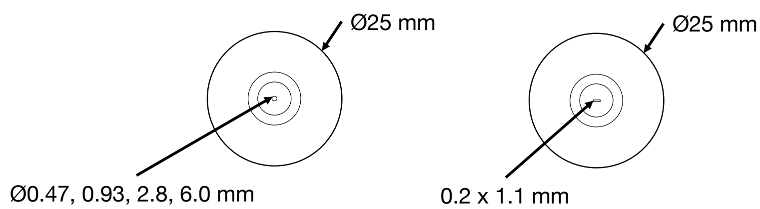

Figure 2.6: Mechanical layout of the photometers' masks onboard PLD. (Left) Example of the pinhole mask for Venus lightning observations. (Right) The slit mask for Jupiter lightning observations.

2.1.4 Performances

PLDs lack spatial resolution within their field of view, making it impossible to simultaneously measure reference stars. Therefore, absolute measurements of brightness variations cannot be obtained. Due to the highly variable nature of Earth's atmospheric effects, such as weather conditions, photometric results can only be estimated by order of magnitude.

2.1.5 Imaging

Figure 2.7 shows an example of imaging using a CCD for Jupiter alignment, and Figure 2.8 shows an example for Venus alignment.

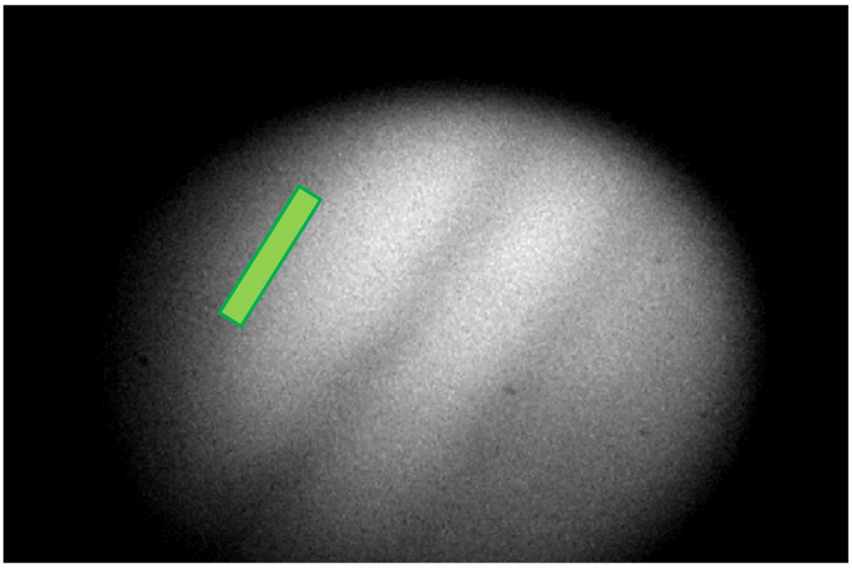

Figure 2.7: Example of the Jupiter image observed by the CCD onboard PLD and the observed area by the photometers with the slit mask. The green-colored area indicates that the two photometers observed with the slit mask (0.2 mm $\times$ 1.1 mm)

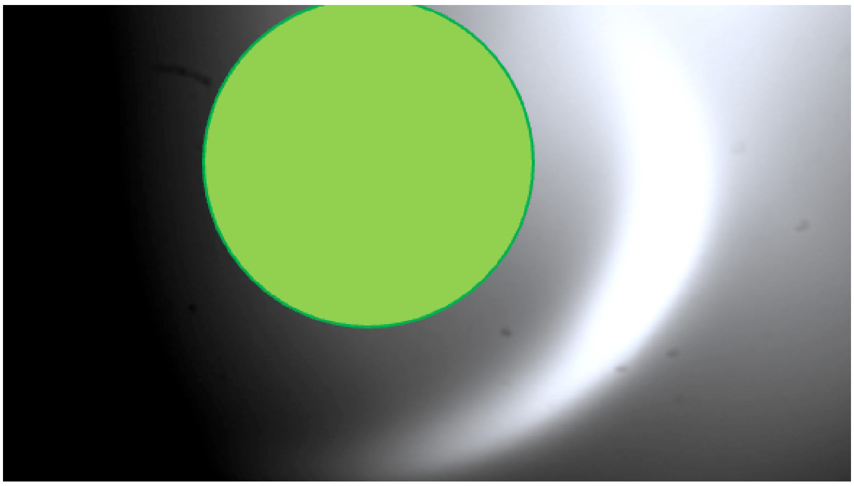

Figure 2.8: Example of the Venus image observed by the CCD onboard PLD and the observed area by the photometers with the pinhole mask. The green-colored area indicates that the two photometers observed with the pinhole mask (diameter = 6 mm).

The position of the PLD field of view within the alignment CCD's field of view was confirmed by scanning celestial objects within the field of view. Figure 2.9 shows a schematic diagram illustrating the method for confirming the PCH field position within the alignment CCD's FOV.

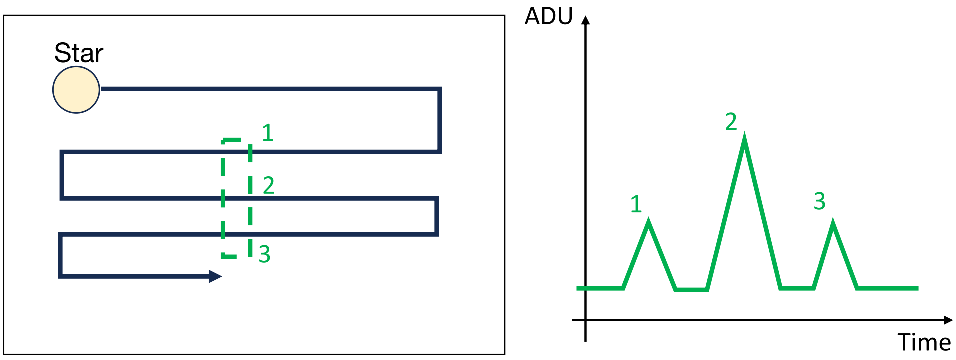

Figure 2.9: Schematic of the observation process and the conceptual data for the PLD's photometers observation area. (Left) The green broken line indicates the mask area on the CCD image. The black solid line indicates the star tracking pass. (Right) Conceptual data obtained by the observation indicate the left images. If the star enters the photometers' Field of View (FOV), the light curve shows peaks. The position of the image where the peak value occurred in the light curve was taken as the PLD observation area.

Adjust the telescope's RA/DEC offsets and move it to scan the CCD field of view while aligning with the reference star. Simultaneously, acquire the light curve using the PCH. When an object enters the PCH's field of view, the PCH count increases. The densely clustered areas of increasing counts were estimated as the PCH's field of view aperture. When manually replacing the field of view aperture, verify the FOV.

2.1.6 Calibrated coefficients

Table 2.4 summarizes the conversion coefficients for each wavelength.

Table 2.4: List of conversion coefficients from digital units to physical quantities for PLD measurements.

Wavelength [nm]	PLD efficiency	Measured conversion coeff. [J/ADU]	Estimated conversion coeff. [J/ADU]	Ratio of estimated to measured
656	0.022	2.83×10^{-16}	6.42×10^{-17}	0.23
777	0.071	2.95×10^{-16}	2.04×10^{-16}	0.69
Ratio (656/777)	0.318	0.960	0.314	

The values obtained from observational results are lower than those estimated from design values. However, the estimated efficiency from the design does not account for light attenuation in parallel sections, the Earth's atmospheric transmittance, the reduced efficiency of the telescope's primary mirror, or the effects of misalignment during assembly. Nevertheless, based on prior research, it was estimated that lightning energy of 10^9 to 10^{10} J, when observed as a point source, would appear as counts ranging from 10 to several hundred ADUs. Therefore, observations were conducted on the assumption that this would manifest as an amplitude significantly above the noise level.

2.1.7 Data reduction and analysis

The data acquired by the photon counting head (PCH) mounted on the PLD is a light curve recording changes in brightness. From this light curve, signals possessing specific time scales and characteristic waveforms are extracted. The light curves primarily contain two types of waveforms originating from non-lightning variations: shot noise from the photomultiplier tube and background brightness (Jupiter's daytime brightness for Jupiter, and contamination from the daytime surface for Venus). First, to remove shot noise originating from the PCH, noise reduction using wavelet transform and extraction of specific wavelengths were performed. We applied the same processing to two time series datasets measured simultaneously at two wavelengths. By comparing these two datasets, we investigated waveforms amplified only at the lightning wavelength (777 nm or 656 nm) relative to the 700 nm wavelength where background changes were observed, examining them at different timescales. Python scripts were used for data analysis.

Wavelet transform was applied for noise reduction, extraction of waveforms with specific time scales, and bandpass filtering. Figure 2.10 shows an overview of the wavelet transform.

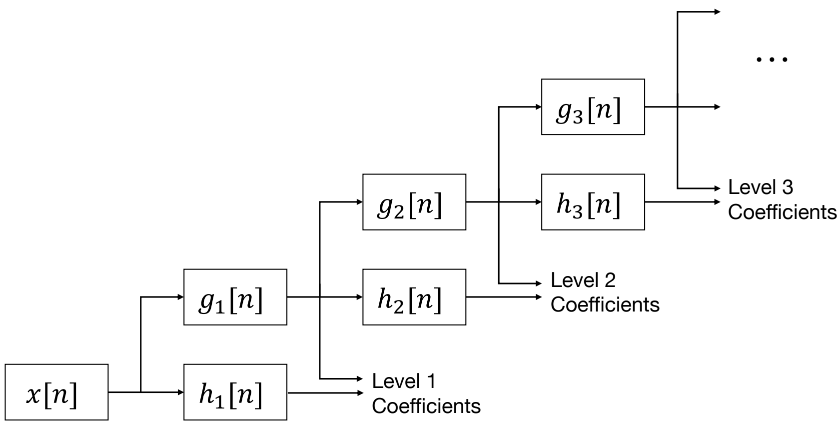

Figure 2.10: The block diagram represents the implementation of the wavelet transform. g and h indicate the approximate and detailed coefficients, respectively.

Wavelet transform analyzes signals using local basis functions (wavelet functions) that carry both time and frequency information. Like the Fourier transform, it decomposes signals into various frequencies and times using wavelet functions. It offers advantages over the Fourier transform, being more robust for non-stationary signals and better preserving time-frequency information. The Daubechies wavelet function was used as the wavelet function, as it allows for relatively continuous changes while maintaining continuity.

This time, we are utilizing the stationary wavelet transform within the wavelet transform family. Since time series data is discrete, it is necessary to perform a discrete wavelet transform. The stationary wavelet transform is a type of transform method developed to avoid downsampling in the discrete wavelet transform. It calculates wavelet coefficients decomposed into different frequency bands and scales using the stationary wavelet transform. Larger scales contain higher-frequency components and are called detail coefficients. Smaller scales contain lower-frequency components and are called approximation coefficients. Here, threshold processing is applied to the decomposed wavelet coefficients for noise removal. Figure 2.11 shows an overview diagram of noise removal using the wavelet transform.

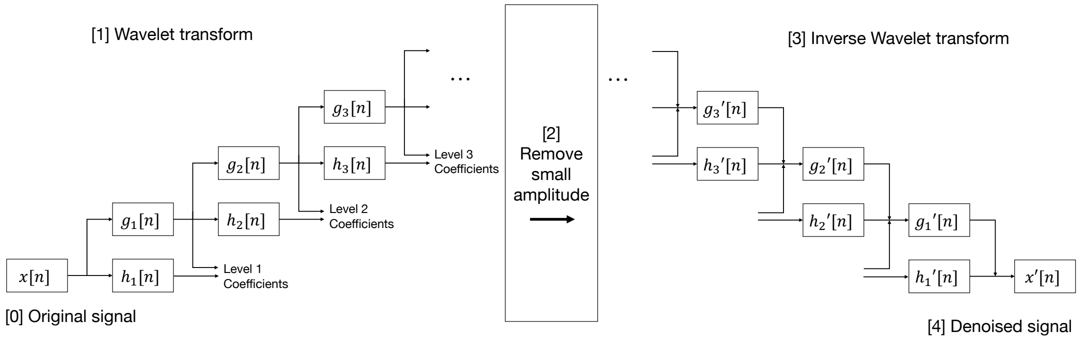

Figure 2.11: The block diagram shows the implementation of wavelet denoising. g and h indicate the approximate and detailed coefficients, respectively. A thresholding process is applied to remove coefficients below a specified threshold, thereby eliminating some coefficients. An inverse wavelet transform is then performed to reconstruct the signal.

Set detailed coefficients with high noise levels to zero if they fall below a certain threshold. For this threshold determination, the Universal threshold method was adopted. While the Universal threshold is simple to implement and determines the threshold based on noise level statistics, it tends to lose more signal components compared to other threshold estimation methods. However, it enables reliable noise removal. After applying threshold processing, perform an inverse wavelet transform using the wavelet coefficients from which noise components have been removed. This reconstructs the noise-removed signal back into the original time domain. This process is equivalent to low-pass filtering to remove high-frequency noise components.

Next, bandpass processing is performed to extract a specific frequency range using low-pass filtering based on the stationary wavelet transform. A low-pass filter with a cutoff frequency at the upper limit of the desired frequency range is applied. This process yields a signal containing frequency components up to $0 - f_{High}$ Hz. Next, a low-pass filter processing with a cutoff frequency at the lower frequency limit is applied. This process yields a signal containing frequency components up to $0 - f_{Low}$ Hz. Subtraction is then performed between these two signals. The result of this subtraction allows extraction of the signal containing the frequency components between f_{Low} and f_{High}. By applying the aforementioned noise processing using wavelet transform to the low-pass filter, waveforms with specific frequency components can be extracted while preserving their temporal components.

The trigger level is determined from the bandpass-processed signal. The variance and mean of the bandpass-processed signal are calculated. The trigger level is set to the greater of four times the variance or the mean value. Waves where the maximum value exceeded the trigger level, and where the trigger level was exceeded at two or more consecutive points in time, were prioritized for verification. For this analysis, processing was performed to enable extraction of waveforms at scales of 5, 10, 50, 100, and 200 msec.

Not only waveform verification, but also verification of the waveform's maximum value is performed to examine the trigger level for lightning. It is considered that waveforms originating from noise that cannot be completely removed exist within the bandpass-processed waveform results. The primary noise in the PCH is shot noise, whose distribution is close to a normal distribution. Therefore, if there are outliers in the distribution of triggered events that deviate from the noise's normal distribution, it is considered that an event was triggered. This time, we use the distribution of the maximum values of the waveforms from the second PCH (700 nm), which is observing background fluctuations, as the noise's normal distribution. The Kolmogorov-Smirnov Test was used to determine outliers. The Kolmogorov-Smirnov test, when used with two samples, tests whether two independent datasets were drawn from the same unknown distribution. To detect differences in distribution between groups, it compares the cumulative distribution functions (CDFs) and calculates a p-value. If the p-value is 0.1 or less for distributions above a certain threshold, it is considered that statistically significant cumulative distribution outliers exist.

We attempted to detect lightning-derived waveforms using two methods: comparing waveforms and comparing cumulative distributions. The brightness of triggered events is estimated from the peak values of the detected waveforms. In PLD observations, due to daytime observations and the lack of spatial resolution, observations of standard stars could not be performed simultaneously with observations of Venusian and Jovian lightning. Therefore, energy estimation is limited to an order-of-magnitude estimate based on the relative difference from brightness variations on the celestial body's day face. When observing lightning from Earth, the spread of lightning emissions is on the order of tens of kilometers compared to the several AU distances of Jupiter or Venus, allowing lightning to be approximated as a point source. It is assumed that light from lightning at the cloud top is scattered isotropically in a hemispherical pattern. Consequently, the intensity of lightning at the cloud top can be estimated using the ratio of the telescope aperture to the solid angle and the energy estimated from the PLD observations. Therefore, the energy of the lightning is calculated from the count values received by the PLD according to the following conversion formula.

$$E_L = \frac{4\pi D^2}{A} \alpha C_{obs} \tag{2}$$

E_L represents lightning flash energy, unit is J, D is the distance between the planet and Earth, A is the effective aperture area of the telescope, C_{obs} represents the PCH measurement count value, with the unit being Analog Digital Unit (ADU), α is the coefficient that converts the measured count value of the PCH, as shown in Table 2.4, into energy.

2.2 Earth lightning observation

To compare and verify the observation results of Venus and Jupiter obtained by the PLD and the simulation results from the developed model, we refer to studies on Earth's lightning, which are being advanced using various methods such as visible light, radio waves, ultraviolet, and infrared, from the ground and from satellite orbits. This chapter organizes the waveforms of Earth's lightning observed by JEM-GLIMS aboard the ISS, similar to the nadir observations by the PLD and spacecraft.

2.2.1 JEM-GLIMS

JEM-GLIMS is an instrument developed for the mission to observe Transient Luminous Events occurring in the stratosphere, mesosphere, and lower thermosphere following lightning discharges. It is installed on the Exposed Facility of the Japanese Experiment Module (JEM) aboard the International Space Station (ISS). The instrument consists of two CMOS observation devices (LSI) and six photometers (PH) utilizing photomultiplier tubes and photodiodes for optical observation. The specifications for JEM-GLIMS are shown in Tables 2.5 and 2.6. Details are described in Sato et al. (2015). Initial operations began at the end of September 2012 and concluded in August 2015.

Table 2.5: List of LSI specification

LSI-1 Wavelength	740 – 830 nm
LSI-2 Wavelength	762 ± 5 nm
FOV	28.3 × 28.3 deg
Pixel number	512 × 512
Spatial resolution	0.55 km/pix
Time resolution	34.5, 8.6, 2.1 msec (Selectable)

Table 2.6: List of PH specification

Item	Unit #1				Unit #2	
	PH1	PH2	PH3	PH4	PH5	PH6
Wavelength	150 – 280 nm (N_2 LBH)	337 ± 5 nm (N_2 2P)	762 ± 5 nm (N_2 1P)	600 – 900 nm (N_2 1P)	316 ± 5 nm (N_2 2P)	392 ± 5 nm (N_2^+ 1N)
FOV	42.7 deg			86.8 deg	42.7 deg	
Time resolution	50 µsec					

The PH instrument aboard JEM-GLIMS features ultraviolet wavelength filters designed to observe TLEs, such as sprites, which are difficult to detect from the ground due to absorption and scattering by Earth's atmosphere. It determines whether TLEs were detected based on results from the ultraviolet wavelength-equipped PH1 and PH2 instruments. With a sampling frequency of 20 kHz and an exposure time of 50 µsec per data point, the time resolution is 40 times higher than that of the PLD. It is 10 times lower than the time resolution achievable with waveforms obtained from models. Caution is required regarding the difference in time resolution when comparing waveforms.

The classification of discharge types in JEM-GLIMS observation waveforms is based on the results in Bandholnopparat et al. (2019). Previous studies distinguished between IC, +CG, -CG, and lightning discharges by comparing results from the lightning networks WWLN, JLDN, NLDN, and GEON. Lightning waveforms not classified in previous studies are referred to here as Unclass.

2.3 Modeling of lightning scattering

To investigate whether the light curves recorded by the PLD, which document the temporal variations in visible light intensity, represent lightning-derived waveforms, we developed a visible light scattering model for Venusian and Jovian lightning. Using this model, we estimate the lightning scatter light curve and verify the detected waveform.

2.3.1 Modeling and numerical algorithm

The fundamental structure of the lightning-induced light scattering model is identical to CloudScat, which was developed for validating Earth's thunderstorm-bottom-of-sky observations using instruments such as the Modular Multispectral Imaging Array (MMIA) mounted on the ISS and others, based on Thomson & Krider (1982) (Light et al. (2001)). Here is a summary of that.

The model developed by Light et al. (2001) does not alter the wavelength of photons, therefore considering photons of a specific single wavelength. The model's applicable wavelength range is from 200 nm to 1000 nm. All photon processes propagate asynchronously and independently. The model considers two processes: scattering, which alters the propagation direction of photons, and absorption by molecules, which reduces the statistical weight. The scattering process is treated as a discrete probabilistic event. The absorption process is treated as a continuous process.

Figure 2.12 shows an overview diagram of the process handled by the model.

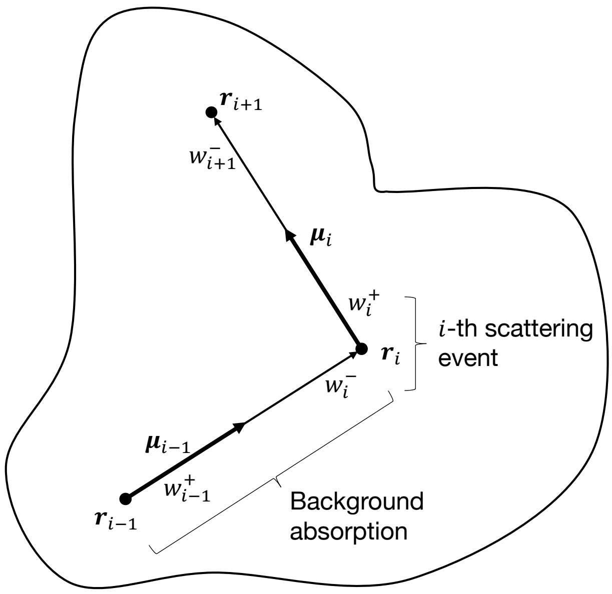

Figure 2.12: Schematic diagram of scattering processes with the notation employed in this model. $\boldsymbol{r}$ indicates position, $\boldsymbol{\mu}$ indicates unit vector, and w indicates intensity.

Consider the case where the ith photon collision occurs at position $\boldsymbol{r}_i$ and time t_i. The intensity of the photon before collision is denoted by w_i^-, its velocity by the speed of light c, and its unit vector by $\boldsymbol{\mu}_{i-1}$. Thus, it can be expressed as $c\boldsymbol{\mu}_{i-1}$.

Upon collision, the force instantly changes to w_i^+, and the velocity changes to $c\boldsymbol{\mu}_{\boldsymbol{i}}$.

Due to the absorption effect in the background, the intensity decays before collision, so $w_{i+1}^- \leq w_i^+$. The equality holds only when there is no absorption. When $t_0 = 0$, let $w_0^+ = 1$, and assume that the random initial positions $\boldsymbol{r}_0$ are uniformly distributed along the line, and that $\boldsymbol{\mu}_0$ exhibits isotropy. All outputs are normalized by dividing by the initial photon count.

As photons propagate, the total collision rate with background scattering matter is expressed per unit time by the following equation.

$$\nu(\boldsymbol{r}) = c \sum_{p=1}^{m} \bar{\sigma_p}(\boldsymbol{r}) n_p(\boldsymbol{r}) \tag{3}$$

c is the speed of light. $\bar{\sigma_p}(\boldsymbol{r})$ is the locally averaged cross section, $n_p(\boldsymbol{r})$ is the number density of scattered particles at position$\boldsymbol{r}$ for a given process p. Since the entire spectrum of scattered particles with various cross sections exists, the cross section is locally averaged here. To estimate interaction times, the model employs the null collision method, calculating the rate satisfying $\nu_T > \nu(\boldsymbol{r})$ anywhere within the computational domain. The time until the$i$th scattering is expressed as follows.

$$t_i = t_{i-1} + \nu_T^{-1} \left|\log(\xi_{i-1})\right| \tag{4}$$

ξ_i is an independent random variable uniformly distributed on the interval from 0 to 1. The type of interaction is determined based on the probability assigned proportionally to each individual rate and the probability represented by $1 - \nu(\boldsymbol{r})/\nu_T$.

Consider Mie scattering, one type of scattering process. In Mie scattering, interaction occurs between photons of wavelengthλ and cloud particles modeled as dielectric spheres of radius R when $\lambda \ll R$. The cross section of the interaction is expressed by the following equation.

$$\sigma_{Mie} = Q_{ext}(R)\pi R^2 \tag{5}$$

Q_{ext} represents the damping coefficient, which exhibits a value close to 2. Incident radiation on scattered particles is partially absorbed and re-emitted at a rate known as the single-scattering albedo, denoted by the ratio ω_0. In the model of Light et al. (2001), this absorption is taken into account, and the statistical weight is changed from w_i^- to w_i^+ for each collision as follows. First, we determine the temporary indicator w_i'.

$$w_i' = \omega_0 w_i^- \tag{6}$$

If w_i' is greater than the threshold w_min less than 1, then $w_i^+ = w_i'$. Otherwise, $w_i^+ = 1$ with probability w_i', and $w_i^+ = 0$ with probability $1 - w_i'$. In this study, $w_{min} = 10^{-2}$ was adopted.

Electromagnetic waves scattered by Mie scattering undergo a change in the direction of propagation of the incident photons. The unit solid angle scattering intensity distribution given the angle θ with the incident direction is called the phase function. Based on Thomson & Krider (1982), the Henyey-Greenstein phase function, $p_{HG}(\theta)$, was adopted.

$$p_{HG}(\theta) = \frac{1 - g^2}{(1 + g^2 - 2g\cos\theta)^{3/2}} \tag{7}$$

At this point, the phase function is normalized as follows.

$$\int_0^{\pi} p(\theta)\sin(\theta)d\theta = 4\pi \tag{8}$$

The Henyey-Greenstein phase function is parameterized by the asymmetry parameter g given by the following equation.

$$g = \frac{1}{4\pi}\int_0^{\pi} p(\theta)\cos(\theta)\sin(\theta)d\theta \tag{9}$$

When an arbitrary phase correlation function is given from Mie scattering calculations, the asymmetry parameter can be calculated from equation 9. Then, using the same asymmetry parameter and the Henyey-Greenstein function, the exact phase correlation function can be approximated. As a result, we can compute the following using a uniformly distributed random number s in the range from -1 to 1.

$$\cos\theta = \frac{1}{2g}\left[1 + g^2 - \left(\frac{1-g^2}{1+g^s}\right)^2\right] \tag{10}$$

The open-source MieScatter.jl code (Wilkman (2013)) was used to calculate the Mie scattering parameters. Q_{ext} is the extinction coefficient. ω_0 is the single-scattering albedo. g is the asymmetry parameter. The solution can be obtained by inputting the refractive index of the medium.

Generally, the size distribution of droplets in convective clouds is heterogeneous, and assuming a constant radius may be an excessive simplification. While the full radius spectrum is approximated with a single effective radius R, this radius can be made dependent on the scattering position. In the Light et al. (2001) model, each parameter is calculated using the following equation.

$$Q_{ext}(R) = 2 + bR^{-3/4} \tag{11}$$

$$w_0(R) = 1 - aR \tag{12}$$

$$g(R) = \frac{g_0 R}{R + R_0} \tag{13}$$

a_0、b_0、g_0、R_0 are the respective fitting parameters. The model solves the Mie scattering problem for radii in the range $1\mu\text{m} < R < 100\ \mu\text{m}$, fits the results to the above function, and uses these results to construct a non-uniform cloud model.

Next, we consider Rayleigh scattering. When optical radiation passes through paths within clouds or toward space platforms, it is also affected by interactions with atmospheric molecular components. In the case of Earth lightning discharges, this effect is largely negligible in certain wavelength ranges or when observing from satellite orbits toward the zenith. However, this model incorporates Rayleigh scattering. To calculate the scattering cross section for Rayleigh scattering, it is computed using the following equation based on Bodhaine et al. (1999).

$$\sigma_R = \frac{24\pi^3 F(air)}{\lambda^4 N_0^2}\left(\frac{n_s^2 - 1}{n_s + 2}\right)^2 \tag{14}$$

N_0 is the density of air at standard temperature and pressure. n_s is the refractive index under the same environmental conditions. $F(air)$ is a parameter related to Rayleigh scattering known as the King factor. For the Earth's atmosphere, it can be derived as follows from Peck & Reeder (1972).

$$10^8(n_s - 1) = 8060.51 + \frac{2480990}{132.274 - \lambda^{-2}} + \frac{17455.7}{39.32957 - \lambda^{-2}} \tag{15}$$

Note that the unit for λ is micrometers. The phase function for Rayleigh scattering is as follows.

$$p_R(\theta) = \frac{3}{4}(1 + \cos^2\theta) \tag{16}$$

Then, to inverse transform the cumulative probability distribution of $\cos^2\theta$, to sample the phase correlation function, we set it as follows.

$$cos\theta = w^{1/3} - w^{-1/3} \tag{17}$$

$$w = 2s + (4s^2 + 1)^{1/2} \tag{18}$$

Here, s is a uniformly distributed random number ranging from -1 to 1.

The collision rate for Rayleigh scattering is determined as follows based on the number density at altitude z.

$$\nu_R = cN(z)\sigma_R \tag{19}$$

At this point, when hydrostatic equilibrium holds, the number density at height z is H is determined from the scale height as follows.

$$N(z) = N_0 \exp(-z/H) \tag{20}$$

Regarding background absorption, specific wavelengths undergo significant absorption in the atmosphere. For a single absorbing substance, the statistical weight (intensity) between positions $\boldsymbol{r}_i - \boldsymbol{r}_{i+1}$ is calculated according to Beer-Lambert's law as follows:

$$w_{i+1}^{-} = w_i^{+} \exp\left(-\int_{\boldsymbol{r}_i}^{\boldsymbol{r}_{i+1}} \sigma_{abs} n_{abs}(\boldsymbol{r}) dr\right) \tag{21}$$

σ_{abs} is the absorption cross section, n_{abs} is the number density of absorbing particles. This model assumes that the number density depends only on altitude. In this case, the following equation can be used to calculate the change without directly computing the integral part.

$$M(z) = \int_0^z n_{abs}(z')dz' \tag{22}$$

$$\int_{\boldsymbol{r}_i}^{\boldsymbol{r}_{i+1}} \sigma_{abs} n_{abs}(\boldsymbol{r}) dr = \frac{\sigma_{abs}|M(z_{i+1}) - M(z_i)|}{|\mu_i^z|} \tag{23}$$

Here, μ_i^z is the z-component of the unit vector $\boldsymbol{\mu}_i$ and is a nonzero value.

This model employs a two-step process to obtain cloud composition at a specific location. First, it identifies the local properties of the cloud composition model at that location. Then, it calls calculation functions such as density to obtain the parameters required for computations like scattering. The reason for dividing the process into multiple stages is to avoid performing multiple calculations to obtain parameters like cloud particle size.

Finally, we perform these local calculations of scattering and absorption. After the ith photon collides with the scattering particle, the photon's flux energy is radiated in all directions according to the incident direction and phase function. Considering the surface area A of the device and the distance d_i between the scattering point and the observation device, the energy reaching the sensor is

$$\delta_i = \frac{A w_i^- p(\theta_i)}{4\pi d_i^2} \exp(-\tau_i). \tag{24}$$

It is normalized to the energy of a photon of a certain wavelength with unit weight. θ_i is the angle between the line of sight S_i from the scattering event location $\boldsymbol{r}_i$ to the instrument and $\boldsymbol{\mu}_{i-1}$. τ_i is the optical depth defined as follows.

$$\tau_i = \int_{S_i} \nu_{all}(s) ds \tag{25}$$

s is the coordinate indexing the line-of-sight direction S_i. ν_{all} is the rate that incorporates all effects, including Rayleigh scattering, Mie scattering, and background absorption. During simulation, either classify all δ_i by arrival direction to the detector for each coordinate to form an image, or classify them by arrival time $t_i' = t_i + d_i/c$ to simulate the photometer waveform. However, for typical cloud geometries, the integration path may traverse multiple cloud boundary regions, resulting in discontinuities in the Mie scattering component ν_{Mie}. To account for this, each segment is integrated discretely.

$$\tau_{i,Mie} = \sum_{k=1}^{n} \int_{S_k} S_{k+1} \nu_{Mie}(s) ds \tag{26}$$

2.3.2 Customization

One modification made in this study to the original CloudScat.jl enables the simulation of clouds composed of multiple constituents. To apply it to simulations of lightning on Venus and Jupiter, we modified the step identifying local cloud composition properties to randomly select the composition based on the number density of cloud particles. When implementing cross-section averaging, we avoid excessive averaging based on a single composition assumption by applying weights to specific cross sections according to their number density. This modification enables adaptation to cases where cloud compositions, such as those on Jupiter, consist of multiple components beyond just water ice.

The second modification was to adapt the phase function to the One-Term Henyey-Greenstein phase function, enabling consideration of the Two-Term HG (TTHG) phase function as well. TTHG can be expressed as in Equation (27) using the ratio f of forward and backward scattering, and the respective asymmetry parameters g_1 and g_2.

$$p_{TTHG}(\theta) = f\frac{1-g_1^2}{(1+g_1^2-2g_1\cos\theta)^{3/2}} + (1-f)\frac{1-g_2^2}{(1+g_2^2-2g_2\cos\theta)^{3/2}} \tag{27}$$

TTHG can independently adjust both forward and backward scattering, making it highly adaptable to complex scattering characteristics compared to OTHG or isotropic scattering. It can highly reproduce realistic scattering characteristics found in nature, such as those of the atmosphere, cloud particles, and biological tissues. Due to the large number of parameters, it can reproduce diverse scattering behaviors, and TTHG can fit observational data with high precision. When prior research has advanced the validation of TTHG, utilizing TTHG enables more accurate validation. For the Venus and Jupiter models, we are comparing and verifying two types: OTHG and TTHG.

The default settings and parameters for CloudScat.jl (Light et al. (2001)) are configured for the Earth lightning-induced scattering model. Next chapter organizes parameters for models used on Venus and Jupiter. For both profiles, cloud particles are assumed to be perfectly spherical. The atmosphere is assumed to be in hydrostatic equilibrium.

2.3.3 Model parameters of Venus

The wavelength of lightning emissions considered in the model is set to 777 nm based on prior research. The scale height of Venus's atmosphere is set to $H_V = 15.9$ km. The composition of Venus's atmosphere is shown in Table 2.7, referencing NASA's Factsheet. Alongside this, we also present previous studies that referenced the King correction factor for each component.

Table 2.7: List of parameters related to Rayleigh scattering in the Venus atmosphere.

Gas	VMR [%]	King correction factor F	Note
CO_2	96.5	1.141	Sneep et al., 20024
N_2	3.5	1.035	Thalman et al. ,2014
SO_2	0.015	1.063	Bogaard et al., 1978
Ar	0.007	1.000	Thalman et al., 2014
H_2O	0.002	1.001	Hill et al., 1986, Polyanskiy et al., 2016

The number density of cloud particles on Venus is being observed by the Particle Size Spectrometer mounted on the Pioneer Venus LARGE probe(Knollenberg & Hunten (1980)). Based on these observational results, Venusian cloud particles are distinguished into multiple modes across three layers, based on their presumed formation processes and particle radii. From Knollenberg & Hunten (1980), Based on the cloud formation and dissipation processes, Mode 1 is presumed to be sulfur in the upper layer and sulfuric acid in the lower layer, Mode 2 is sulfuric acid, Mode 3 is sulfuric acid, chloride, and solid $NOSHO_4$.

In the models of previous studies, a distribution assuming that the composition of cloud particles in all modes consists of spherical aerosols primarily composed of sulfuric acid solution has been used. In this study, we adopted the altitude distribution of cloud particle number density from a model (Haus et al. (2013)) based on analysis results of spectral image data from the Visible and Infrared Thermal Imaging Spectrometer (VIRTIS) onboard Venus Express and infrared spectral data observed by the Profile Measuring instrument for Venus (PMV) onboard VENERA-15. Figure 2.13 shows the altitude distribution of cloud particle number density for each mode adopted in this model. Table 2.8 lists the parameters for the equations used to reproduce the model.

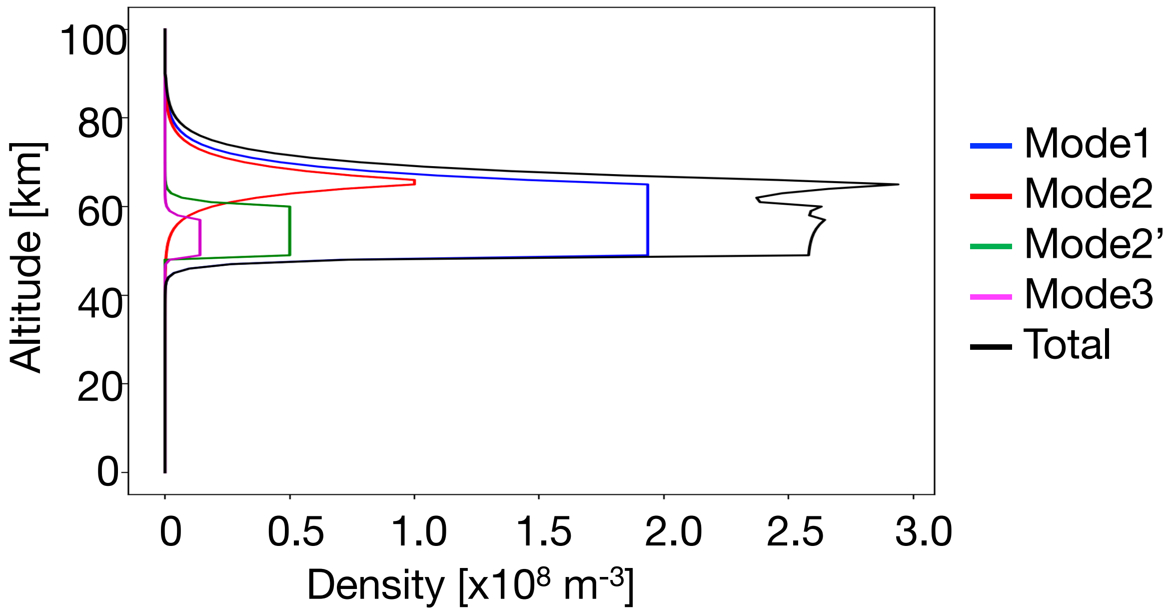

Figure 2.13: Standard model of cloud particle distribution with altitude based on Haus et al. (2013), Haus et al. (2014) and Haus et al. (2015). Solid lines indicate the generation state (Mode 1, 2, 2' , and 3) number density of each cloud particle. The black solid line indicates the sum of each model.

Table 2.8: List of model parameters for the cloud structure of Venus (Haus et al. (2013), Haus et al. (2014), Haus et al. (2015)).

Mode	1	2	2'	3
Lower base of peak altitude z_b [km]	49.0	65.0	49.0	49.0
Layer thickness of constant peak particle number z_c [km]	16.0	1.0	11.0	8.0
Upper scale height H_{up} [km]	3.5	3.5	1.0	1.0
Lower scale height H_{lo} [km]	1.0	3.0	0.1	0.5
Particle number density N_0 at z_b [cm^{-3}]	193.5	100	50	14

$$N(z) = \left\{ \begin{array}{ll} N_0(z_b)\exp(-(z-(z_b+z_c))/H_{up}) & ,z > (z_b+z_c) \quad (28) \\ N_0(z_b) & ,(z_b+z_c) \geq z \geq z_b \quad (29) \\ N_0(z_b)\exp(-(z_b-z)/H_{lo}) & ,z \leq z_b \quad (30) \end{array} \right\}$$

Additionally, we also employed a model (Karyu et al. (2024)) that incorporates high-altitude haze. Figure 2.14 shows the vertical distribution of number density and cloud particle of Venusian cloud.

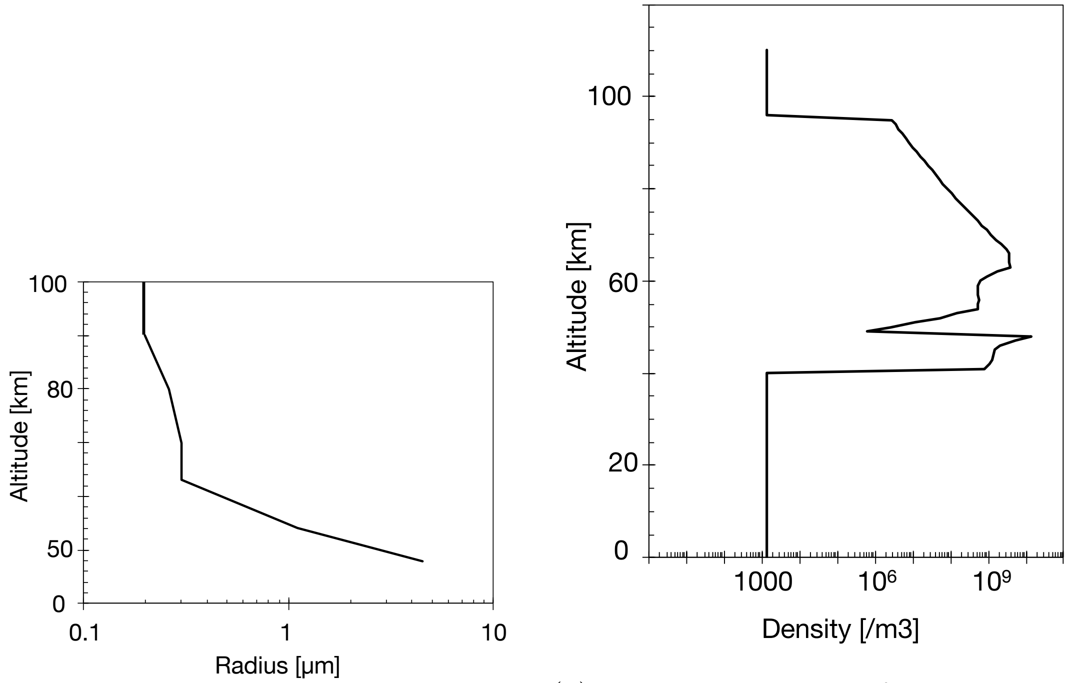

(a) The radius of cloud particle.

(b) The number density of total cloud particles.

Figure 2.14: Model including uppermost haze distribution with altitude based on Karyu et al. (2024). (a) radius of cloud particle. (b) The number density of total cloud particles.

This model considering the uppermost haze observed by Venus Express (Takagi et al. (2019)). Haus et al. (2013)'s model didn't consider the haze above 100 km altitude. This study assumes that these hazes are also composed of H_2SO_4

Table 2.7 shows the refractive index of H_2SO_4 The refractive index of Venusian cloud particles is estimated from polarization observations Coffeen & Gehrels (1969). From

Table 2.9: List of complex refractive indices of clouds on Venus

Particle	Complex refractive index at 656 nm	Note
H_2SO_4	$1.440+1\times10^{-8}i$	Cofeen and Gehrels 1969 Hansen and Hovenier 1974 Palmer and Williams 1974, 1975

Hansen & Travis (1974), the real part of the complex refractive index is estimated from the Mie particle multiple scattering model. In this model, the real part of the complex refractive index is set to 1.44. In the visible light range, including the 777 nm wavelength of the lightning discharge under consideration, the imaginary part of the complex refractive index is nearly zero. This time, 10^{-8} is adopted.

Table 2.10 shows the calculated results for the cloud particle radius adopted in this model, along with the dissipation coefficient, absorption coefficient, and asymmetry parameter calculated from that radius.

Table 2.10: List of properties of Venusian cloud particles.

Mode	Radius [μm]	Extinction parameter Qext	Absorption parameter Qabs	Asymmetric parameter g
1	0.5	2.0959	1.3253×10^{-3}	0.64
2, 2'	1.4	2.8275	4.3508×10^{-3}	0.69
3	3.65	2.3732	1.1642×10^{-2}	0.77

The parameters used for TTHG are based on the refractive index of 1.44 for the primary sulfate particles in Venusian clouds, the results of calculations using Mie theory with values ranging from 1.41 to 1.45, and the values obtained from TTHG fitting: $f = 0.975$, $g_1 = 0.8$, $g_2 = -0.8$. Figure 2.15 shows a plot comparing the TTHG phase function used and the results from Mie theory.

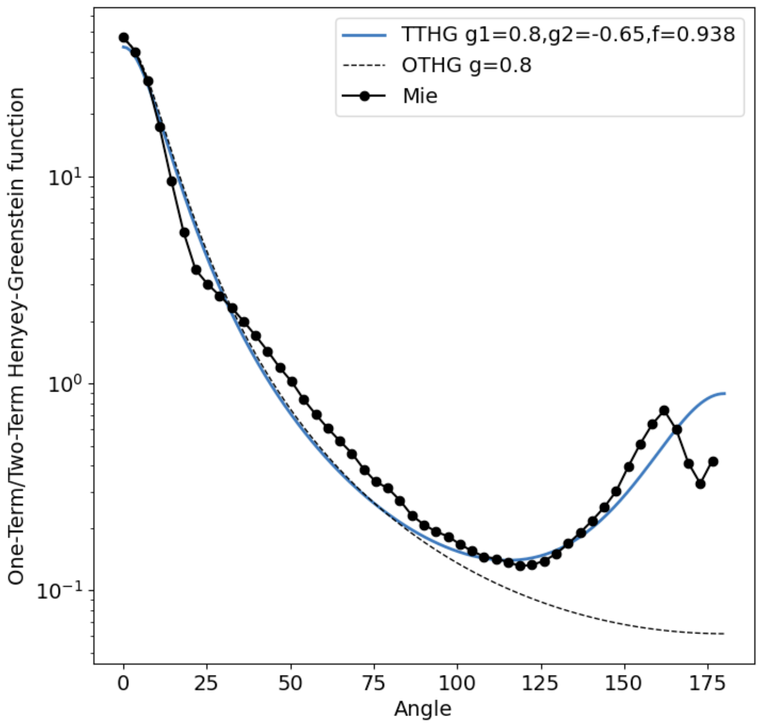

Figure 2.15: Comparison of the phase functions and Mie scattering models for Venus cloud models. The solid black line and black circle markers indicate Mie theory results, the dashed black line indicates OTHG results, and the solid blue line indicates TTHG results.

This TTHG was used for both models. The OTHG fitted from the parameters of the Mie theory was only used in the model with the first H_2SO_4 cloud.

2.3.4 Model parameters of Jupiter

Assuming hydrostatic equilibrium holds in Jupiter's atmosphere, the scale height of Jupiter is taken as $H_J = 27.0$ km. The composition of Jupiter's atmosphere is also shown in Table 2.11, referencing NASA's Factsheet. Alongside this, we also present previous studies that referenced the King correction factor for each composition.

Table 2.11: List of parameters related to Rayleigh scattering in the Jupiter atmosphere.

Gas	VMR [%]	King correction factor F	Note
H_2	89.8	1.032	Peck et al., 1977
He	10.2	1.000	Thalman et al., 2014
CH_4	0.3	1.000	Sneep et al., 2005
NH_3	0.026	1.004	Cuthbertson et al., 1914 Hohm et al., 1993

The altitude distribution of cloud particle number density on Jupiter is based on cloud mass ratios obtained from a cumulonimbus formation simulation model that incorporates chemical reactions in humid atmospheric compositions Sugiyama et al. (2014). In this model, while radiative forcing is simplified, it incorporates various condensing gases and cloud microphysical assumptions, enabling long-term integration of cloud activity. This yields the statistical vertical distribution of cloud particle sizes during active and quiescent periods of cumulonimbus clouds. Furthermore, in the prior study Dyudina et al. (2002) concerning lightning scattering models, a comparison was conducted by reproducing two-dimensional images with the optical thickness estimated from the global average atmosphere, as inferred from observations by the Galileo probe, and defining the spread using the HWHM. However, the discussion does not address the FWHM of the light curve, nor does it consider the vertical distribution of cumulonimbus clouds. Their model does not account for cloud layers below the luminous altitude, and if the same model is used to consider whether photons reach the observer delayed after scattering or to examine the light curve, cloud structure is a critical variable. Sometimes the FWHM may be underestimated. In this study, we compare multiple model setups from Sugiyama's paper as reference for the vertical distribution of cloud particle number density in cumulonimbus clouds. Model set names: R10S3's active phase (Active) was adopted as the cloud structure of cumulonimbus clouds, while R10S3's quiet phase (Quiet), where cumulonimbus clouds do not develop, was adopted as the cloud number density distribution around steady-state cumulonimbus clouds. Additionally, for comparison, results from the model R10S10—which increases the lower-level condensation components compared to R10S3—were also verified for its Active and Quiet phases. In this study, cloud particles are assumed to be spherical, so the number density can be calculated from the mass ratio and the formula for the mass of a sphere as follows.

$$n_i = \frac{\nu_i \times \rho_{atm}}{m_i \times \kappa_{\text{model}}} \tag{31}$$

$$m_i = \frac{4\pi r_i^3}{3}\rho_i \tag{32}$$

n_i is the number density of a given composition. ν_i i the mixing ratio, ρ_{atm} is atmospheric density, m_i is the mass of the spherical cloud particle, κ_{model} is the correction coefficient for the simulation model results. In the simulation, the radiative cooling rate was intentionally amplified to approximately ten times that of real Jupiter to enhance computational efficiency. This likely resulted in an overestimation of cloud density. Their cloud convection simulation suggests that the average cloud density is broadly proportional to the radiative cooling rate. Based on these relationships, κ_{model} is the coefficient used to correct for the actual cloud density. $\kappa_{\text{model}} = 0.1$ was adopted. The radius, density, and mass of each particle are shown in Table 2.12. Based on the value of Table 2.12, Figure 2.16 shows the cloud particle number density altitude distribution converted from the mass ratio.

Table 2.12: List of properties of Jovian cloud particles.

Particle	Radius r_i [μm]	Density ρ_i [g/cm^3]	Weight m_i [g/particle]	Note
H_2O	10.0	0.917	3.84×10^{-9}	Lide et al., 2003
NH_3	0.5	0.817	4.28×10^{-13}	Blum et al., 1975
NH_4SH	3.0	1.17	1.32×10^{-10}	West et al., 1934

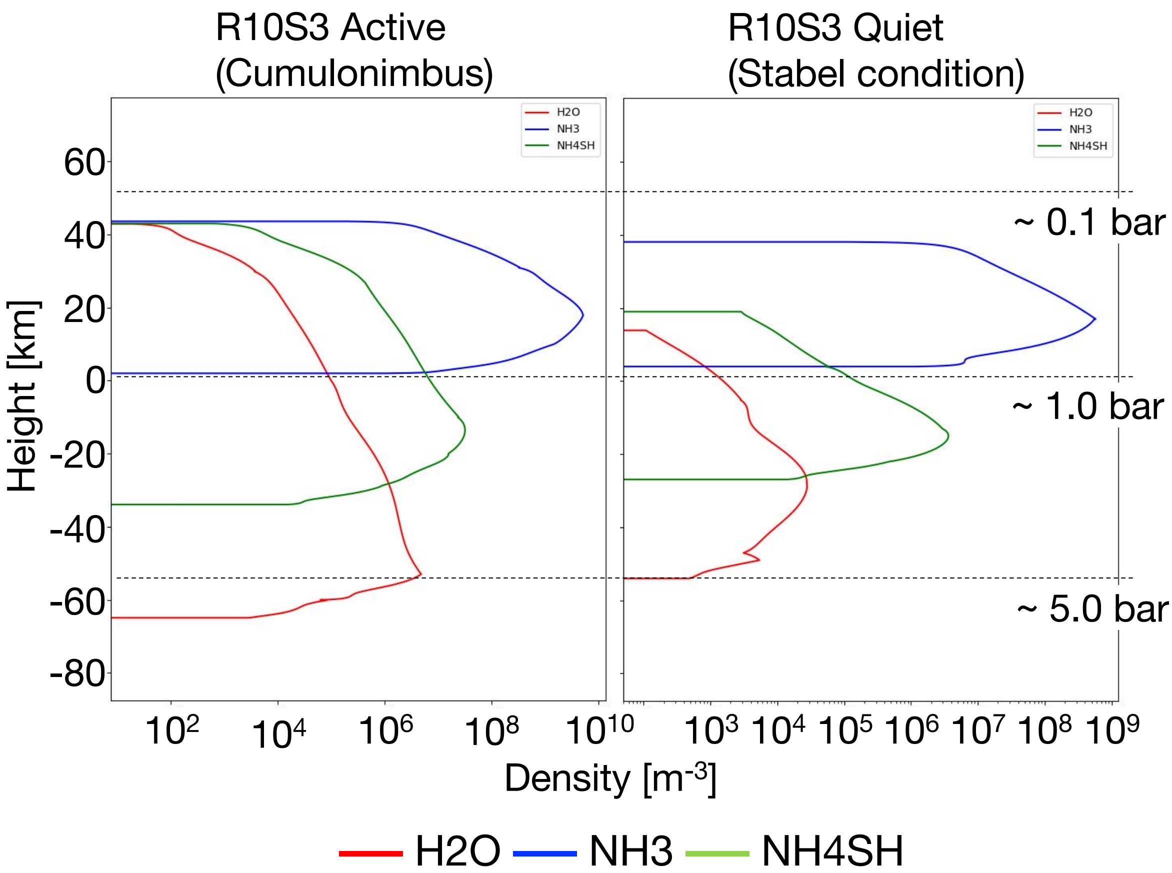

Figure 2.16: Vertical number density profile of Jovian cloud used in the model. The red solid line indicates the water cloud. The blue solid lineindicates the ammonia cloud. The green solid line indicates the ammonium hydrosulfide cloud. (Left) shows the cumulonimbus following R10S3 active, and (Right) shows the stable condition following R10S3 quiet based on Sugiyama et al. (2014).

Table 2.13: List of complex refractive indices of clouds on Jupiter

Particle	Complex refractive index	Note
H_2O	$1.33 + 1.78 \times 10^{-8}i$	Hale and Querry 1973
NH_3	$1.44 + 1.00 \times 10^{-8}i$	Hudson et al., 2022, 100 K (Crystalline NH3)
NH_4SH	$2.30 + 1.00 \times 10^{-10}i$	Howett et al., 2006 and 2007

Regarding the asymmetry parameters of TTHG compared in the table, Figure 2.17 compares the two TTHG cases studied here for each phase angle.

Table 2.14: List of parameters for the Two-Term Henyey-Greenstein function.

No.	g_1	g_2	f	Note
1	0.80	-0.750	0.954	Tomasko et al., 1978 (From Pioneer 10 images) STZ 440 nm, 640 nm average result
2	0.453	-0.801	0.980	Hegn et al., 2021 From Cassini images at 650 nm

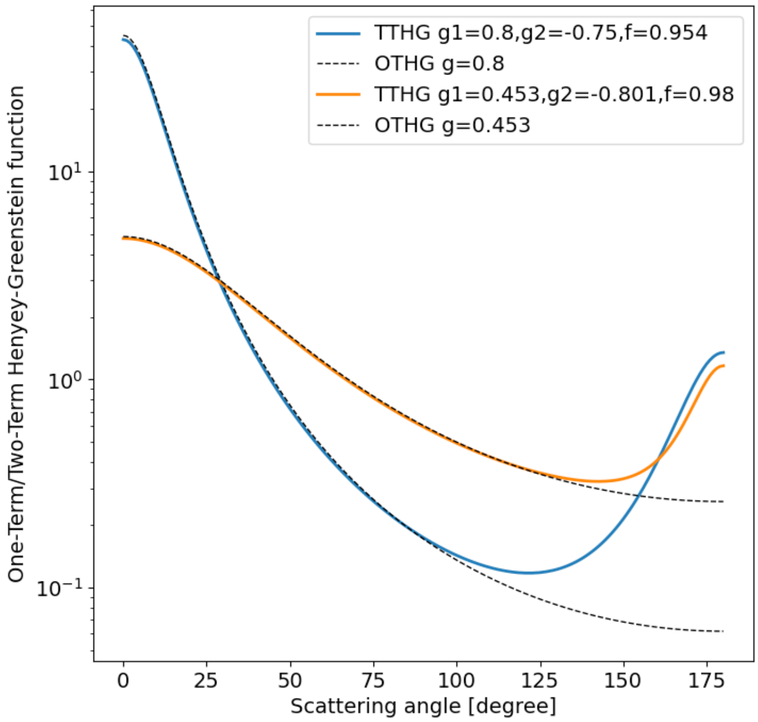

Figure 2.17: Comparison of the phase functions for Jupiter cloud models. Blue and orange lines show the results of TTHG. Black dashed lines show the corresponding OTHG for reference.

From the TTHG comparison results diagram, it can be seen that the backscattering is larger beyond 130 degrees compared to OTHG. Due to the larger proportion of backscattering, the TTHG results are expected to exhibit a longer FWHM compared to the scattering waveforms simulated with OTHG. The first TTHG parameter is the average value of parameters calculated based on images of Jupiter's banded structure obtained at two wavelengths, 440 nm and 640 nm, using the imager aboard Pioneer 10, as adopted in Dyudina et al. (2002). The second parameter uses the results of the phase function estimated by reanalyzing Cassini's imager data near the thunderstorm wavelength of 650 nm. This allows us to confirm the phase function's dependence while also comparing which yields more valid results for discussing Jupiter's cumulonimbus clouds.

2.3.5 Model parameters of Earth

All cloud particles were thought to be formed by water ice. Therefore, cloud particles primarily utilize the optical properties of water. Factors other than clouds, such as the ozone layer and dust, are not taken into account. Earth is easier to observe directly than Venus or Jupiter, so numerous measurement examples and simulation examples exist. In this study's model, we assumed a cloud profile that takes into account the stage of cumulus cloud development, referencing results from such as Park et al. (2024), Morrison et al. (2020), Ryohei Misumi (2008), Hartmann et al. (2018), and so on.

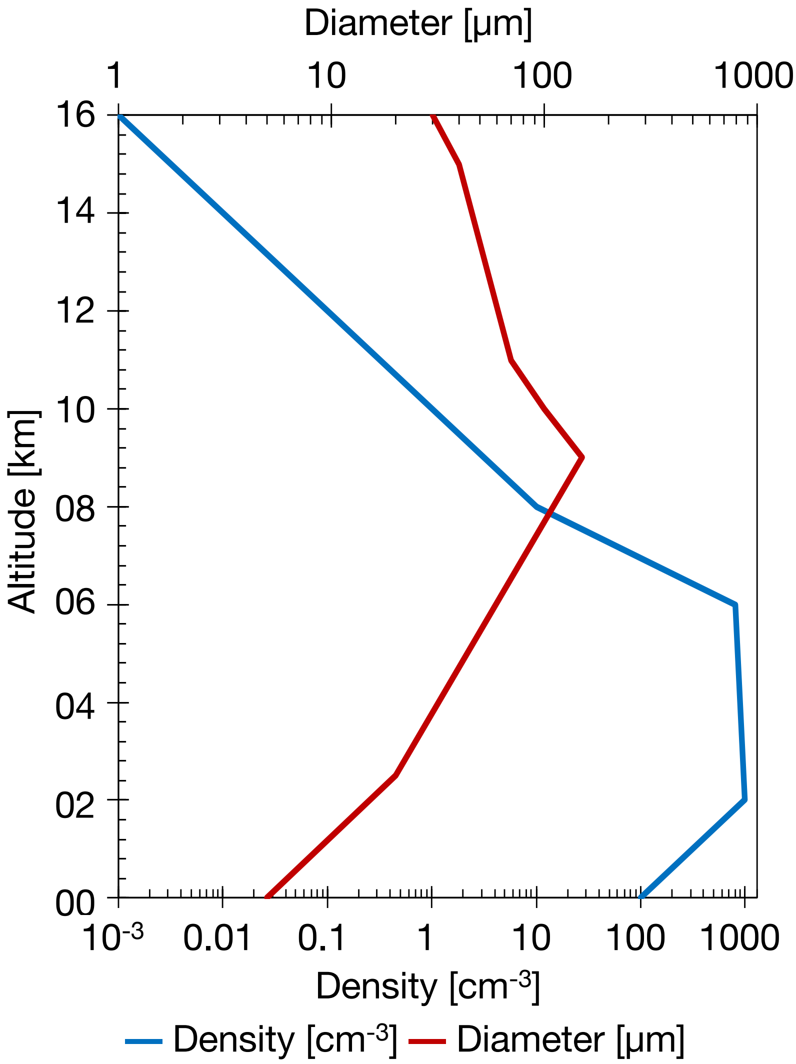

Figure 2.18: Vertical number density and radius profile of the Earth cloud used in the model. The blue solid line indicates the density of cloud particles. The red solid line indicates the diameter of the cloud particle. In this model, considering the water cloud.

We assumed that the diameter of cloud particles increases with altitude and the density decrease with altitude higher than cloud bottom. Informed by the formation model of tropical anvil clouds, it was assumed that water particles transform into ice and decrease in size at altitudes above 9 km.

The variables of the TTHG phase function were set to $g_1 = 0.8792$, $g_2 = -0.9835$, and $f = 0.9832$ based on the results of based on Kattawar (1975). Actually, more recent studies (e.g., Kokhanovsky (2004)) employ more complex phase functions rather than TTHG to better capture the strong forward peak and some backscatter enhancement of realistic cloud phase functions. In this study, TTHG was adopted to align with the fitting performed using TTHG in the previous models of Jupiter lightning. Therefore, it is necessary to note that differences remain between the measured phase function and the observed increase/decrease in backscattering and enhancement in forward scattering. This study omits physical discussion of the differences in these phase functions.

3 Results

3.1 Venus

3.1.1 Observation results of Venus

Venus is an inner planet, so the period during which its night side can be observed is limited by the phase angle formed by the Sun, Venus, and Earth. For this observation, we conducted observations until the period when approximately 50% of the Venus disk was night side, meaning around one week before and after the period when the maximum angular separation was reached and then reached maximum again. However, when the angular separation between the Sun and Venus is small, damage can occur to the telescope's primary and secondary mirrors. Therefore, observations cannot be made around the time of Venus's inferior conjunction, when it approaches Earth, to protect the telescope. Based on empirical rules, the observation period was restricted to times when the angular separation was greater than 20 degrees. Table 3.1 shows the Venus observation results. Observation times are limited to periods around sunrise and sunset, as well as daytime. During observations when Venus's altitude is low, the image is significantly affected by atmospheric turbulence and seeing conditions, causing the crescent portion of the Venusian disk to wobble considerably. As a result, the wobbling image was captured within the PLD's field of view, causing contamination. In reality, contamination from Venus's daytime surface is most severe immediately after sunrise and sunset. Consequently, most valid observational data comes from daytime observations, and there is virtually no data where standard stars or comparison stars were observed simultaneously with Venus. A total of 309 minutes of observation was conducted. Unless observations were performed during the relatively dark hours of dawn or dusk, the amplitude of noise caused by sky brightness became extremely large, limiting the observable time to about Air Mass of 2.

Table 3.1: Summary of PLD observation results for Venus

Date	Time [min]	Filter [nm]	Weather	Airmass
20220124	20	777, 700	Clear	2.8
20220127	31	777, 700	Clear	2.1
20220131	69	777, 700	Clear	2
20220210	20	777, 700	Clear	2.9
20220211	51	777, 700	Clear	2.2
20220215	43	777, 700	Fine	2
20220309	30	777, 700	Clear	2.3
20220312	45	777, 700	Clear	2.1

Figure 3.1, 3.2, 3.3, 3.4, 3.5 show the cumulative distribution of the bandpass processing results for each timescale obtained by applying the analysis method described in Section 2.1.7 to the observational data shown in Table 3.1.

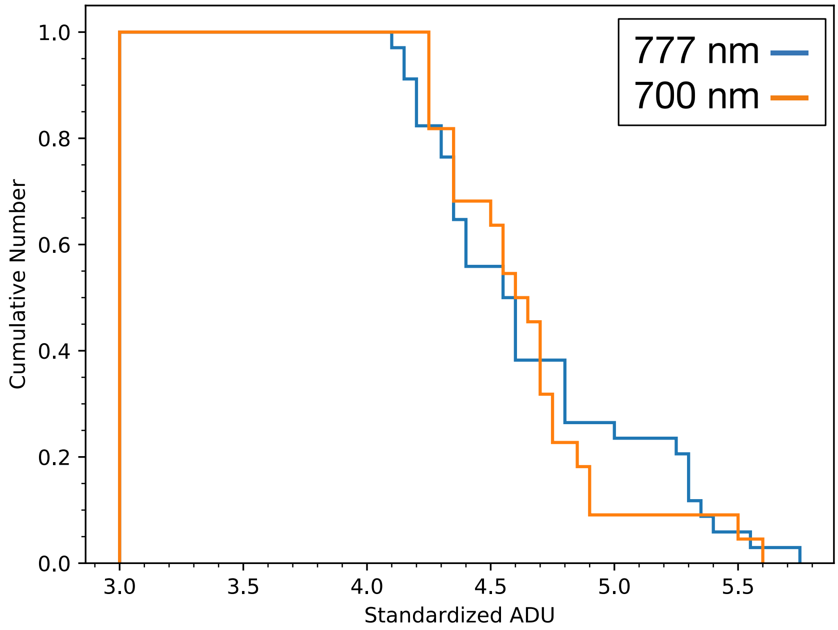

Figure 3.1: Cumulative distribution of Venus observed results on a 10-msec scale.

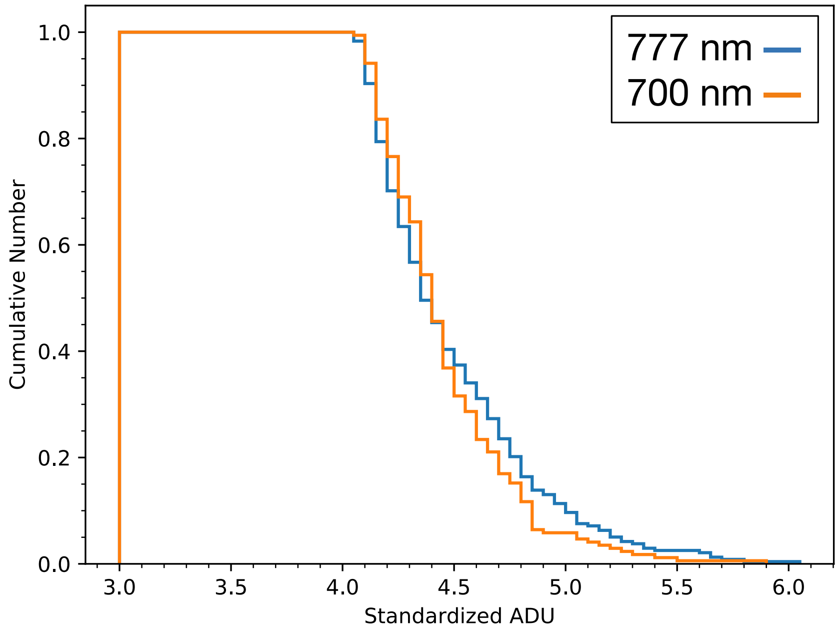

Figure 3.2: Cumulative distribution of Venus observed results on a 50-msec scale.

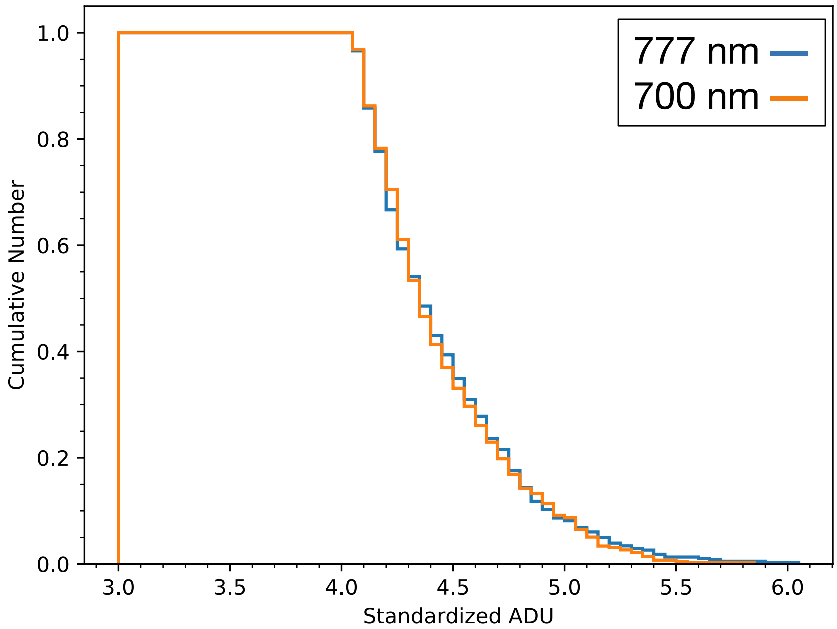

Figure 3.3: Cumulative distribution of Venus observed results on a 100-msec scale.

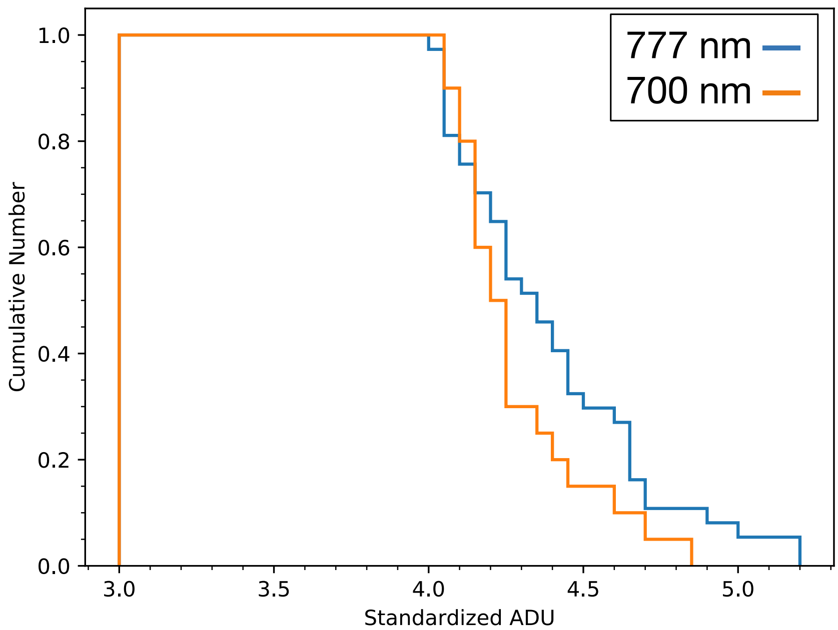

Figure 3.4: Cumulative distribution of Venus observed results on a 200-msec scale.

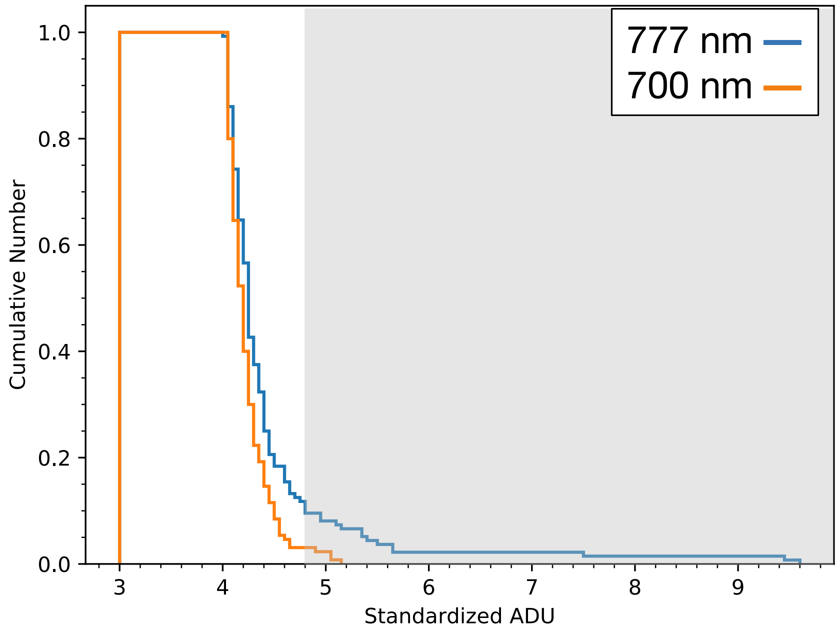

Figure 3.5: Cumulative distribution of Venus observed results on a 5-msec scale. The gray-shaded area indicates outlier events.

The cumulative distribution comparison of extraction results at 10, 50, 100, and 200 msec scales showed p-values of 0.2 or higher for all distributions obtained via the KS test. However, for the 5 msec scale events shown in Figure 3.5, comparing events where the maximum triggered event value exceeded 4.8 times the standard deviation, the p-value was approximately 0.03 in the gray-shaded region. Therefore, we confirmed waveforms for events exhibiting peak values exceeding 4.8 times the standard deviation. Figures 3.6 and 3.7 show two examples of waveforms with large peak values triggered. These waveforms exhibited values exceeding the threshold at only one point within the gate time.

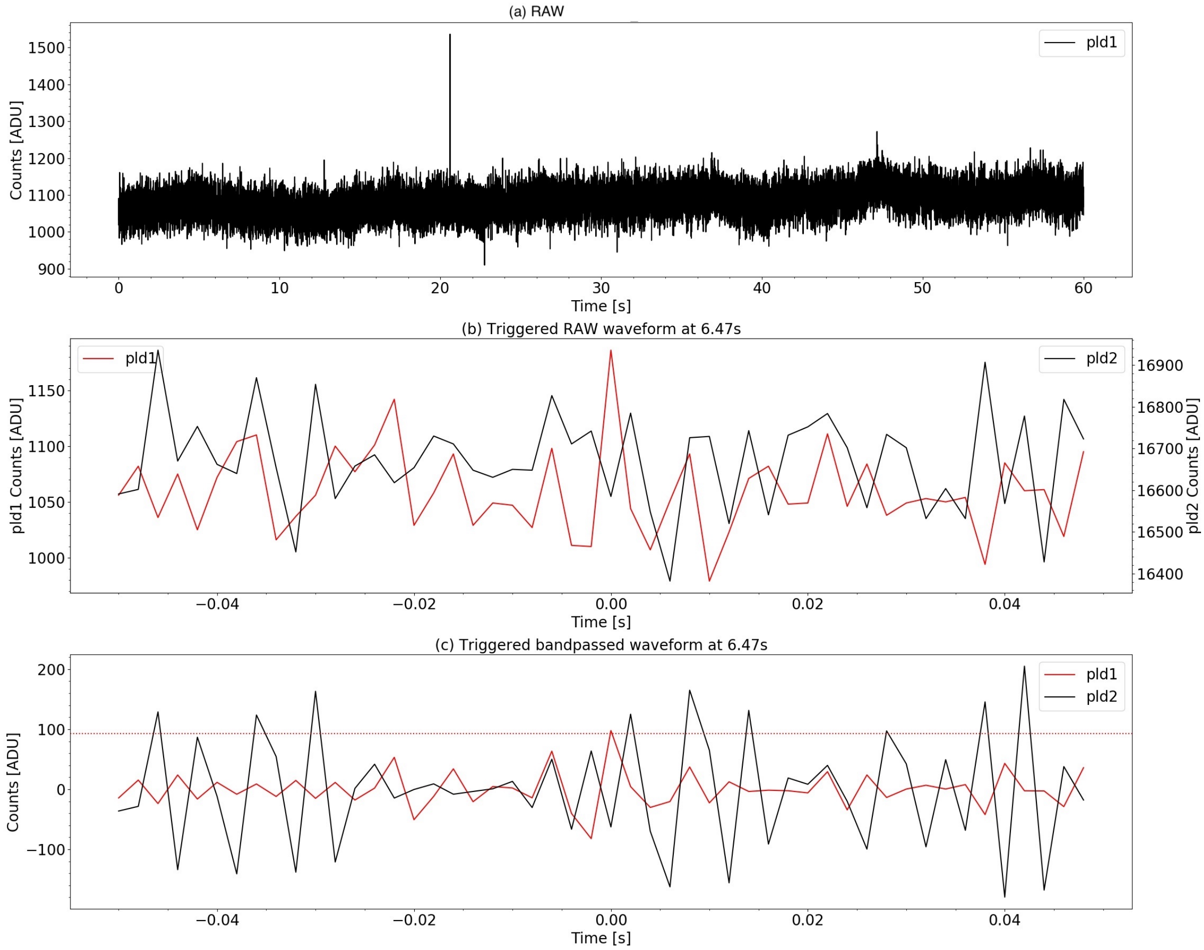

Figure 3.6: Recorded raw waveform data, an enlarged view of the selected interval, and the processed waveform after data reduction in Venus observation results on 2022-01-31 12:16:21 JST. (Top) The black solid line indicates the light curve at 777 nm. (Middle and bottom) The black solid line indicates the light curve at 700 nm. The red solid line indicates the light curve at 777 nm for Venusian lightning.

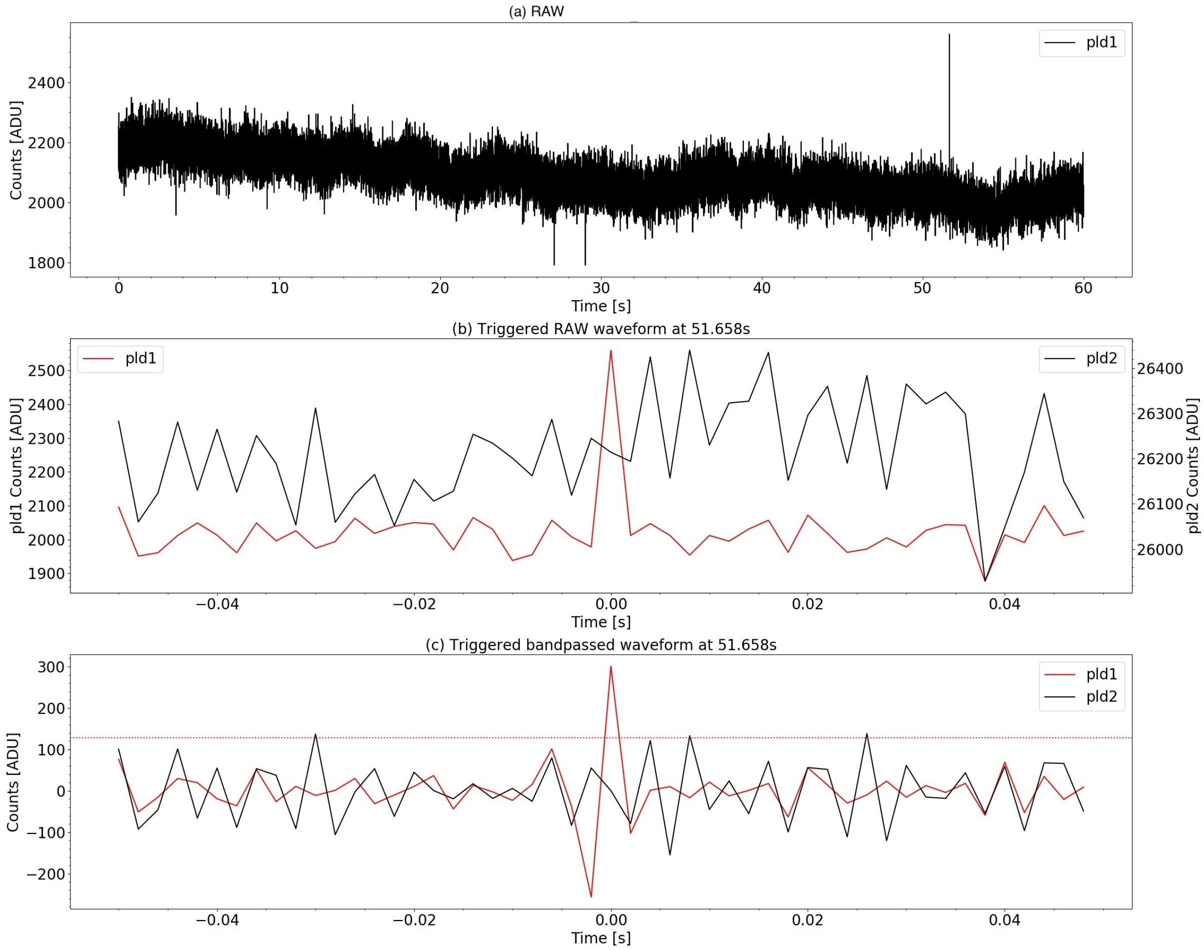

Figure 3.7: Recorded raw waveform data, an enlarged view of the selected interval, and the processed waveform after data reduction in Venus observation results on 2022-01-27 12:01:32 JST. (Top) The black solid line indicates the light curve at 777 nm. (Middle and bottom) The black solid line indicates the light curve at 700 nm. The red solid line indicates the light curve at 777 nm for Venusian lightning.

The waveform actually applied to the trigger was the result of applying the bandpass processing shown at the bottom of Figure 3.6 and Figure 3.7. Upon examining the trigger waveform, it showed its maximum value at only one data point in the PCH. Further investigation was required to conclude that this waveform was lightning-derived. If it was indeed lightning-derived, the lightning emission duration was estimated to be around 2 msec, the exposure time, or less than 4 msec.

The estimated emission intensity, along with the FWHM, for the waveform triggered by the Venus observation results is shown in Table 3.2.

Table 3.2: Summary of triggered waveforms of Venus

Date (JST)	Energy [J]	FWHM [ms]	sub-longitude	Distance [km]
2022/01/27 12:01:32	1.23×10^9	< 2	0.59	4.71×10^7
2022/01/31 10:45:35	5.34×10^8	< 2	6.05	5.00×10^7
2022/03/09 07:18:40	1.40×10^9	< 2	81.9	8.81×10^7
2022/01/31 12:16:21	4.51×10^8	< 2	6.14	5.00×10^7

We estimated the occurrence frequency assuming the triggered waveform originates from lightning with previous studies. The number of waveforms triggered by Venus was four, with a total observation time of 309 minutes. The average observation area was 3×10^7 km^2. Based on these results, the observation frequency by PLD was calculated as 7.2×10^{-12} /km^2/sec. This result is consistent with the estimated occurrence frequency of approximately one event per observation period from previous studies. Although the value obtained in this study agrees in order of magnitude with previous research results, it is quantitatively about 2.6 times larger.

3.1.2 Simulation results of Venus

Simulation results for a lightning flash scattering model occurring at various altitudes in Venus's atmosphere are shown. Since Venus possesses a solid surface, the surface was defined as altitude $z = 0$ km. The model assumes lightning occurs as point sources at altitudes of 30, 50, and 60 km within Venus's troposphere.

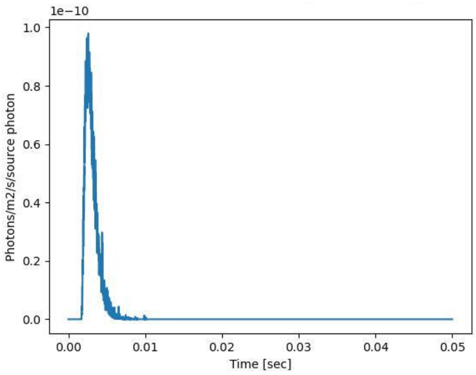

(a) Simulated light curve

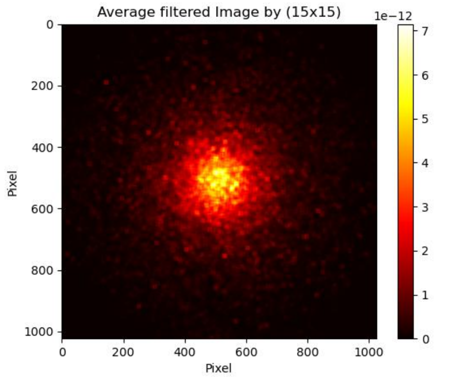

(b) Simulated image

Figure 3.8: Simulation results showing the light curve and image of Venusian lightning at an altitude of $z = 30$ km. (a) Simulated light curve. (b) Simulated image. The image was processed using an averaging filter.

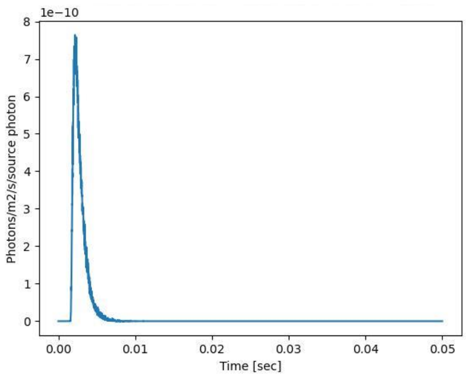

(a) Simulated light curve

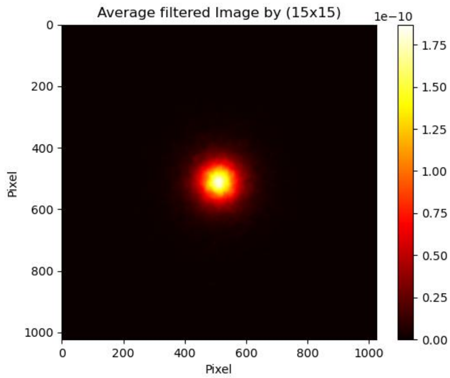

(b) Simulated image

Figure 3.9: Simulation results showing the light curve and image of Venusian lightning at an altitude of $z = 50$ km. (a) Simulated light curve. (b) Simulated image. The image was processed using an averaging filter.

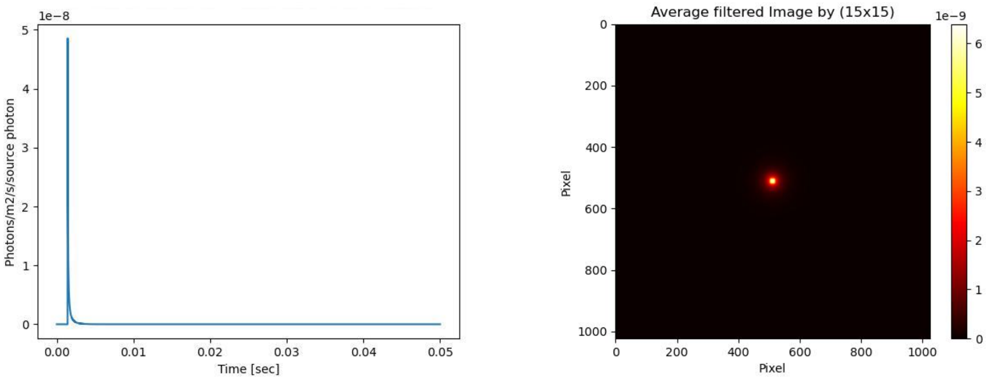

(a) Simulated light curve (b) Simulated image

Figure 3.10: Simulation results showing the light curve and image of Venusian lightning at an altitude of $z = 70$ km. (a) Simulated light curve. (b) Simulated image. The image was processed using an averaging filter.

Next, we show the waveform of the results obtained using TTHG.

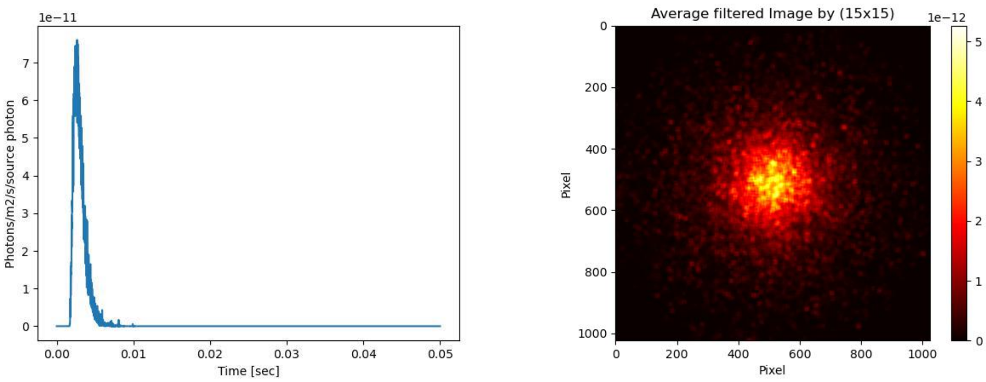

(a) Simulated light curve (b) Simulated image

Figure 3.11: Simulation results showing the light curve and image of Venusian lightning at $z = 30$ km, with TTHG. (a) Simulated light curve. (b) Simulated image. The image was processed using an averaging filter.

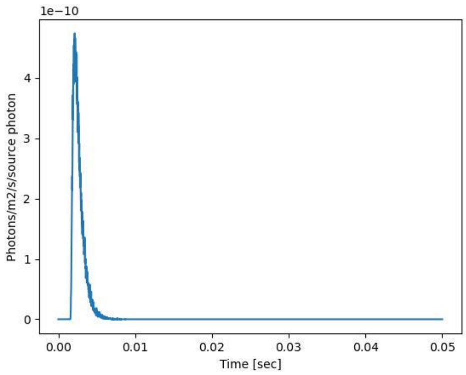

(a) Simulated light curve

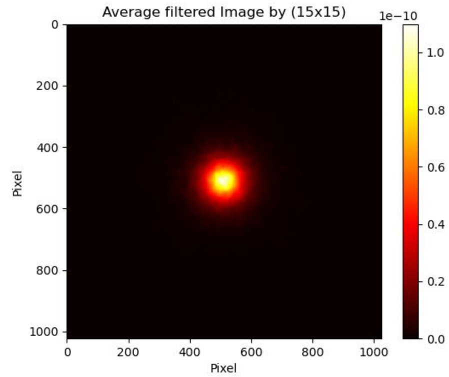

(b) Simulated image

Figure 3.12: Simulation results showing the light curve and image of Venusian lightning at $z = 50$ km, with TTHG. (a) Simulated light curve. (b) Simulated image. The image was processed using an averaging filter.

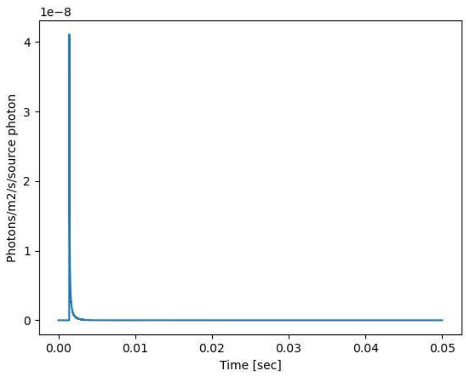

(a) Simulated light curve

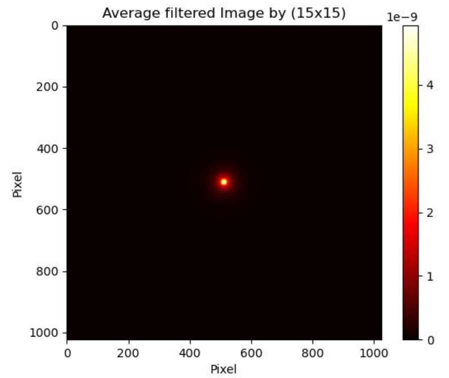

(b) Simulated image

Figure 3.13: Simulation results showing the light curve and image of Venusian lightning at $z = 70$ km, with TTHG. (a) Simulated light curve. (b) Simulated image. The image was processed using an averaging filter.

Figure 3.14 plots the relationship between altitude and FWHM, where the lightning flash duration is defined as the FWHM of the light curve obtained from the simulation.

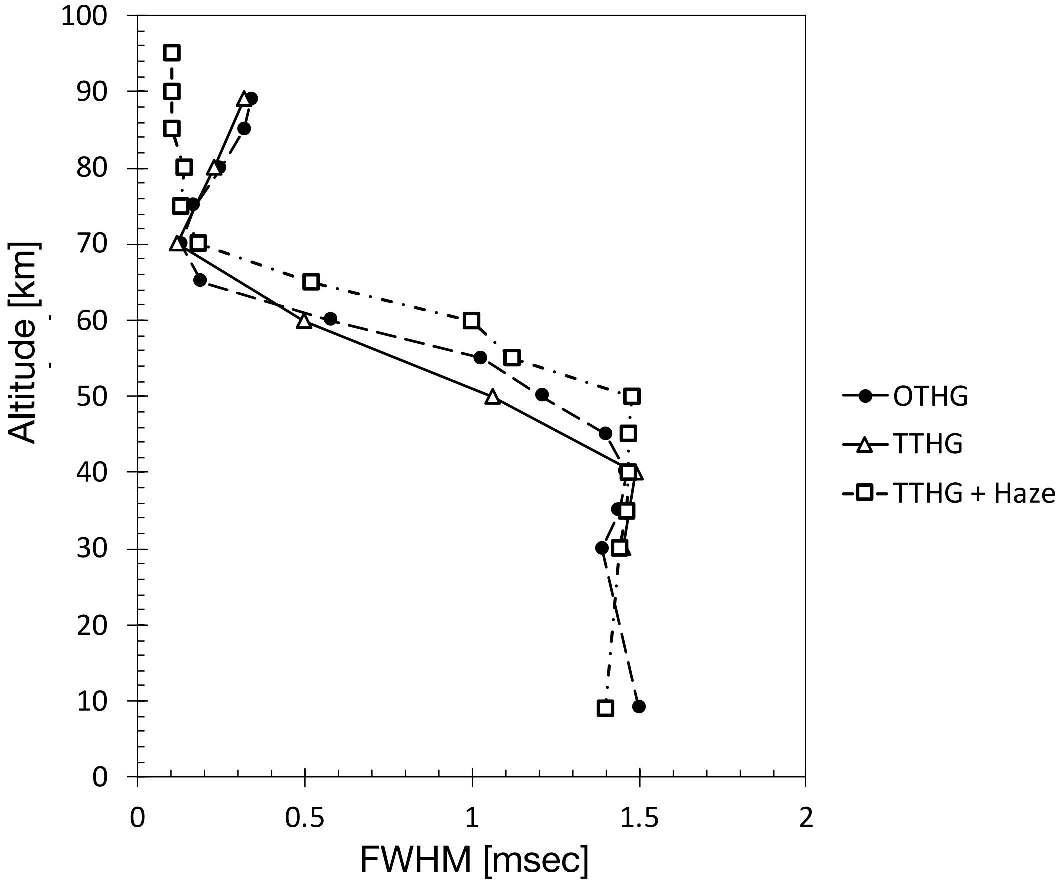

Figure 3.14: Relationship between the Full Width at Half Maximum (FWHM) of the simulated light curves and altitude of the light source, assuming lightning for Venus.

From Figure 3.14, the full width at half maximum (FWHM) duration of lightning discharges occurring at an altitude of 30 km is 1.5 msec. The duration of lightning discharges saturates at altitudes of 40 km or below.

Figure 3.15 shows the plot of the relationship between the spread HWHM of the lightning zenith observation image obtained from the calculation results and the occurrence altitude.

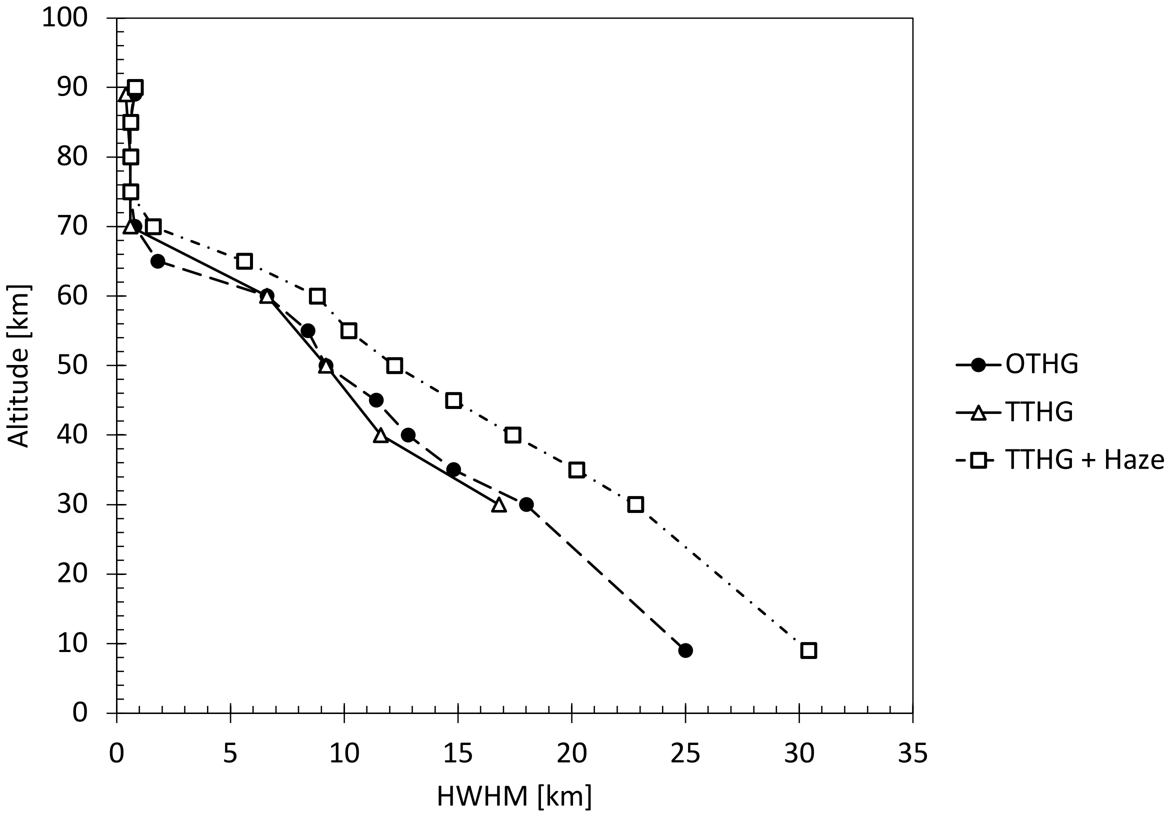

Figure 3.15: Relationship between the Half-Width at Half Maximum (HWHM) of the simulated images and altitude of the light source, assuming lightning for Venus.

The relationship between HWHM and altitude can be expressed by a linear equation, and it was found that HWHM $= -0.41z + 31.5$, indicating a linear relationship. HWHM is the point spread function in kilometers, z is the occurrence altitude in kilometers.

In the model used this time, no difference greater than 2 km or 0.5 msec was observed in either HWHM or FWHM due to differences in the phase functions of OTHG and TTHG. Results consistent with previous transmission model studies discussing Venusian cloud radiation transfer using OTHG with parameters estimated by Mie theory, excluding specific wavelengths such as CO_2, were obtained.

The difference in observed flux resulting from placing point light sources at various heights indicates the transmission rate of lightning flashes affected by scattering.

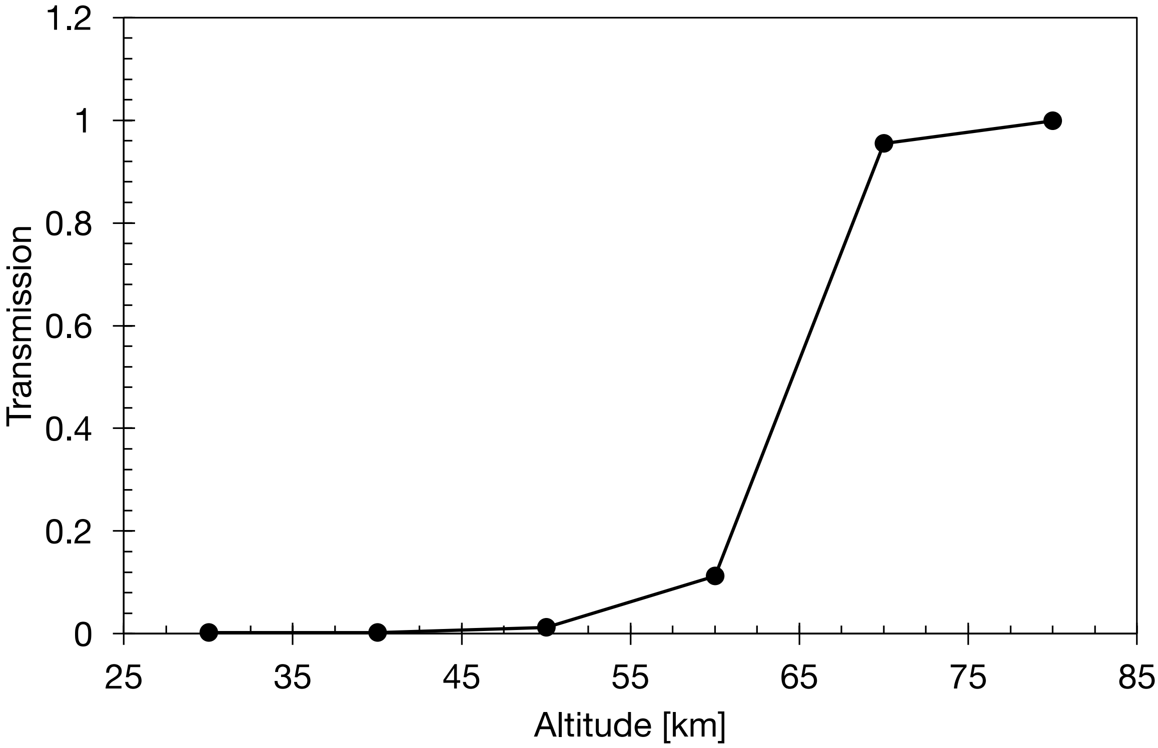

Figure 3.16: Relationship between the estimated transmittance and the altitude of the light source, assuming lightning for Venus inferred from the simulation results.

The transmission rate was defined by multiplying the peak value of the normalized photon flux reaching the observer, obtained from model simulations, by the square of the observer's altitude. It represents the ratio of the number of photons reaching the observer to the number of photons emitted by the light source.

3.2 Jupiter

3.2.1 Observation results of Jupiter

Observations of Jupiter were conducted every few months in 2020, 2021, and 2022. Before utilizing two PCHs as in the current PLD, Jupiter was observed with one PCH in 2020, and with the current PLD design for the latter half of 2021 and all of 2022. The 2022 observation results used in this analysis are shown in Table 3.3. During this period, Jupiter's apparent diameter was approximately 49 arcseconds. The average seeing was around 4 arcseconds. A 2×11 arcsecond slit mask was used for the field of view. The lightning observation wavelength was set to 656 nm (H-alpha) based on previous studies. Exposures were taken at 2 ms.

Table 3.3: Summary of PLD observation results for Jupiter

Date	Time [min]	Filter [nm]	Weather	Airmass
2021-08-20	31	656, 700	Slightly cloud	2.0
2021-09-02	48	656, 700	Clear	2.2
2021-09-06	60	656, 700	Clear	1.9
2021-09-10	4	656, 700	Clear	2.0
2021-09-13	44	656, 700	Fine	2.0
2021-09-14	70	656, 700	Cloudy	1.9
2021-09-25	35	656, 700	Clear	2.0
2021-09-27	40	656, 700	Slightly cloud	2.0
2021-10-06	50	656, 700	Slightly cloud	2.1
2021-10-12	30	656, 700	Clear	2.5
2021-10-18	30	656, 700	Slightly cloud	2.5
2022-07-30	7	656, 700	Clear	1.4
2022-08-11	10	656, 700	Clear	1.4
2022-08-14	16	656, 700	Clear	1.7
2022-08-17	60	656, 700	Clear	1.7
2022-08-21	32	656, 700	Clear	1.7
2022-08-24	10	656, 700	Clear	2.5
2022-09-07	3	656, 700	Clear	1.5
2022-09-09	63	656, 700	Clear	1.4
2022-09-10	32	656, 700	Clear	1.4
2022-09-11	20	656, 700	Fine	1.4
2022-09-14	25	656, 700	Clear	1.6
2022-09-21	62	656, 700	Clear	1.4
2022-09-26	35	656, 700	Clear	1.3
2022-09-27	21	656, 700	Slightly cloud	1.5
2022-09-28	40	656, 700	Clear	1.4

Jupiter observations were conducted at night, so the primary component of the observed light curve is the brightness from Jupiter's day face. Compared to 2021, observations in 2022 were conducted during relatively favorable time slots with higher elevations, taking into account coordination with other observations. A total of 472 minutes of observation were conducted in 2021, and 436 minutes in 2022. Although a test observation using one PCH was also conducted in 2020, it was excluded from analysis here because the signal could not be separated from background fluctuations.

After applying bandpass filtering with a time window of 5 to 200 msec to the Jupiter observation data, we examine the cumulative distribution results for the peak values of events exhibiting a threshold of 4 sigma or greater.

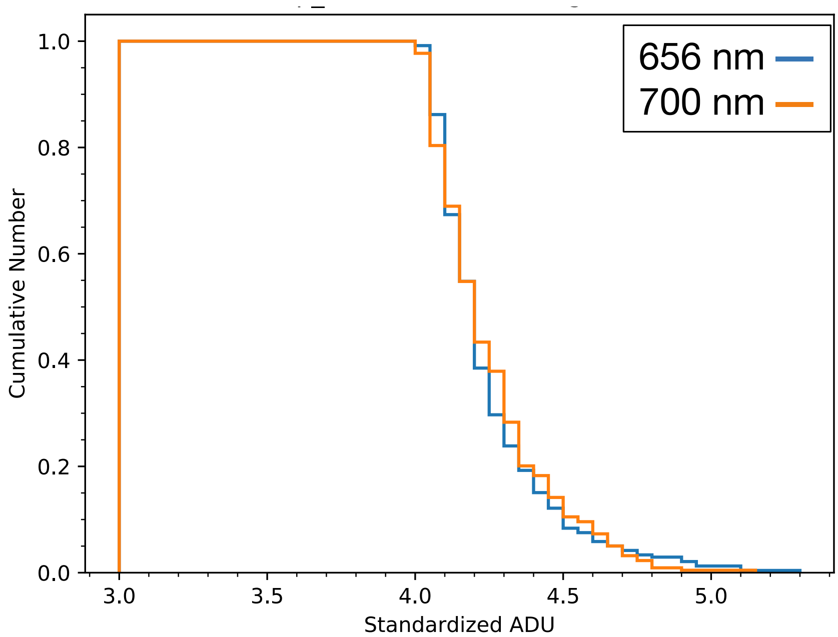

Figure 3.17: Cumulative distribution of Jupiter observed results on a 5-msec scale.

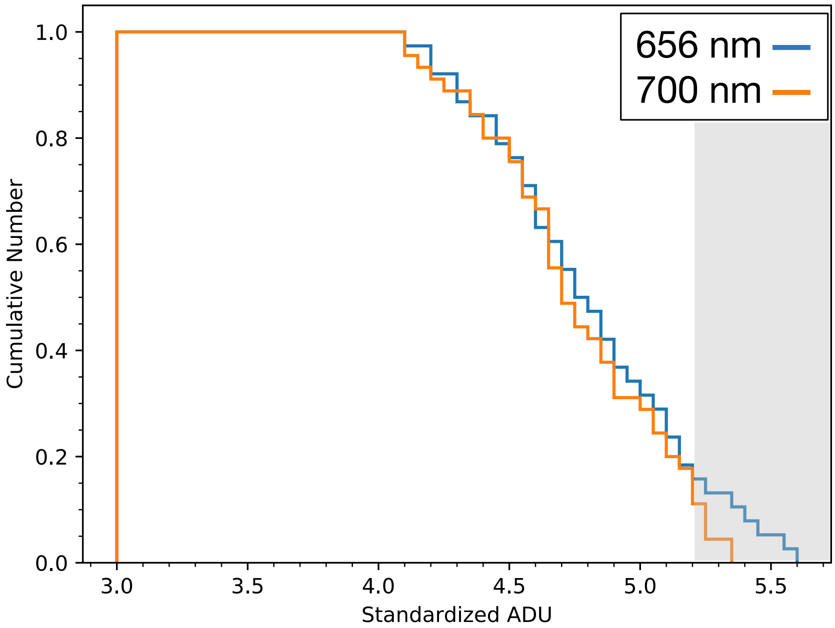

Figure 3.18: Cumulative distribution of Jupiter observed results on a 10-msec scale. The gray-shaded area indicates outlier events.

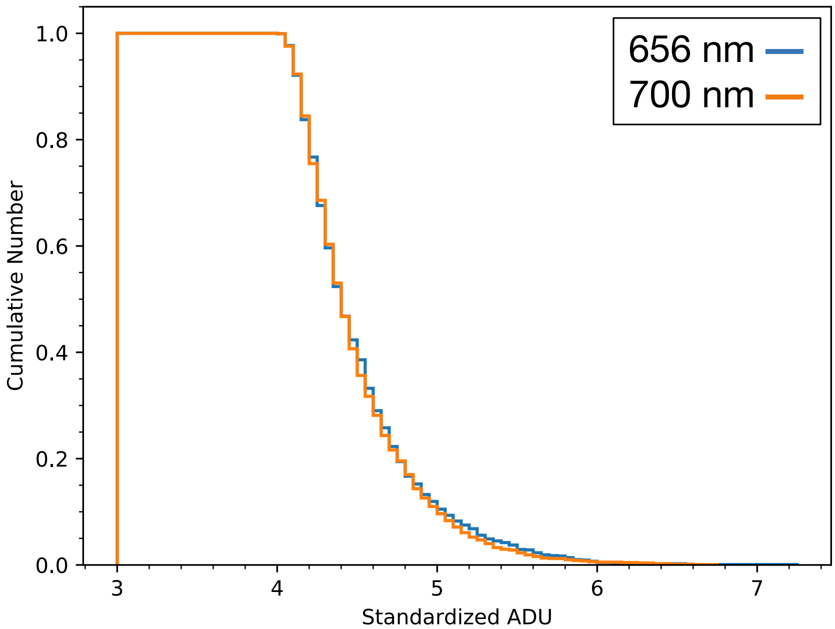

Figure 3.19: Cumulative distribution of Jupiter observed results on a 50-msec scale.

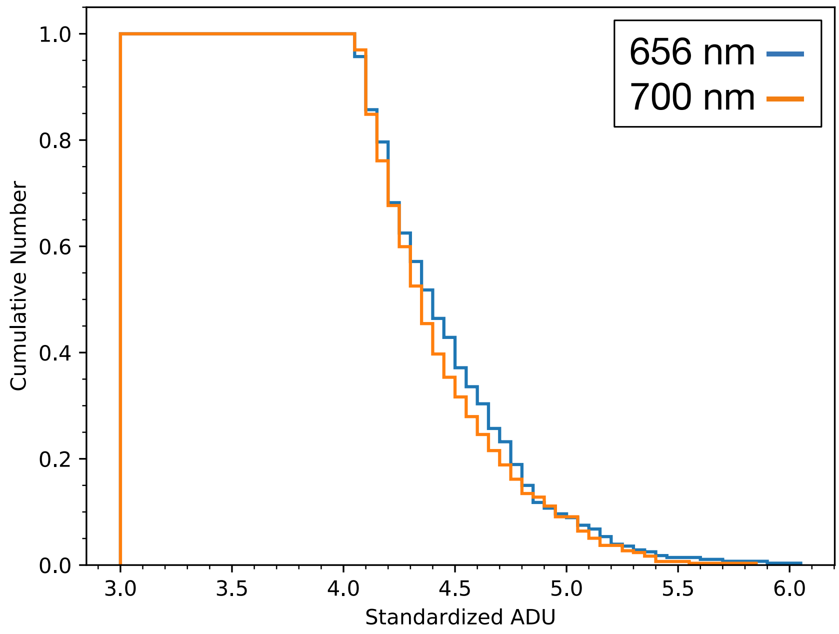

Figure 3.20: Cumulative distribution of Jupiter observed results on a 100-msec scale.

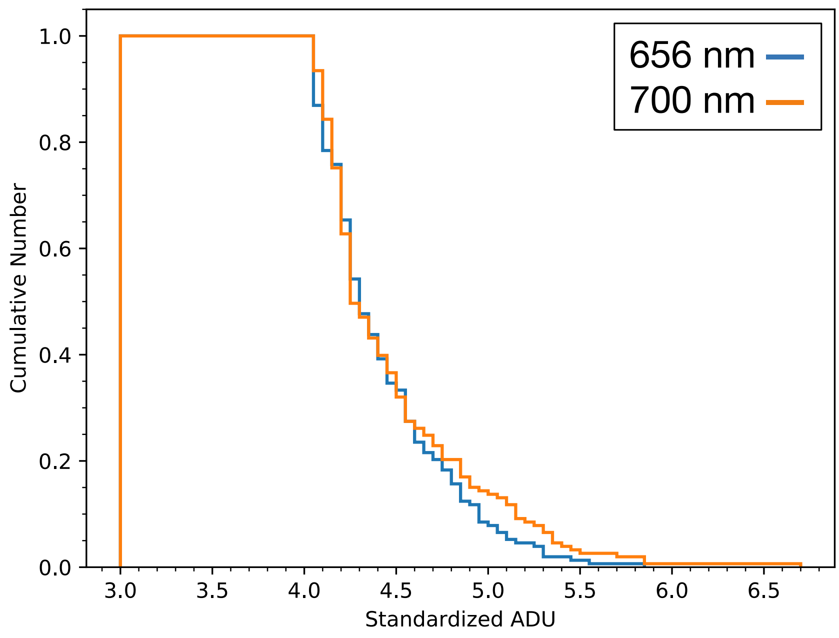

Figure 3.21: Cumulative distribution of Jupiter observed results on a 200-msec scale.

The KS test results for the cumulative distribution comparisons shown in the Figure 3.17, 3.18, 3.19, 3.20, 3.21 yielded p-values of 0.15 or greater in all cases. That is, no events statistically significant enough to be identified as outliers could be detected at any timescale. On the other hand, for the distribution shown in Figure 3.18 with a threshold set to 5.2 times the standard deviation, the p-value obtained from the KS test was approximately 0.15. To examine whether cases that could be considered valid lightning waveforms were detected under these relaxed conditions, waveform verification was performed. Figure 3.22 and 3.23, show triggered waveforms on a 10 msec scale results.

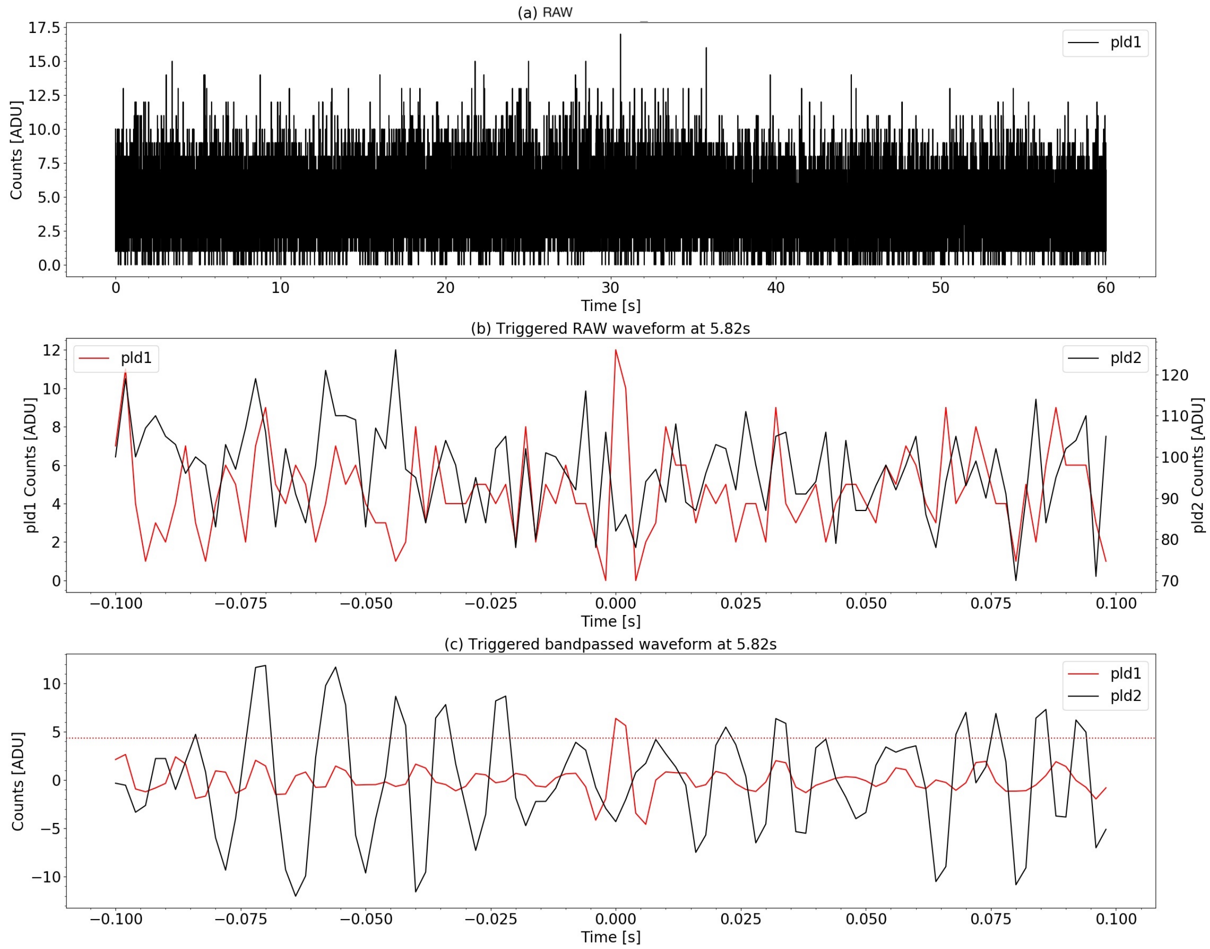

Figure 3.22: Recorded raw waveform data, an enlarged view of the selected interval, and the processed waveform after data reduction in Jupiter observation results on 2021-09-02 23:26:29 JST. (Top) The black solid line indicates the light curve at 656 nm. (Middle and bottom) The black solid line indicates the light curve at 700 nm. The red solid line indicates the light curve at 656 nm for Jovian lightning.

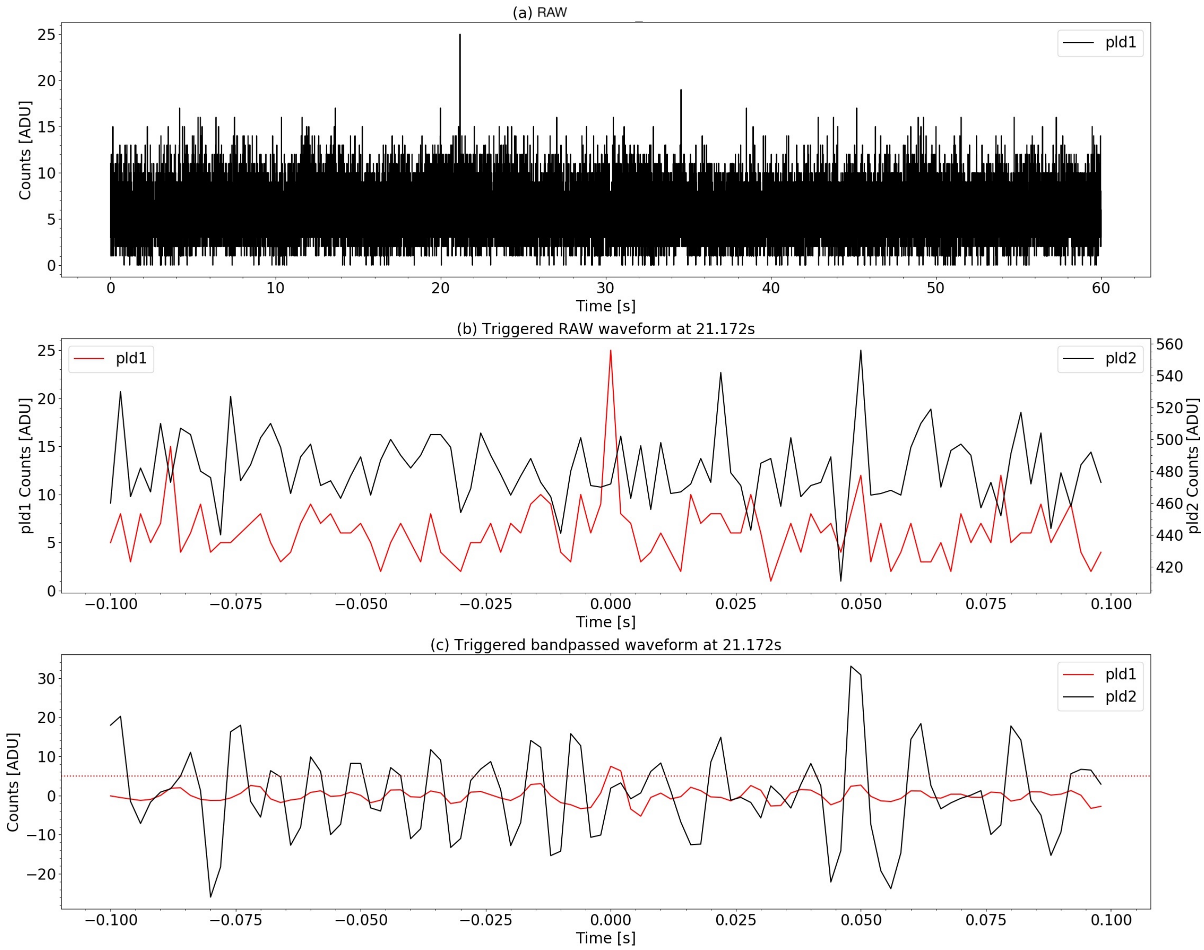

Figure 3.23: Recorded raw waveform data, an enlarged view of the selected interval, and the processed waveform after data reduction in Jupiter observation results on 2021-10-12 22:37:14 JST. (Top) The black solid line indicates the light curve at 656 nm. (Middle and bottom) The black solid line indicates the light curve at 700 nm. The red solid line indicates the light curve at 656 nm for Jovian lightning.

It can be seen that the signal waveform was triggered when it exceeded the trigger level across multiple data points. Since the threshold was exceeded over two gate times, this paper treated it as a subject for consideration. However, it should be noted that no significant difference from noise was observed in the cumulative distribution comparison. Unfortunately, the waveform and its amplitude do not allow us to conclude that lightning triggered the event.

The estimated emission intensity, along with the FWHM, for the waveform triggered by the Jupiter observation results is shown in Table 3.4.

Table 3.4: Summary of triggered waveforms of Jupiter

Date (JST)	Energy [J]	FWHM [ms]	sub-longitude	Distance [km]
2021/09/25 21:30:42	5.03×10^9	3.7	253.2	6.28×10^8
2021/10/12 22:37:14	5.71×10^9	3.7	332.4	6.58×10^8
2021/10/18 21:42:19	6.98×10^9	3.4	112.0	6.70×10^8
2021/09/02 23:26:29	4.12×10^9	3.4	99.4	6.04×10^8
2021/09/02 22:39:58	6.05×10^9	3.4	71.3	6.04×10^8

The waveform triggered for Jupiter yielded five events when conditions were relaxed, with a total observation time of 908 minutes. Given the slit FOV of 2×11 arcseconds used during the observation, assuming an average distance of 5.9×10^7 km, the observed area on Jupiter's surface was approximately 570×3100 km^2. The trigger waveform frequency was thus 5.2×10^{-11} /km^2/sec. This result is approximately 37 times lower than the occurrence frequency estimated in the previous study (Little et al. (1999)). This study compared the occurrence frequency estimated in Little et al. (1999) with that of 10^9 J lightning. Becker et al. (2020) calculated the occurrence frequency, including events up to 10^7 J. The flash rate was about 6.1×10^{-2} flashes per square kilometer per year. It was 15 times larger than 10^9 J lightning frequency.

3.2.2 Simulation results of Jupiter

The light curves and two-dimensional images obtained from the Jupiter model simulation results are shown. Note that when atmospheric pressure of 1 bar is set at an altitude of 0 km, an altitude of -80 km is defined as a height of 0 km within the model. An altitude of 111 km corresponds to an atmospheric pressure of approximately 0.25 bar, an altitude of 80 km corresponds to 1 bar, and an altitude of 59 km corresponds to 2 bar. Figure 3.24, 3.25, and 3.26 show results obtained using MieCloudScat.jl to calculate the asymmetry parameter of the phase function are shown when using the One-Term Henyey-Greenstein function.

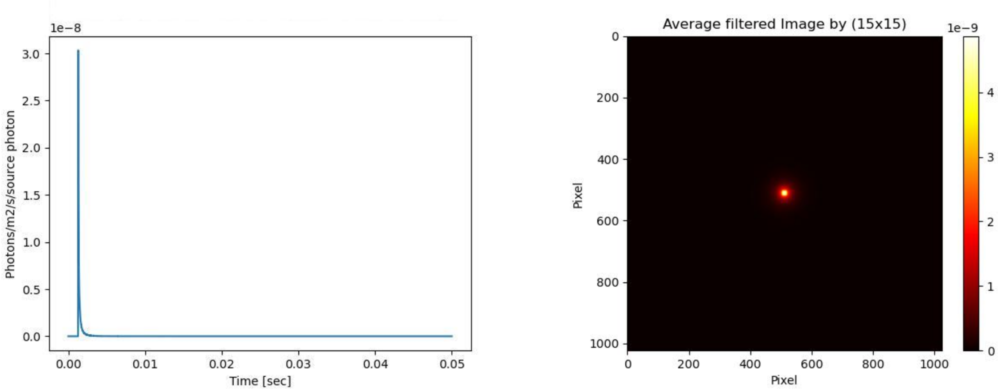

(a) Simulated light curve (b) Simulated image

Figure 3.24: Simulation results showing the light curve and image of Jovian lightning at an altitude of $z = 111$ km and a pressure of 0.25 bar with OTHG in a cumulonimbus cloud. (a) Simulated light curve. (b) Simulated image. The image was processed using an averaging filter. The cloud structure was based on R10S3 Active (Sugiyama et al. (2014)).

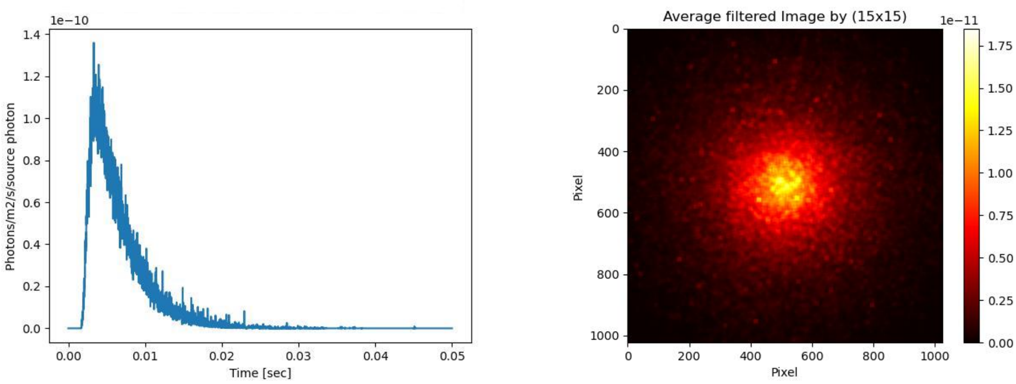

(a) Simulated light curve (b) Simulated image

Figure 3.25: Simulation results showing the light curve and image of Jovian lightning at an altitude of $z = 80$ km and a pressure of 1.0 bar with OTHG in a cumulonimbus cloud. (a) Simulated light curve. (b) Simulated image. The image was processed using an averaging filter. The cloud structure was based on R10S3 Active (Sugiyama et al. (2014)).

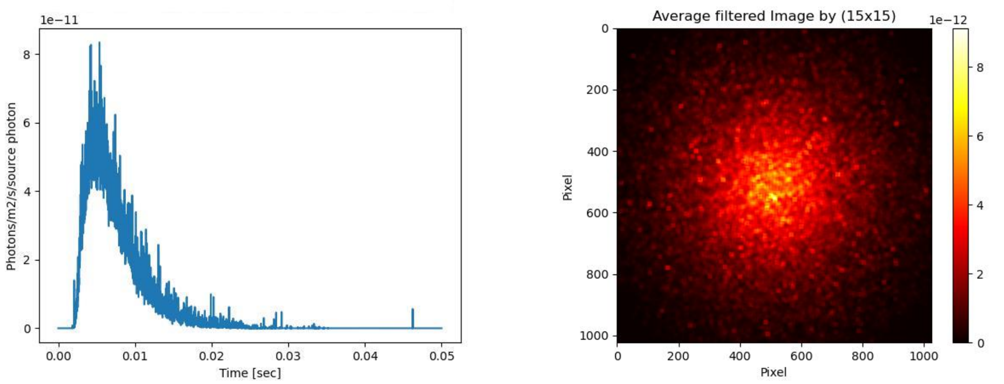

(a) Simulated light curve (b) Simulated image

Figure 3.26: Simulation results showing the light curve and image of Jovian lightning at an altitude of $z = 59$ km and a pressure of 2.0 bar with OTHG in a cumulonimbus cloud. (a) Simulated light curve. (b) Simulated image. The image was processed using an averaging filter. The cloud structure was based on R10S3 Active (Sugiyama et al. (2014)).

Next, the TTHG parameters estimated using images from Pioneer 10 by Tomasko et al. (1978), as employed in the prior study Dyudina et al. (2002), $g_1 = 0.8$, $g_2 = -0.75$, and $f = 0.954$. Results from a cloud model simulating the environment where cumulonimbus clouds form are shown in Figure 3.27, 3.28, and 3.29.

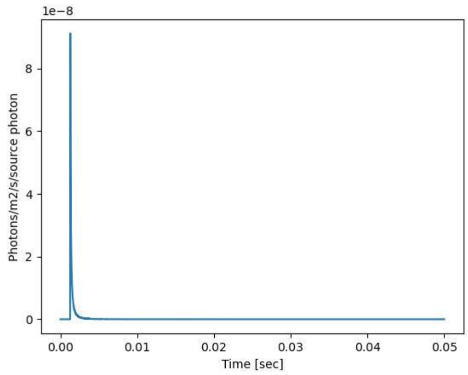

(a) Simulated light curve

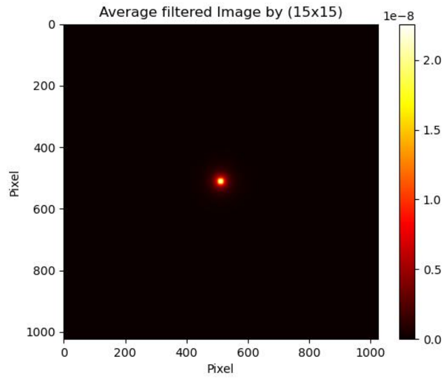

(b) Simulated image

Figure 3.27: Simulation results showing the light curve and image of Jovian lightning at an altitude of $z = 111$ km and a pressure of 0.25 bar with TTHG in a cumulonimbus cloud. (a) Simulated light curve. (b) Simulated image. The image was processed using an averaging filter. The cloud structure was based on R10S3 Active (Sugiyama et al. (2014)).

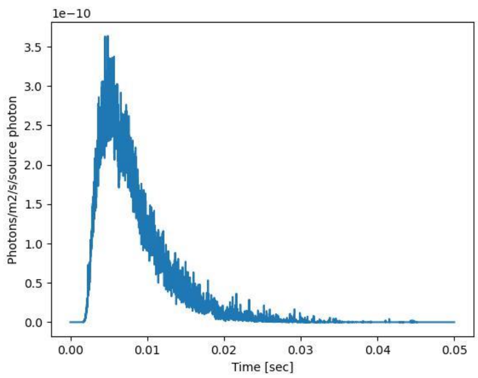

(a) Simulated light curve

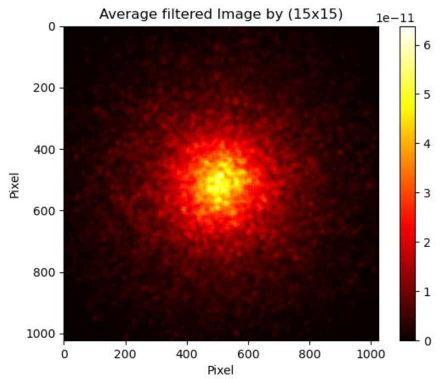

(b) Simulated image

Figure 3.28: Simulation results showing the light curve and image of Jovian lightning at an altitude of $z = 80$ km and a pressure of 1.0 bar with TTHG in a cumulonimbus cloud. (a) Simulated light curve. (b) Simulated image. The image was processed using an averaging filter. The cloud structure was based on R10S3 Active (Sugiyama et al. (2014)).

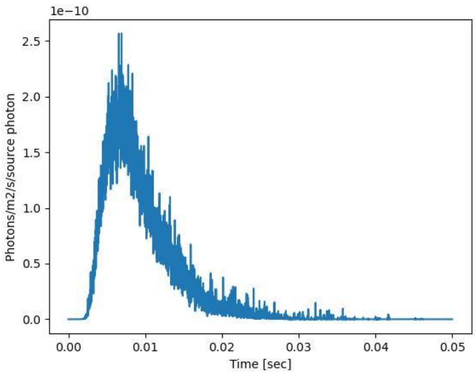

(a) Simulated light curve

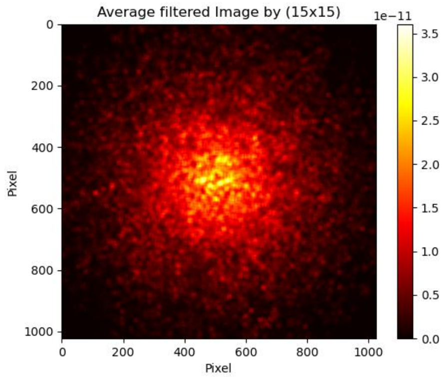

(b) Simulated image

Figure 3.29: Simulation results showing the light curve and image of Jovian lightning at an altitude of $z = 59$ km and a pressure of 2.0 bar with TTHG in a cumulonimbus cloud. (a) Simulated light curve. (b) Simulated image. The image was processed using an averaging filter. The cloud structure was based on R10S3 Active (Sugiyama et al. (2014)).

Results of the cloud model during the quiet period, assuming the vicinity of cumulonimbus clouds, are shown in 3.30, 3.31, and 3.32.

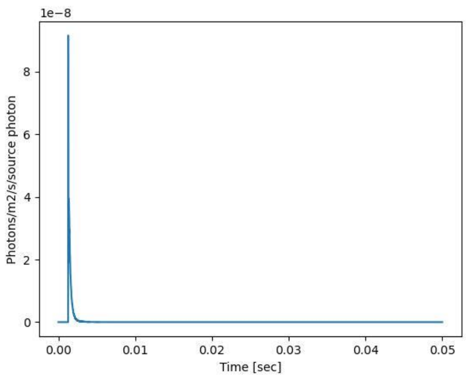

(a) Simulated light curve

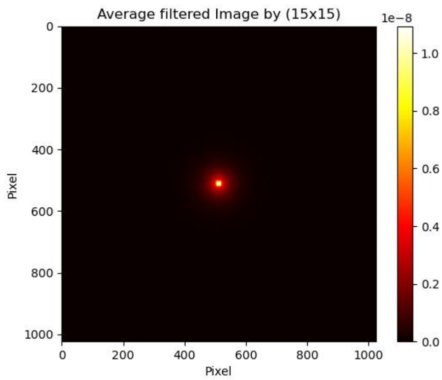

(b) Simulated image

Figure 3.30: Simulation results assuming a quiet cloud, showing the light curve and image of Jovian lightning at $z = 111$ km and 0.25 bar with TTHG during a quiet period. (a) Simulated light curve. (b) Simulated image. The image was processed using an averaging filter. The cloud structure was based on R10S3 Quiet (Sugiyama et al. (2014)).

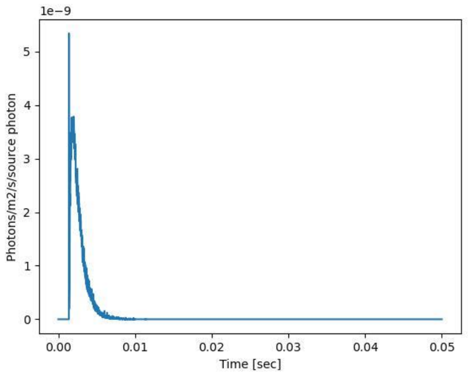

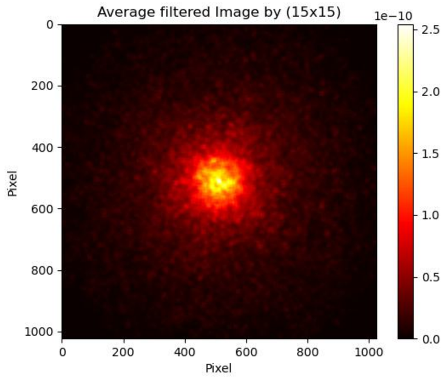

(a) Simulated light curve (b) Simulated images

Figure 3.31: Simulation results assuming a quiet cloud, showing the light curve and image of Jovian lightning at $z = 80$ km and 1.0 bar with TTHG during a quiet period. (a) Simulated light curve. (b) Simulated image. The image was processed using an averaging filter. The cloud structure was based on R10S3 Quiet (Sugiyama et al. (2014)).

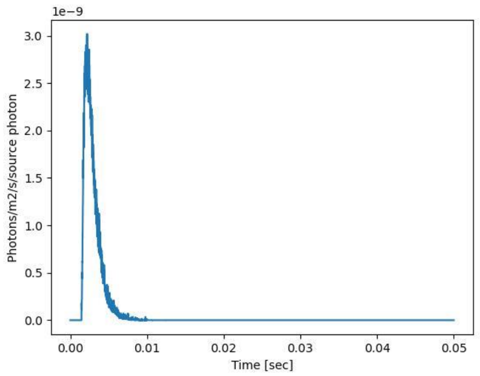

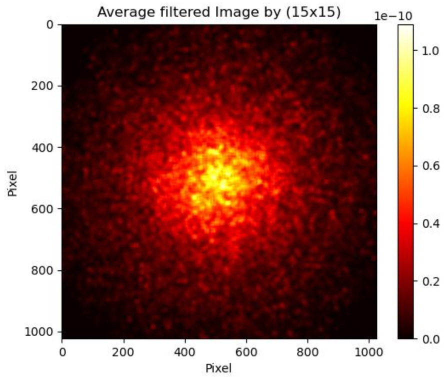

(a) Simulated light curve (b) Simulated image

Figure 3.32: Simulation results assuming a quiet cloud, showing the light curve and image of Jovian lightning at $z = 59$ km and 2.0 bar with TTHG during a quiet period. (a) Simulated light curve. (b) Simulated image. The image was processed using an averaging filter. The cloud structure was based on R10S3 Quiet (Sugiyama et al. (2014)).

Regarding the waveforms of the model using OTHG and TTHG, Figure 3.33 shows the relationship between altitude and HWHM, and Figure 3.34 shows the relationship between altitude and FWHM.

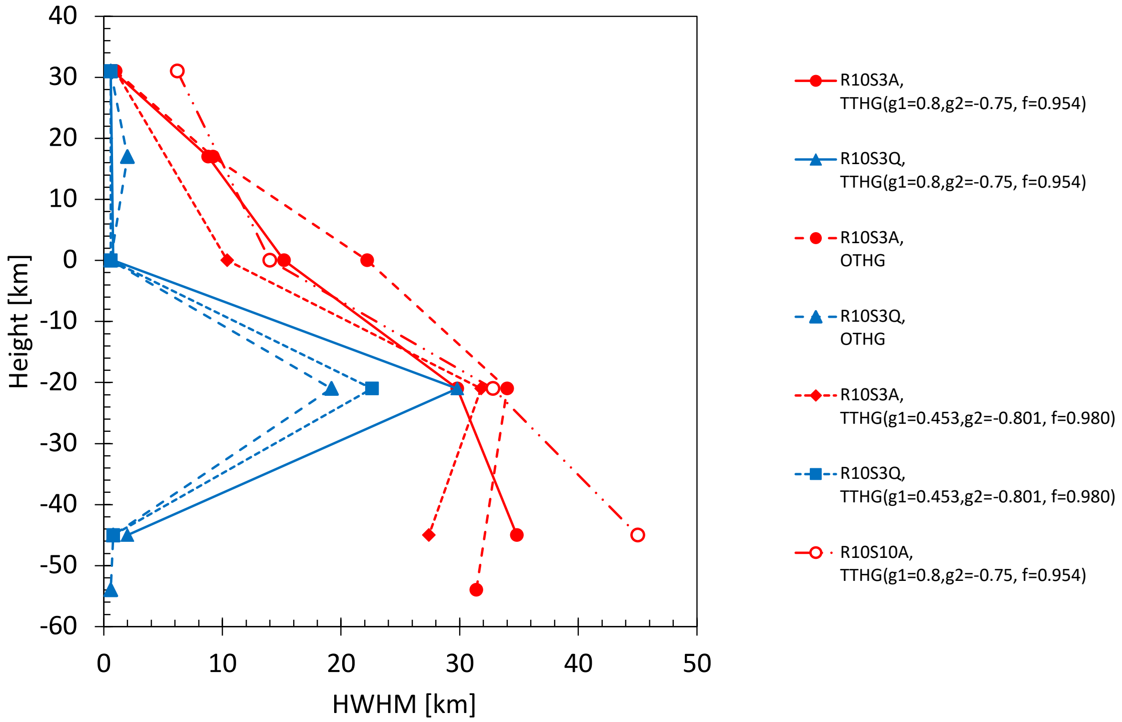

Figure 3.33: Relationship between the Half-Width at Half Maximum (HWHM) of the simulated images and altitude of the light source, assuming lightning for Jupiter. The red-colored lines (solid, broken, dashed, and dash-dot-dot) indicate cumulonimbus. The blue-colored lines indicate quiet clouds.

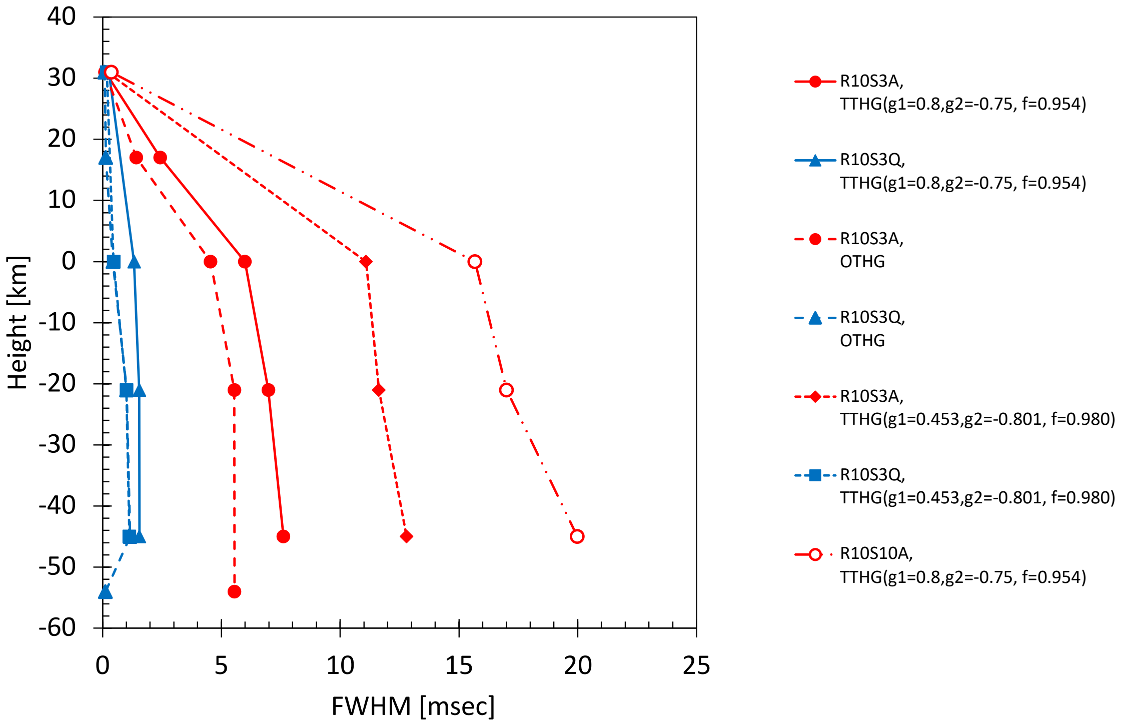

Figure 3.34: Relationship between the Full Width at Half Maximum (FWHM) of the simulated light curves and altitude of the light source, assuming lightning for Jupiter. The red-colored lines (solid, broken, dashed, and dash-dot-dot) indicate cumulonimbus. The blue-colored lines indicate quiet clouds.

Compare the results of OTHG and TTHG. Regarding HWHM, Active and Quiet showed different trends due to differences in cloud structure. In Quiet, both OTHG and TTHG show HWHM peaking at 2 bar, with HWHM decreasing at higher and lower altitudes. When the light source is positioned at low altitude, cloud absorption becomes significant.

Both FWHM values show a tendency toward saturation at altitudes below 2 bar. The FWHM timescale tends to be approximately 1.4 times longer for TTHG.

At an altitude of 126 km, where atmospheric pressure is approximately 0.1 bar, with depth d = 0 km, the relationship between depth d and HWHM is shown in the following Figure 3.35.

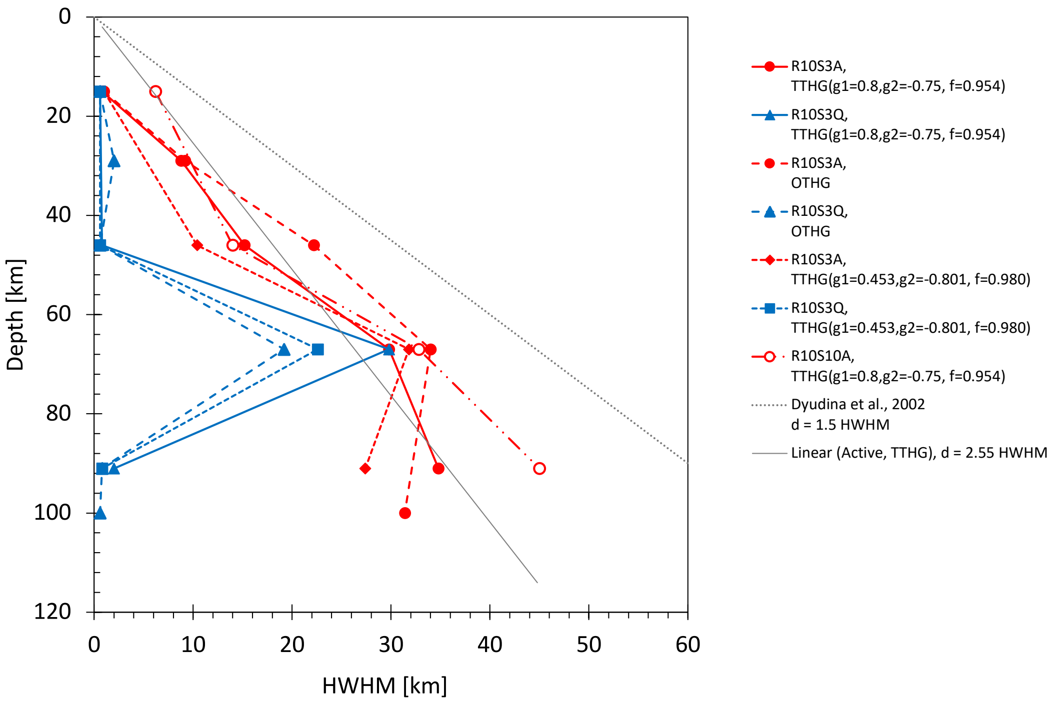

Figure 3.35: Relationship between the Half-Width at Half Maximum (HWHM) of the simulated images and depth of the light source, assuming lightning for Jupiter. The red-colored lines (solid, broken, dashed, and dash-dot-dot) indicate cumulonimbus. The blue-colored lines indicate quiet clouds. At a depth of 0 km, the pressure is 0.1 bar. The black dot lines indicate the linear relationships.

From Figure 3.35, regarding the spread of scattered light HWHM, when using the same parameters as the TTHG in the prior study, the same proportional relationship as the previous study was obtained. In Dyudina et al. (2002), the ratio of depth to HWHM was estimated to be proportional to the optical thickness between 1 and 2.5, averaging 1.5, for optical thicknesses ranging from 5 to 100. In contrast, the present model yielded a result of approximately 2.55.

3.3 Earth

3.3.1 Characteristic of FWHM observed by JEM-GLIMS

In this study, we obtained the histogram of FWHM observed by PH onboard JEM-GLIMS. The FWHM of the geostorm discharge is shown in the histogram in Figure 3.36 .

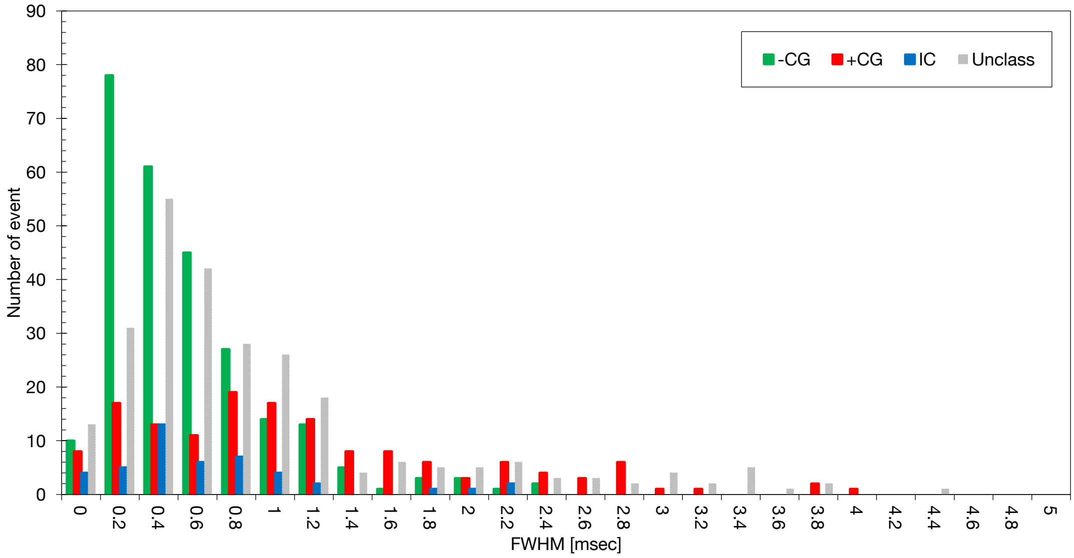

Figure 3.36: Histogram of FWHM observed by PH4 shorter than 5 msec

For all discharge types, +CG, -CG, IC, the FWHM was shorter than 5.2 msec. The average value for the discharge type that was determined was approximately 0.6 milliseconds. -CG and IC discharges frequently exhibit waveforms with FWHM values below 1 msec. In contrast, +CG discharges relatively often have longer FWHM values around 3 msec.

This study calculated the average waveform of the most common classified lightning waveform, -CG, based on classified lightning discharges. This waveform was used for comparison with the model. Figure 3.37 shows a typical negative CG average waveform. The calculations used the PH4 waveform observed in 2014.

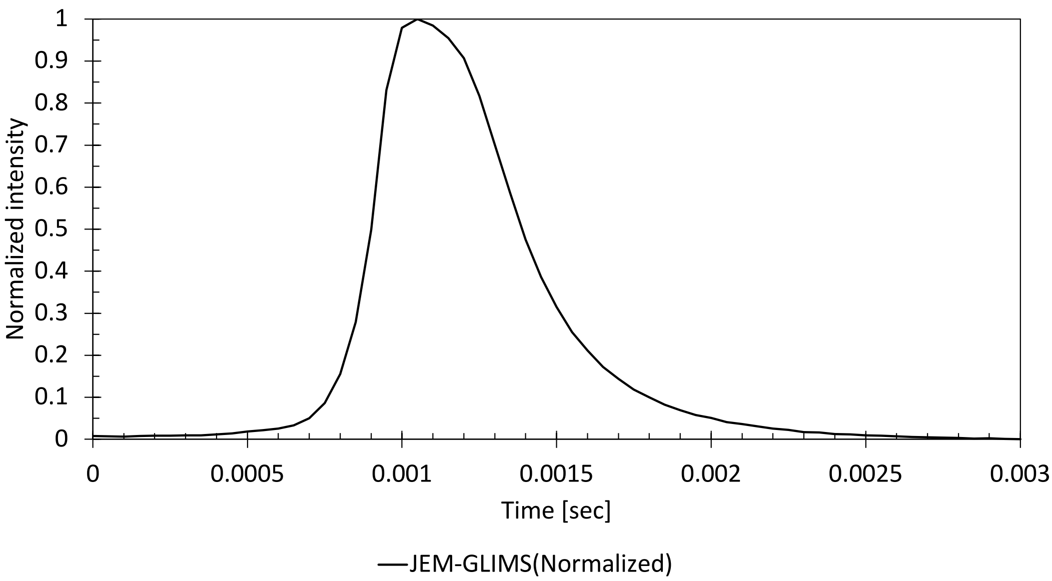

Figure 3.37: Typical negative cloud-to-ground discharge (-CG) average waveform based on the waveforms observed by PH4 in 2014.

This study clarified the relationship between the FWHM of the measured photometric curve and the peak value.

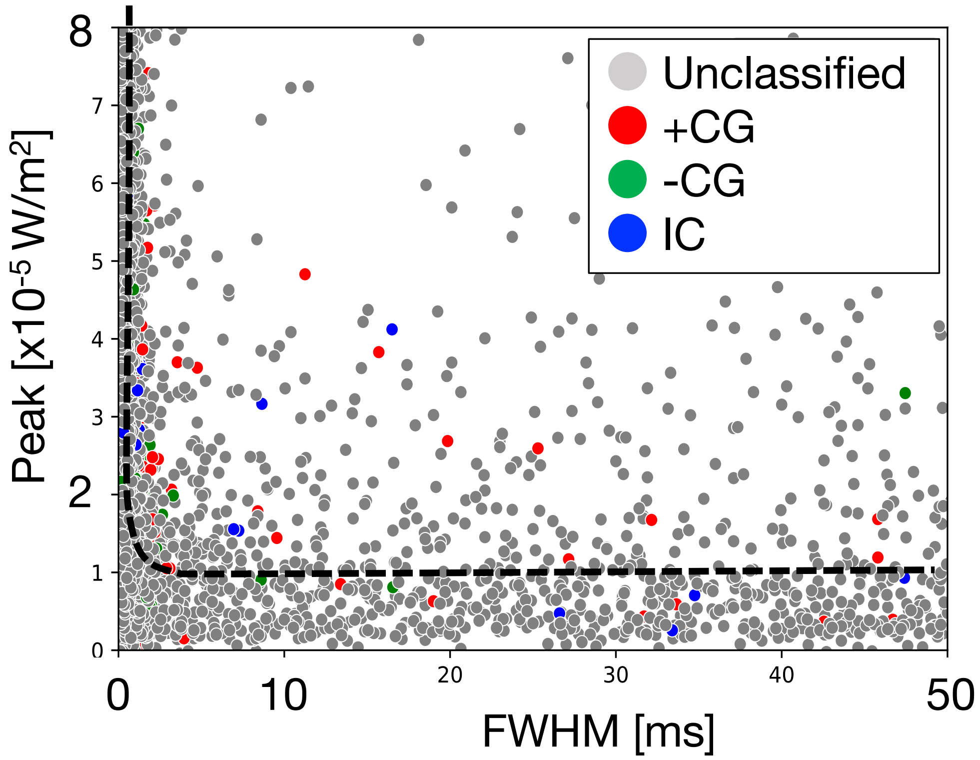

Figure 3.38: Relationship between the Full Width at Half Maximum (FWHM) of the light curves and the brightness observed by JEM-GLIMS. The red circle indicates positive cloud-to-ground discharge (+CG). The green circle indicates negative CG (-CG). The blue circle indicates intra cloud discarge (IC). The gray circle indicates unclassified results. The black dot line indicates the distribution trend.

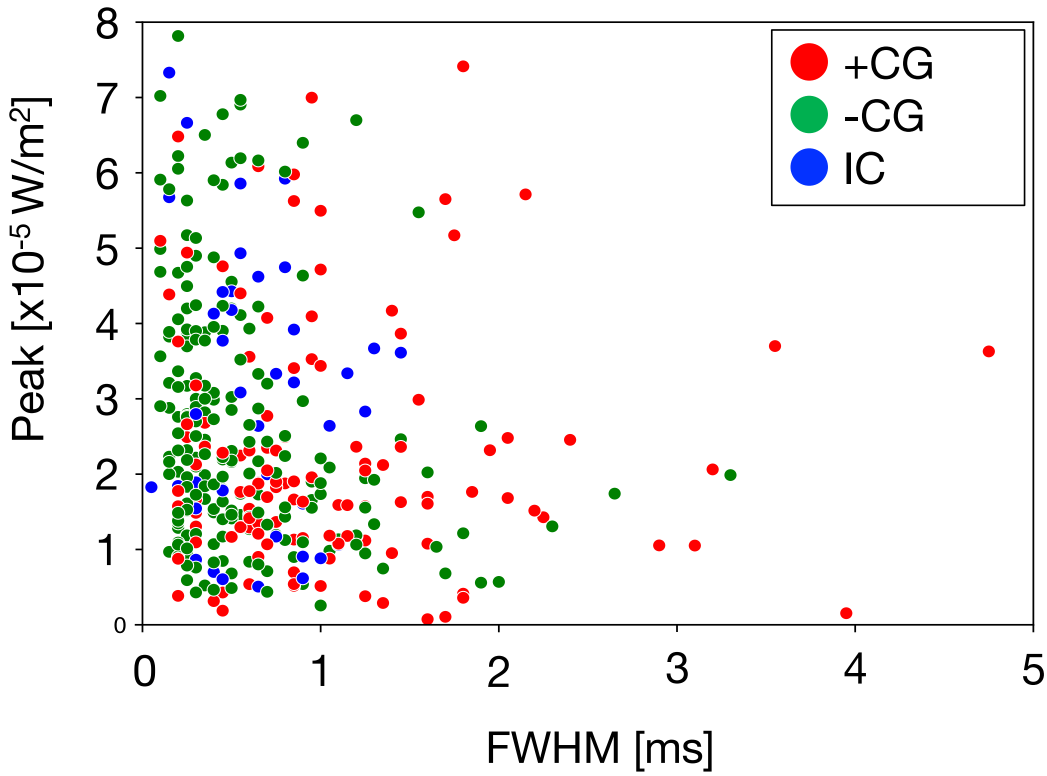

Figure 3.39: Relationship between the Full Width at Half Maximum (FWHM) of the light curves and the brightness observed by JEM-GLIMS based only on the classified. The red circle indicates positive cloud-to-ground discharge (+CG). The green circle indicates negative CG (-CG). The blue circle indicates intra cloud discarge (IC).

Figure 3.38 shows the relationship between FWHM and peak power. Figure 3.39 shows an enlarged view of the classified results. The horizontal axis represents the FWHM, in milliseconds. The vertical axis represents the Peak power. Focusing on the lightning distribution classified by discharge type, lightning with relatively small peak values was distributed more frequently. It was found that the longer the FWHM of a lightning event, the smaller its luminous peak value, indicating an inverse relationship.

3.3.2 Simulation results of Earth

Simulation results for a lightning flash scattering model occurring at various altitudes in Earth were shown. Since Earth possesses a solid surface, the surface was defined as altitude $z = 0$ km. The model assumes lightning occurs as point sources at altitudes of 2, 4, 6, 8, 10, and 12 km within Earth troposphere.

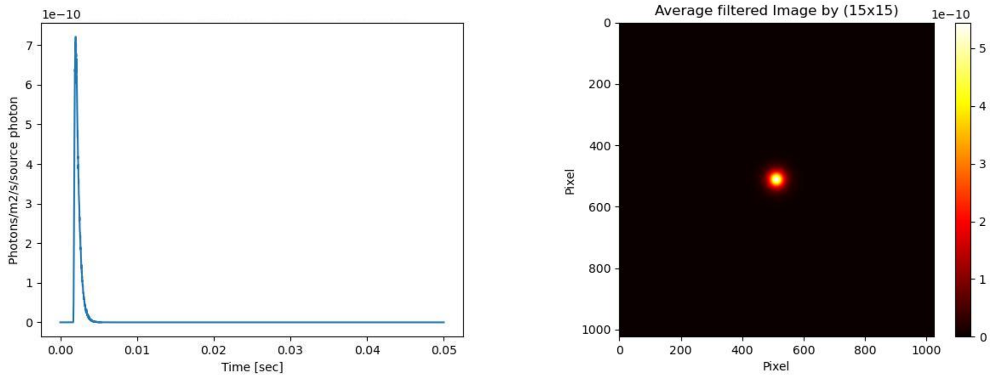

(a) Simulated light curve (b) Simulated images

Figure 3.40: Simulation results showing the light curve and image of Earth lightning at z = 2 km with TTHG. (a) Simulated light curve. (b) Simulated image. The image was processed using an averaging filter.

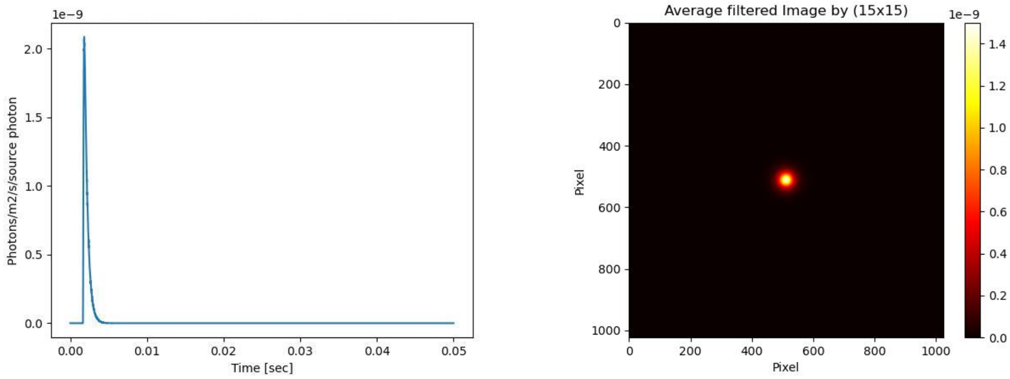

(a) Simulated light curve (b) Simulated images

Figure 3.41: Simulation results showing the light curve and image of Earth lightning at z = 4 km with TTHG. (a) Simulated light curve. (b) Simulated image. The image was processed using an averaging filter.

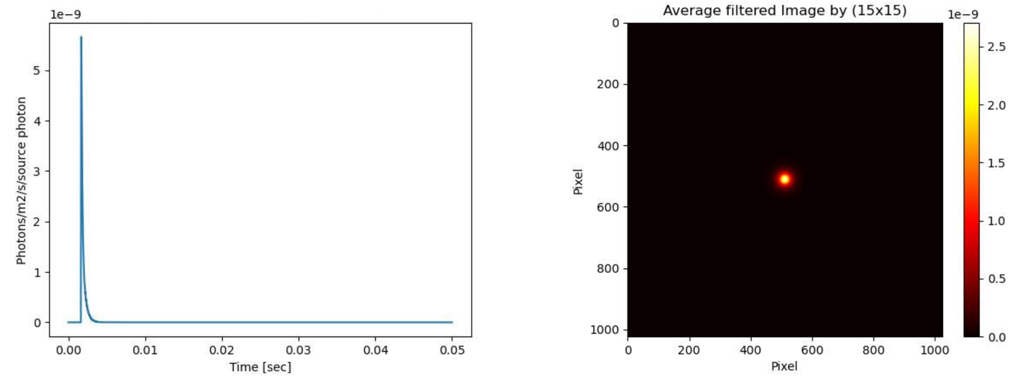

(a) Simulated light curve

(b) Simulated images

Figure 3.42: Simulation results showing the light curve and image of Earth lightning at z = 6 km with TTHG. (a) Simulated light curve. (b) Simulated image. The image was processed using an averaging filter.

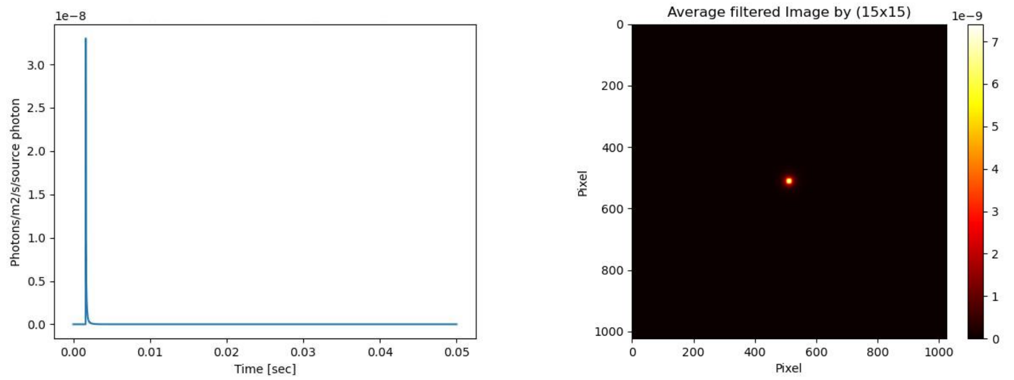

(a) Simulated light curve

(b) Simulated images

Figure 3.43: Simulation results showing the light curve and image of Earth lightning at z = 10 km with TTHG. (a) Simulated light curve. (b) Simulated image. The image was processed using an averaging filter.

In the cloud structure used in this study, the time constant of the visible lightning luminance curve originating from submillisec-scale lightning discharges was shorter than to 0.6 msec. Figure 3.44 plots the relationship between altitude and FWHM, where the lightning flash duration is defined as the FWHM of the light curve obtained from the simulation.

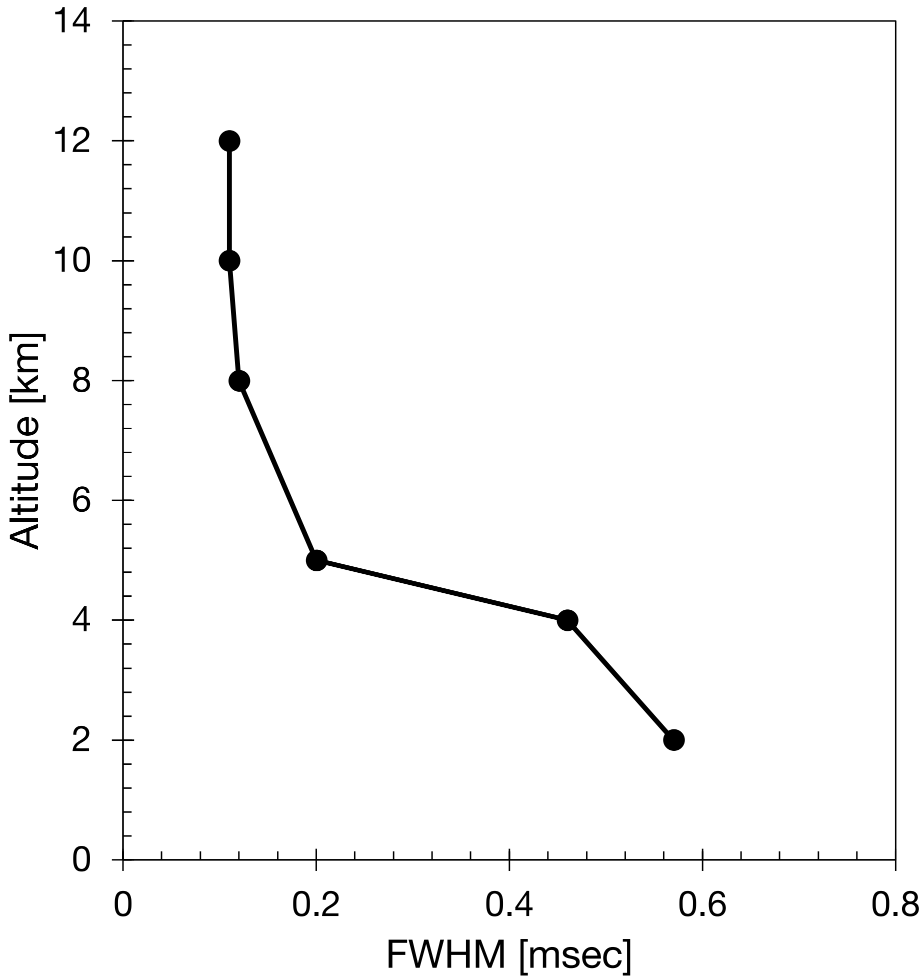

Figure 3.44: Relationship between the Full Width at Half Maximum (FWHM) of the simulated light curves and altitude of the light source, assuming lightning for Earth.

Summer thunderstorms are thought to form at altitudes between 3 and 5 kilometers. At the average value of 4 km, the FWHM was found to be 0.46 msec.

4 Discussion

In this section, we have described the evaluation of the model and the PLD observation results. After that, we have discussed lightning time constants and limitation of this study. Finally, we have described the further observation by PLD.

4.1 Evaluation of the model performances

The reliability of our 3D scattering model was established using observational data from Earth' s JEM-GLIMS. The model successfully explained and quantitatively reproduced the waveform, duration time, anti-correlation relationship, and the relationship between the lightning pulse duration and the occurrence altitude characteristics of the lightning flash.

First, we compared waveforms and evaluated the model. PH onboard JEM-GLIMS observed data was compare with our model results. 4.1 shows us the comparing results.

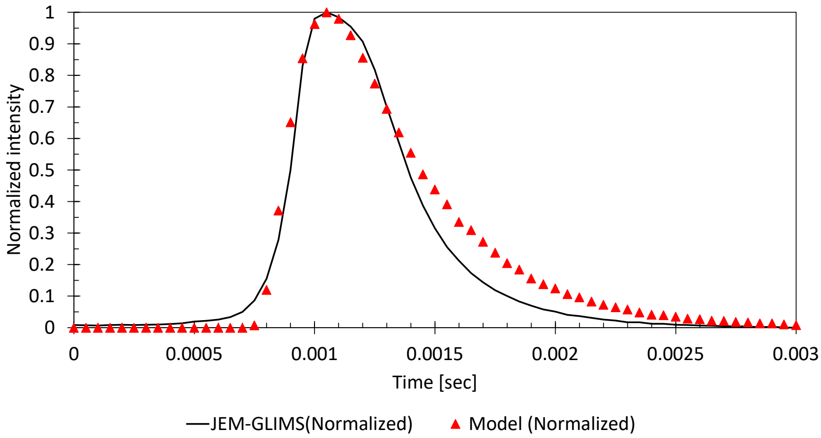

Figure 4.1: Waveform comparison between the PH-averaged waveform and our model results. The black line indicates JEM-GLIMS observed results. The red triangle indicates the simulation results. Both sets of data were normalized for a maximum of 1 and a minimum of 0.

The correlation coefficients was about 0.98. Our model represented PH averaged waveform well. Comparing the waveforms, the model waveform exhibits a short rise time. This is because the PH observation data uses an averaged waveform that includes the stepped reader waveform. The model only considers the submillisecond return stroke. This difference is thought to manifest in the rise time of the waveform. Due to variations in the return stroke discharge time and cloud structure, the waveform of lightning discharge is not always identical with the model result.

Second, we compare the model estimated time constant with the average time constant of the observed waveform. Summer CG lightning discharges are thought to occur between the ground and the bottom of the cloud at around 2 km. At the average altitude of 2 km, the model estimate was about 0.6 msec. This results was inconsistent with the overall average value of approximately 4.8 msec from the JEM-GLIMS data. However, these discrepancies are negligible because the model in this study considers only simple discharges lasting submilliseconds. In fact, the average of classified lightning based on was about 0.6 ms. The lightning for which type identification succeeded is considered to have been a simple lightning discharge. It would seem that the model's estimated duration is consistent with the observed results.

Third, we consider the inverse proportional relationship. This analysis of PH onboard JEM-GLIMS observational data was consistent with the results of You et al. (2019) using data observed by TRMM/LIS. This suggested that the anti-correlation relationship between FWHM and brightness is common. This relationship confirms that the physical principle governing multiple scattering and pulse broadening is accurately represented. Specifically, this anti-correlation is rooted in the consistency demonstrated between the FWHM of the pulse and the model's calculated cloud transmittance.

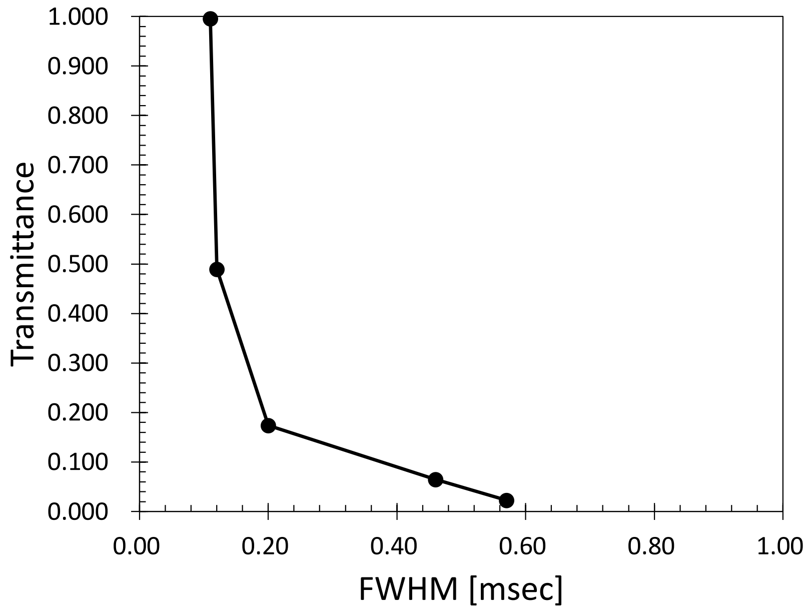

Figure 4.2: Relationship between the FWHM and transmittance simulated by our model

This successful reproduction establishes the model's reliability while supporting the claim that this inverse correlation is a universal physical phenomenon governing the scattering of lightning flashes within clouds.

Finally, the relationship between FWHM and altitude derived from this study's model was consistent with the differences in emission altitude suggested by LSI. JEM-GLIMS observed a lightning event with an overall duration of approximately 200 ms. Figure 4.3 shows an example of a long-duration lightning event observed by JEM-GLIMS PH3 and PH4 on 2013/04/15.

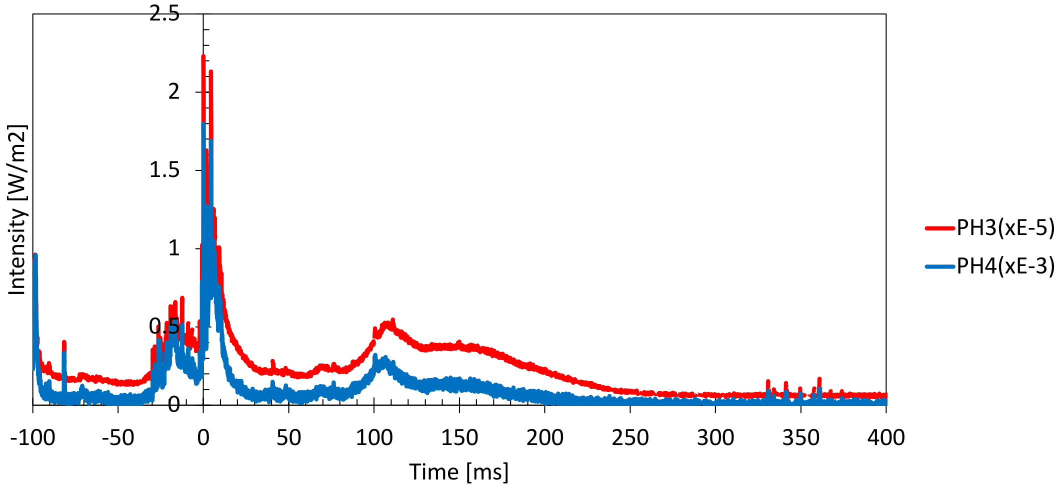

Figure 4.3: Example of a long-duration lightning event observed by JEM-GLIMS PH3 and PH4 on 2013/04/15.

Figure 4.4 shows the correspondence between the imaging timing of the LSI's four consecutive images and the PH's light curve.

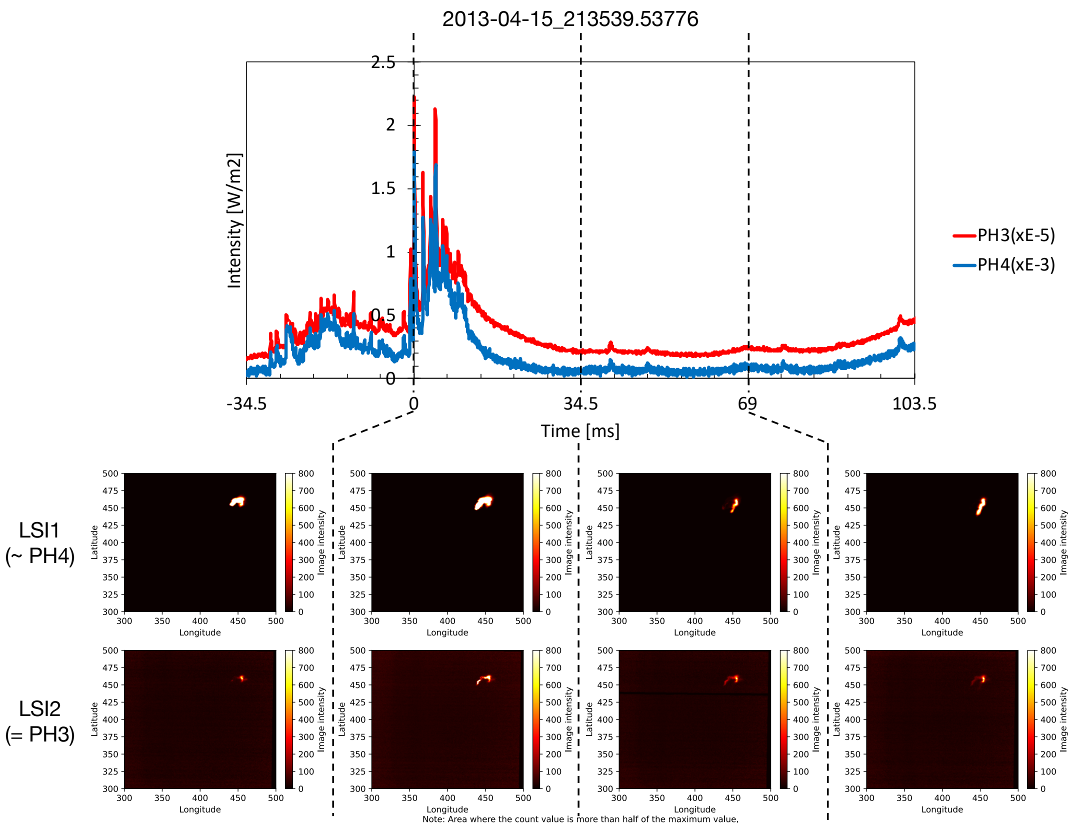

Figure 4.4: The correspondence between the imaging timing of the LSI's four consecutive images and the PH's light curve

The second frame of the LSI is the trigger timing for lightning via PH. Figure 4.5 shows the waveform of Frame 2 and an enlarged view of the lightning image. The rise time of the lightning-typical waveform was confirmed to be short based on the PH light curve during Frame 2 imaging. The PH’ s FWHM of the waveform was approximately 0.35 msec.

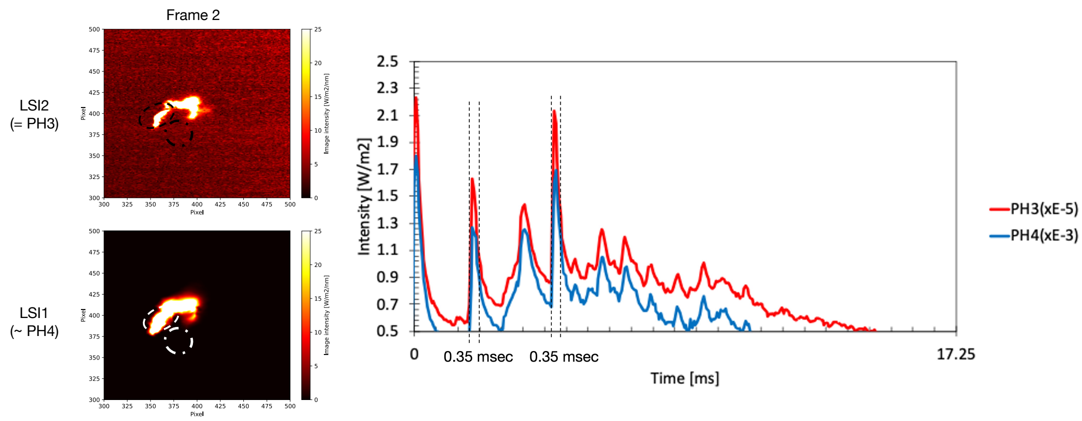

Figure 4.5: Comparison of LSI image frame-2 and PH photometric curve. The black dashed line area of LSI2 and the white dotted line area of LSI1 showed the same distribution. The difference in absorption amounts was small, and the altitude of occurrence would be high.

Figure 4.6 shows the waveform of Frame 3 and an enlarged view of the lightning image.

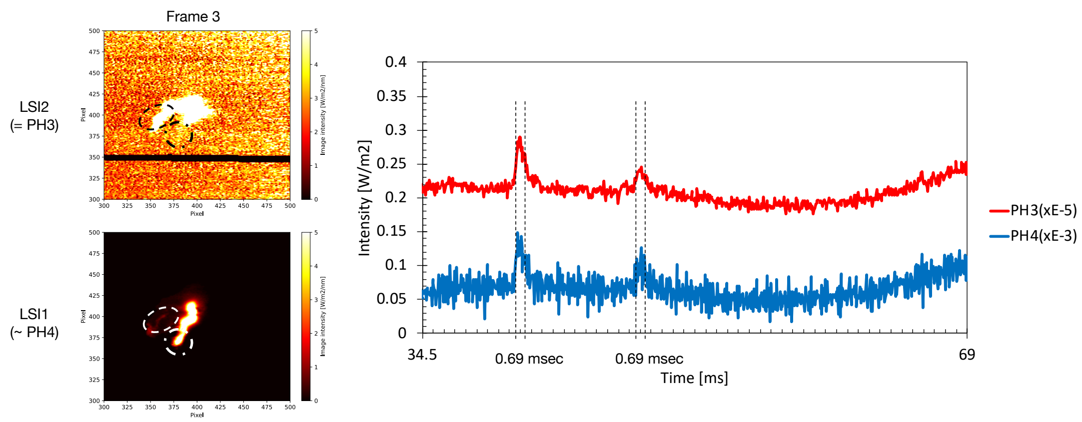

Figure 4.6: Comparison of LSI image frame-3 and PH photometric curve. The black dashed line area of LSI2 and the white dotted line area of LSI1 showed a different distribution. The difference in absorption amounts was large, and the altitude of occurrence would be low.

The PH light curve recorded during Frame 3 also confirmed the presence of a lightning-typical waveform with a short rise time. The FWHM of the waveform was approximately 0.69 msec. It can be seen that the area emitting light in both Frame 2 and Frame 3 remained illuminated for an extended period. However, comparing the images from LSI-1 and LSI-2 revealed differences in brightness distribution. LSI-2’s filter wavelength is 726 nm. Oxygen molecules absorb the 726 nm. The atmospheric transmittance is low, at around 0.2. Low-altitude lightning discharges are absorbed by oxygen molecules, causing the light intensity to decay. The fact that LSI-2 is relatively dim compared to LSI-1 is thought to indicate not only differences in the lightning discharge spectrum but also a lower altitude. This study revealed that Frame 3 exhibits differences in brightness distribution (within the dot-dashed area in Figure 4.6) between LSI-1 and LSI-2. The images also suggested the difference in occurrence altitude. The scattering model in this study has demonstrated that the difference in FWHM corresponds to a difference in altitude (Figure 3.44). This study, based on the model, suggests that the lightning in Frame 2 would have occurred at an altitude of approximately 4.5 km. The lightning in Frame 3 would have occurred at an altitude below 2 km. This model result is consistent with the elevation differences estimated from the LSI image brightness.

The model developed in this study showed a high correlation with the PH waveforms observed by JEM-GLIMS. The average time constants estimated by PH’ s data also matched. The model also expressed an inverse relationship between light intensity and the FWHM of the PH light curve. Furthermore, the relationship between FWHM and altitude indicated by the model was consistent with the comparison results between LSI and PH. Based on the results above, the model developed in this study can be used to estimate the durations of lightning-scattering waveforms on Venus and Jupiter.

4.2 Evaluation of PLD observations

The waveform that could be confidently identified as ideal Venusian or Jovian lightning has not been triggered, and there remains debate as to whether the detected waveform originates from lightning. This section compares PLD observational results with model results and previous studies to interpret the PLD observational findings.

4.2.1 Evaluation of the results of Venus

Observational results from the PLD confirmed that the physical characteristics of the FWHM, detection frequency, and emission energy were consistent with previous studies. Regarding the FWHM of the waveform, ground-based telescope observations were thought to capture light-emitting phenomena lasting approximately 50 msec or less per frame due to constraints such as CCD image readout time. In contrast, the FWHM of the waveform triggered by the PLD was 2 msec or less, demonstrating consistency in this regard. Furthermore, the FWHM simulated from this model and the FWHM of the observed waveform from the PLD were consistent. The detection frequency (7.2×10^{-12} /km^2/sec) was also of the same order of magnitude as the occurrence frequency estimated in previous studies (2.7×10^{-12} /km^2/sec), being several times higher. The maximum energy of the lightning discharge was estimated to be approximately 10^9 J. Figure 4.7 shows the cumulative histogram of the energy of the lightning discharge observed by ground-based telescopes and the LAC instrument onboard the Akatsuki, as well as the energy when events triggered by the PLD were assumed to be lightning discharges.

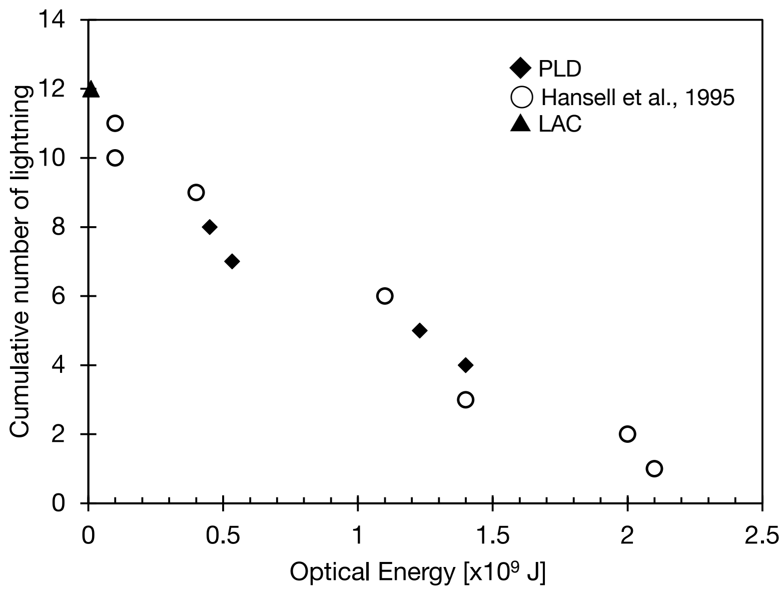

Figure 4.7: Cumulative distribution of light emission energy for comparing previous observation results with PLD detection results. The black rhombus indicates PLD results. The white circle indicates previous ground-based observation results. The black triangle indicates LAC results.

The luminescence energies observed in previous studies were distributed within the range of 10^8 to 10^9 J. Since the energies of events triggered by PLD fall within this range, it cannot be ruled out that lightning was not triggered.

While consistency has been confirmed for the physical parameters, other light sources and signal sources must be considered. The shot noise from the photomultiplier tubes mounted on the PCH is excluded by comparing the peak distributions of triggered waveforms, but other noise sources besides shot noise may not be eliminated. One possible noise source is Cherenkov radiation generated by cosmic rays and environmental gamma rays. The primary cosmic ray source contributing to photomultiplier tube noise is believed to be muons. When a muon passes through the glass material of the sensor window, it emits numerous photons via Cherenkov radiation. The number of photons N generated in Cherenkov radiation is derived from the decay of charged particles in the medium. The number of photons emitted per unit length when a charged particle with charge z passes through a medium can be calculated using the Frank-Tamm Formula as follows, assuming the wavelength range is from λ_1 to λ_2, the fine structure constant $\alpha = \frac{1}{137}$, and the Cherenkov light emission angle is θ_c.

$$\frac{dN}{dx} = 2\pi z^2 \alpha \sin^2\theta_c \left(\frac{1}{\lambda_1} - \frac{1}{\lambda_2}\right) \tag{33}$$

The wavelength range of the PCH using the wavelength region adopted by the PLD, from 230 to 870 nm, and using muons with $z = 1$, yields 1.15×10^5 photons/m. Assuming the thickness of the PCH's photoelectric surface and glass surface is 0.5 mm, and assuming the emission angle where the number of emitted photons is maximized ($\sin^2\theta_c = 1$), the number of photons generated by Cherenkov radiation is approximately 57. Assume these photons are detected as photons with a wavelength of 777 nm. Since the energy per 777 nm photon is 2.55×10^{-19} J, the event was expected to be observed as having an energy of 1.45×10^{-17} J. In contrast, for the spike waveform triggered during Venus observation, the energy on the PCH can be determined from the PCH's sensitivity and count number. Using the average value of the triggered waveform, 153 ADU, the energy was equivalent to an event of 3.20×10^{-15} J occurring at the PCH light-receiving surface. Comparing the energy that could be produced by Cherenkov radiation with the energy estimated from the triggered spike waveform, the event was 218 times brighter than the energy from Cherenkov radiation. Therefore, it is unlikely to be noise caused by cosmic ray muons.

Other potential noise sources include thermionic emission and increased dark current. Specifically, decreased vacuum in the PCH, degradation of the dynode surface, and thermionic emission from the photocathode or dynode could be primary causes of noise. These may manifest as spike-like noise. However, it is unlikely that component degradation has progressed significantly even in an instrument that has been in operation for approximately one year. Furthermore, no events exhibiting amplitudes equivalent to the triggered spike waveforms were confirmed in either the dark current measurements conducted beforehand at room temperature or in the dark current measurements taken before and after the observation on the same day. Additionally, the possibility of fluctuations in the instrument's power supply voltage must be considered. Since the photomultiplier tube operates under high voltage, even slight voltage fluctuations can cause significant amplification, potentially leading to increased noise. While power to the PCH itself is supplied via the control unit, this unit shares its power supply with the control PC and camera. Therefore, it cannot be ruled out that noise generated due to power instability in other devices coincided with the trigger timing and was recorded as large spike-like noise.

Another possible cause is a meteorite impact. Blaske et al. (2023) suggested that meteorites can emit light bright enough at Venus's lightning wavelength of 777 nm. 4.8 shows the spectrum of the meteorite and the spectrum of blackbody radiation as demonstrated in previous studies.

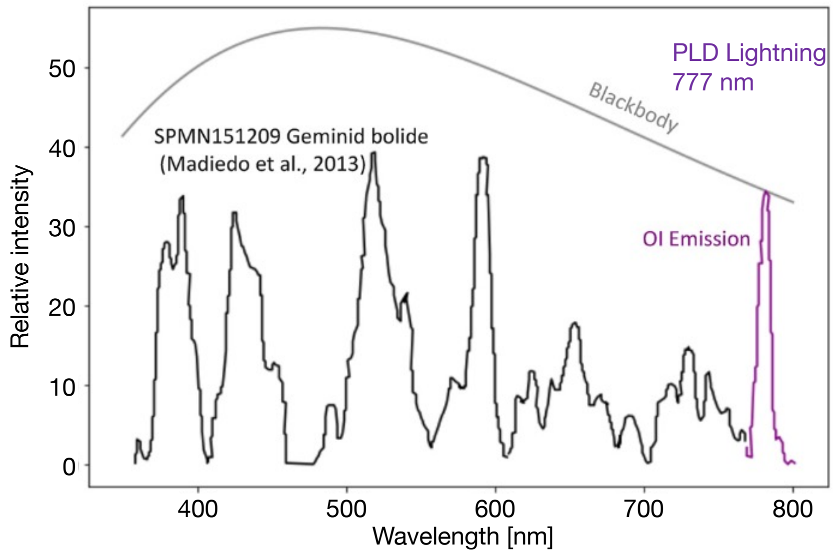

Figure 4.8: Spectrum of meteorite and blackbody compared with the wavelength of PLD. The purple line indicates the OI emission same as Venusian lightning wavelength (777 nm).

However, PLD dual-band observation observed no simultaneous peaks at 777 nm and 700 nm. The radiance of a blackbody at 700 nm is approximately 1.2 times that at 777 nm. The observed brightness of the Geminid meteor shower at 700 nm is approximately one-seventh that at 777 nm. Due to PLD's ten times wider bandwidth, the PLD sensitivities at both wavelengths are nearly equal. The PLD dual-band observation indicated that the triggered events were not meteor events.

Events triggered by the PLD with durations of 2 msec or less showed a time scale comparable to the FWHM predicted by the model. If lightning discharges occur on a submillisecond scale, the visible light waveform is likely to show durations of 2 msec or less. Of the electrostatic energy accumulated by charge separation that generates lightning discharges, 10^{-3} to 10^{-4} is used for visible light emission (Maggio et al. (2009), C. T. Russell (1991)). Combined with the transmission rate of scattered light obtained from model calculations, the required total electromagnetic energy can be estimated. The luminous energy of lightning discharges observed in previous studies, ranging from 1.1×10^7 to 2.0×10^9 J were examined. -CG assumed an altitude near the cloud base of approximately 45 km. +CG assumed lightning originating near the cloud top at an altitude of approximately 70 km, while IC assumed lightning originating from an altitude of approximately 55 km, the average value between 45 and 65 km. As a result, the total electromagnetic energy required was estimated to be between 1.3×10^{10} and 1.0×10^{15} J (Tabel 4.1). Figure 4.9 shows total electromagnetic energy to observe the 1.1×10^7 J optical lightning as function of altitude and ratio of electromagnetic to optical energy.

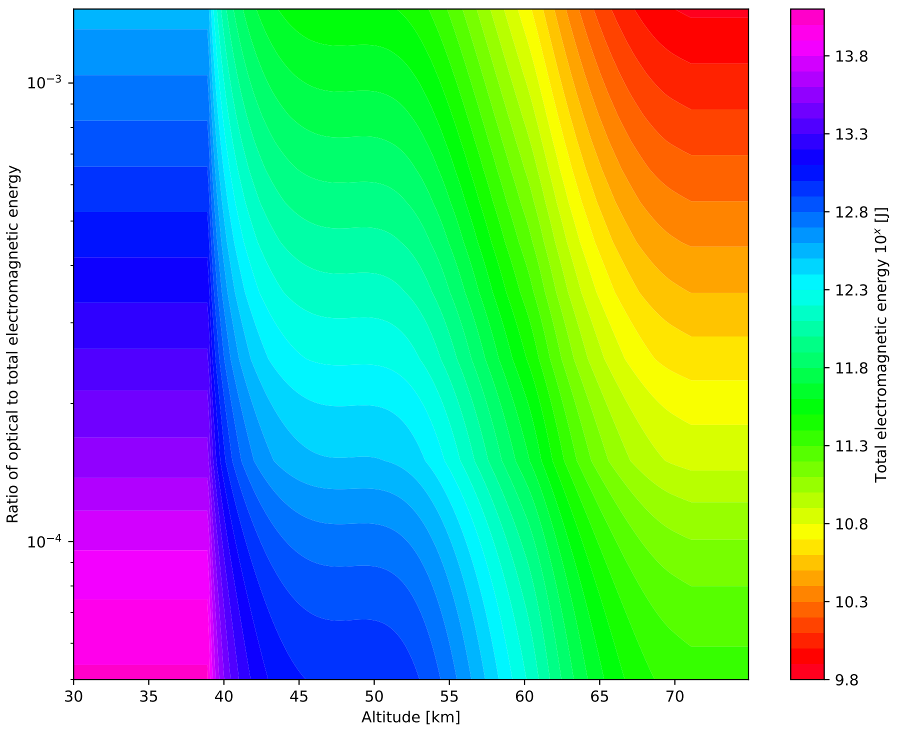

Figure 4.9: Heatmap showing the distribution of optical energy 1.1×10^7 J relative to electromagnetic energy at each altitude. The vertical axis indicates the ratio of optical to total electromagnetic energy. The horizontal axis indicates the occurrence altitude of lightning. The color scale indicates an exponential scale in base 10 of the total electromagnetic energy.

Table 4.1: Altitude dependence of observable optical energy and total electromagnetic energy.

	Total electromagnetic energy [J]		
Optical observed energy [J]	at 45 km (-CG)	at 70 km (+CG)	at 55 km (IC)
2.0×10^9	8.91×10^{13} - 1.00×10^{15}	2.00×10^{12} - 2.51×10^{13}	5.01×10^{13} - 6.31×10^{14}
5.0×10^8	3.16×10^{13} - 2.51×10^{14}	5.01×10^{11} - 6.31×10^{12}	1.26×10^{13} - 1.41×10^{14}
1.1×10^7	5.01×10^{11} - 5.62×10^{12}	1.12×10^{10} - 1.26×10^{11}	2.51×10^{11} - 3.16×10^{12}

The energy is greater than the typical value for Earth, 10^9 J. However, it is thought that Jupiter and Saturn can possess energies of 10^{12} J, while exoplanets can possess energies ranging from 10^{10} to 10^{17} J (Hodosán et al. (2021)). Furthermore, for intracloud discharges at altitudes above 50 km, such as IC and +CG, Kumar et al. (2021) indicates the presence of charged regions within the cloud itself, yielding a potential of 10^{13} J at altitudes between 50 and 55 km. Viewing the charged region as a capacitor, based on the relationship $U = CV^2/2$, assuming a charged region with a cluster radius of 5 km and thickness of approximately 1.5 km exists at 50 km and 55 km above and below the cylinder, the charge density is about 28 nC/m^3. When viewed as a capacitor, it can hold an electrostatic energy of 1.53×10^{13}J of electrostatic energy. This energy is of an order that can be reproduced using the charge density required for breakdown estimated by Kumar et al. (2021), along with parameters within the radius and thickness. Therefore, it is conceivable that lightning with a brightness of 10^9 J could possess a time constant of 2 msec.

Although the energy and luminescence duration demonstrated validity based on models and previous research, this study cannot conclude that PLD detected Venusian lightning. This is because the waveform cannot be compared with the model. The events triggered by this PLD could be either below the PLD's time resolution or noise. The model developed in this study indicates that the duration of Venusian lightning scattered light is 1.5 msec or less. On the other hand, the PLD's observation time resolution was 2 msec. Therefore, the time resolution of the PLD in this study was insufficient to achieve adequate time-resolved detection of Venusian lightning-scattered light. There is currently insufficient evidence to rule out the possibility that the data point was noise with a large amplitude. Furthermore, it is difficult to rule out the possibility that a meteorite impact occurred, which would produce a very dark meteorite emission spectrum at 700 nm. Christou (2004) suggested that Venus' meteor emit light at a brightness comparable to or greater than Earth's and to evaporate at high altitudes. Evaporation at high altitudes means it emits light more brightly and for a shorter duration than Earth's meteor glow (approximately 0.4 sec). It cannot be ruled out that Venusian shooting stars may emit intense light at a wavelength of 777 nm for a short duration. To provide more reliable evidence, future observations using PLD with improved time resolution will be necessary.

4.2.2 Evaluation of the results of Jupiter

Regarding the observation results of Jupiter, with the Earth-Jupiter distance set at 5.9×10^7 km, the PLD's FOV of 2×11 arcsec allowed observation of an area of approximately 570×3100 km^2 on Jupiter's surface. When the conditions for detecting triggered waveforms as lightning were relaxed, the detection frequency of triggered waveforms was 5.2×10^{-11} /km^2/sec. This was 37 times less than the Jupiter lightning occurrence frequency of 10^9 J (Little et al. (1999)). The frequency of Jupiter lightning events was 560 times smaller than the 10^7 J frequency reported in Becker et al. (2020). The cumulative distribution of lightning flash energies, as shown in Becker et al. (2020), is depicted in Figure 4.10.

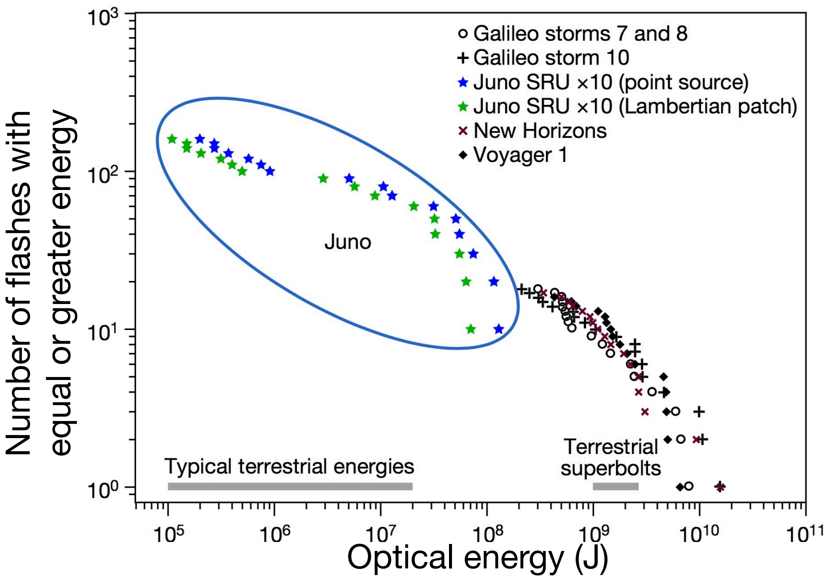

Figure 4.10: Cumulative histogram of jovian lightning optical energy. Becker et al. (2020)

Assuming the waveforms detected by the PLD would be lightning, their detection frequency was inconsistent with previous research. The triggered events were limited to the 2021 observation period. The daily average air mass values during the 2021 observation period were 1.4 times larger than those during the 2022 observation period, suggesting greater influence from seeing conditions and atmospheric absorption. According to Gouda (2014), the coherence time τ_0 of the average atmospheric turbulence in Nayoro City, where the Pirka telescope is located, was approximately 1 msec. The effect of atmospheric turbulence could not be ignored at the 2 msec measurement gate time used in PLD. Therefore, we had no choice but to set the threshold high to avoid false detection of Jupiter's dayside brightness. The lightning detection sensitivity of the PLD had decreased as a result of this analysis. In fact, lowering the threshold to 4.5σ for a distribution normalized by the standard deviation resulted in approximately 200 events, with a detection frequency comparable to the 10^9 J-class lightning occurrence frequency reported in previous studies. The reason the detection frequency in this study was lower than the lightning occurrence frequency reported in previous research may be due to the threshold-setting method.

Unfortunately, the PLD did not detect Jupiter lightning with a statistically significant and high signal-to-noise ratio capable of comparing waveforms to the model of this study. Apart from interpretations where many signals are buried in noise, one possible cause to consider was the local time dependence of lightning frequency on Jupiter. The occurrence frequency of lightning exhibits local time dependence depending on its generation mechanism. On Earth, the primary heat source driving convection is solar radiation. The heat influx differs between dayside and nightside. Sunlight heats land surfaces well during the daytime. Therefore, updrafts become active from approximately 14hr $<$ LT $<$ 19 hr. As updrafts become more active, the frequency of lightning increases during the same local time period. Lightning at ocean dependence differs from terrestrial dependence. Depending on the surveyed sea area, peaks exist between 1:00 AM and 3:00 AM local time and between 11:00 AM and 2:00 PM local time. On Jupiter, the primary heat source driving convection is internal. There is not a relatively strong local time dependency in the frequency of lightning occurrences. No previous studies have demonstrated through observations that the occurrence frequency of lightning and cumulonimbus clouds exhibits local time dependence. Visible light observations of lightning had focused on nightside observations by spacecraft. In the electromagnetic wave observations of lightning, waveforms considered to originate from lightning were not observed exclusively on the night side. Cumulonimbus clouds are thought to exist dayside and nightside based on visible light observations (e.g. Gierasch et al. (2000)) and infrared observations (e.g. Brueshaber et al. (2025)). Therefore, it is considered that there is no local time dependence in the frequency of lightning occurrences on Jupiter. Even if there is a dependency, it is considered very minimal. Since Jupiter has no land surface, it is assumed to be similar to lightning over Earth's oceans. Oceans warm more slowly than land due to their higher specific heat capacity. They agree that solar heating is weak. Assuming that Jupiter lightning and Earth oceanic lightning exhibit similar local time dependencies. The PLD observed LT 12:00. This observation period coincided with Earth's peak period of oceanic lightning. It is difficult to explain the failure to statistically detect Jupiter lightning statistically using local time dependence.

PLD observed event had a FWHM of approximately 3.5 msec and a peak value of about 10^9 J. The observed FWHM was 0.4 times the maximum FWHM of 8 msec in the light curve of the cumulonimbus structure according to this model. In comparison, it was 1.8 times the maximum FWHM of 2 msec in the light curve of the Jupiter stable cloud structure. Due to being buried by noise, caution was required regarding waveform distortion caused by bandpass processing. If the observed event was considered to be lightning occurring at a high altitude, the FWHM did not match. However, this may be interpreted as a difference in discharge time or cloud structure that was not accounted for in the model. If lightning occurs multiple times or if lightning discharges persist for milliseconds, the result would likely be superimposed scattered light curves with temporal offsets introduced by the discharge currents. Alternatively, the cloud structure could be interpreted as occurring midway between the cumulonimbus clouds and the stable conditions compared in this study, suggesting that Jupiter's cumulonimbus clouds formed during their development. This interpretation was also supported by the fact that frequent lightning occurs during the development of cumulonimbus clouds in terrestrial lightning.

4.3 Visible duration time of planetary lightning

Observations from the PLD and model results were expected to suggest new constraints on the time constant of lightning. This section reorganized qualitative hypotheses from previous studies from the perspective of time constants.

4.3.1 Jovian time constants

The non-detection of bright, long-duration pulses 2 msec on Jupiter was interpreted not as a failure of the model, but as a constraint imposed by the instrument' s sensitivity. For a waveform with total energy and duration $t_{duration}$, the peak power can be approximated by dividing the total energy by the duration. Observations in the 2000s showed the maximum luminous energy reached 1.8×10^{18}J. For the peak power to be less than the peak power of the PLD triggered by the results of this analysis, it was considered to have had a duration of 13 msec or longer based on the following equation.

$$\frac{5.5 \times 10^9}{3.7} > \frac{1.8 \times 10^{10}}{t_{duration}} \tag{34}$$

This duration of approximately 10 msec was comparable to the occurrence frequency demonstrated in studies showing Jupiter lightning's similarity to Earth's IC (Kolmašová et al. (2023)). In one instance, ten whistler waveforms originating from lightning discharges were observed within 16 msec. This indicates that when approximately ten lightning discharges, each with an energy of around 10^8 J, occur in succession, they may be observed as a single lightning event with an energy of 10^9 J during imaging with an exposure time exceeding several tens of milliseconds. When multiple lightning strikes occur simultaneously, multiple peaks are expected to appear in the observed light curve. Each peak value corresponds to lightning with an energy of 10^7 to 10^8 J. To verify whether multiple lightning strikes overlapped, it is necessary to observe the light curves of these smaller lightning events.

Comparing the results of the model developed in this study with those of prior studies yielded new findings that re-examined the hypothesis proposed in those studies, based on two-dimensional images, from the perspective of time constants. It was demonstrated that the time constant of the lightning height curve caused by submillisecond discharges occurring within cumulonimbus clouds is 8 msec or less. This result is consistent with the findings of previous studies using Juno, SRU (Becker et al. (2020)). The lightning occurrence altitude estimated from images captured by Juno's SRU is believed to be shallower than 3 bar, occurring near 1 bar at 5.4 msec. Based on the FWHM and HWHM estimated from this result, we evaluate the appropriate cloud structure and phase function parameters when discussing cumulonimbus cloud structure. This study also suggests that even when estimated conservatively, it is 7.9 msec or less. (as indicated in the appendix). Prior studies estimate the HWHM to be less than 30 km. Assuming lightning discharges occur directly beneath the cumulonimbus cloud, an HWHM of less than 30 km corresponds to a light source altitude below 2 bar. Furthermore, results showing FWHM values between 7.9 and 5.4 msec at altitudes below 2 bar are consistent with the parameters of the Two-Term Henyey-Greenstein function estimated by Pioneer

10 (Tomasko et al. (1978)). Based on the above, the lightning observed by Juno SRU with durations of 5.4 msec or less suggests that it originated within cumulonimbus clouds at shallow brightness levels of 2 bar or higher. This was consistent with the emergence altitude suggested in previous studies.

It is necessary to consider the discharge time. Imai et al. (2018) suggested that the discharge duration was hundreds of microseconds based on waveforms from the Microwave Radiometer (MWR) onboard Juno. Furthermore, this study estimated that the lightning discharge duration is less than 1 msec based on the waveform of the UVS installed on Juno. The waveform of the luminous phenomenon thought to originate from TLEs has had its light curve estimated from Giles et al. (2020). TLEs are thought to occur at higher altitudes in the ionosphere and mesosphere than visible lightning, and thus are unaffected by cloud scattering. Because they are unaffected by scattering, the decay time (Absorption time) and diffusion time around the waveform peak are nearly identical. In contrast, the visible light range is affected by scattering. Therefore, visible light waveforms observed by JEM-GLIMS for sprites and TLEs show a longer duration after the peak compared to TLE waveforms. Given that the UVS waveform duration is approximately 1.4 msec, the visible light scattering waveform is thought to show a duration of 2 msec or longer. Considering that the duration of TLEs and lightning discharges is nearly identical, this aligns with the previously mentioned 1 msec order discharge phenomena. However, the UVS observed waveform closely resembles both the visible light waveform and the visible light waveform obtained from the model, exhibiting a post-peak duration (scattering time) approximately twice as long as the decay time. This exhibits the typical decay time seen in lightning waveforms originating from cloud scattering. The altitude where the Jupiter TLE is thought to occur is 250 km, more than 200 km above the cloud tops. Therefore, it is considered unlikely to be affected by cloud scattering. Consequently, it cannot be definitively stated that the events observed by Juno's UVS are necessarily lightning-derived TLEs. The model developed in this study does not account for absorbing substances such as ozone. Furthermore, the H_2 emission line near 160 nm falls outside the wavelength range of this model. Modifications to this model are necessary to examine the waveforms observed by UVS.

4.3.2 Venusian long-duration lightning

Comparing the waveforms observed by the LAC onboard the Akatsuki spacecraft with the PLD results, the PLD values are significantly shorter. The waveform shown in Figure 1.2, considered to originate from lightning based on LAC measurements, exhibited an FWHM of approximately 50 msec, a rise time of 60 msec, and a fall time of 170 msec. A second peak was also visible at +60 msec, suggesting it could represent multiple overlapping lightning events, such as a subsequent return stroke. The FWHM of the first peak was 30 msec. If the FWHM of the first peak is considered equal to the FWHM of the lightning discharge emission occurring during a single discharge in Venus's atmosphere, this is consistent with the upper limit value inferred from ground-based telescope results. However, compared to the waveform observed by the PLD, the PLD trigger event is extremely short. Furthermore, with only one waveform detected by LAC and four trigger events by PLD, the sample size is insufficient for statistical comparison, raising the possibility that this was a chance measurement of a special event.

If we assume that the waveform observed by LAC is due to a submillisecond discharge phenomenon, the required number density is 730 times the normal number density.

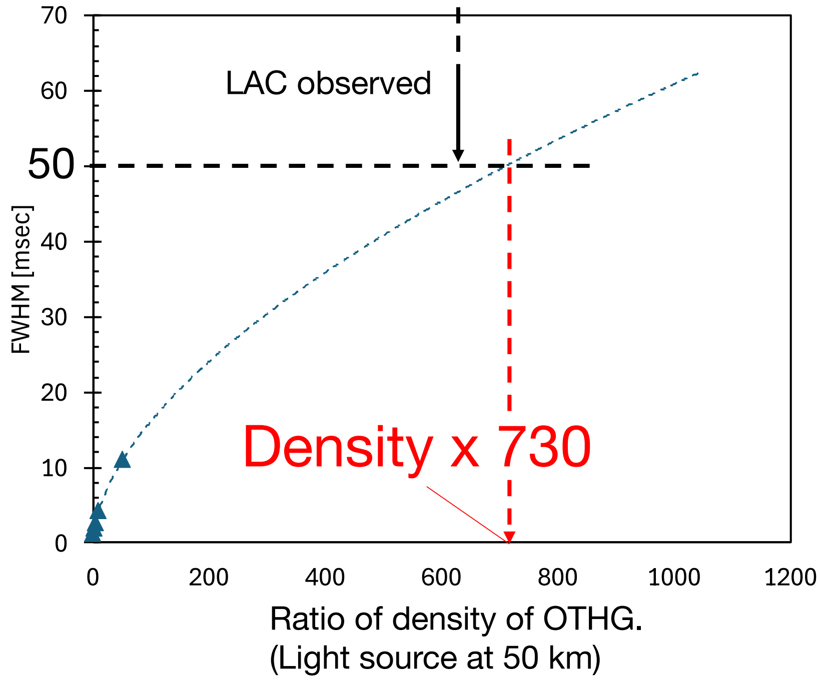

Figure 4.11: Plot of variations in FWHM as a function of X-fold increases in number density. The blue triangle indicates the model results. The blue dot line indicates the extrapolated results.

Figure 4.11 plotted the change in FWHM when the number density was varied by a factor of N. The FWHM when the cloud number density used in this study's model is multiplied by N, where N is the value on the horizontal axis, is shown on the vertical axis. It was estimated that a cloud with approximately 300 times the number density existed for the FWHM to reach about 30 msec. It was estimated that a cloud with approximately 730 times the number density existed for the FWHM to reach about 50 msec.

This study is the first to quantitatively demonstrate the required cloud number density. However, this proposal was refuted for the following two reasons. The first is that the number density is too large relative to the local fluctuations in number density revealed by infrared observations. When the number density increases locally, it can also be observed as optical thickness at other wavelengths. According to previous studies, the optical thickness contrast ranged from approximately 3 to 100 percent. Since optical thickness is nearly proportional to number density, this equates to a local difference in number density of approximately twofold when converted to number density. In contrast, the ratio estimated from the model in this study is over 300 times higher and does not match. Second, the energy required based on transmittance exceeds the electromagnetic energy anticipated from prior research. Transmittance decreases exponentially with respect to number density. Therefore, when the number density increases by a factor of 300 or more without significant dependence on altitude, the transmittance decreases by a factor of approximately 10^{-300}. This is equivalent to the amount of energy emitted during luminescence increasing by a factor of 10 to the power of 300 for the same luminescence energy to be observed. It is necessary to consider that the electric field conditions in Venus's atmosphere change as the number density varies; however, the energy that can be retained before dielectric breakdown occurs in Venus's atmosphere is considered far too small relative to the required value. Based on the above two points, it is unlikely that there was a change in number density of several hundred times. The lightning observed by LAC is thought to be the result of long-duration discharges or multiple lightning strikes occurring simultaneously.

This study verified whether the model could reproduce the LAC observations by assuming Earth-like long-duration lightning occurred on Venus. The model developed in this study didn't account for discharge time. However, the effect of the discharge time can be expressed as the convolution integral between the discharge time and the scattered waveform obtained from the model. The long-duration discharge waveform of Earth was derived using the visible light curve observed by JEM-GLIMS. The scattered waveform accounted for multiple generation altitudes and variations in cloud number density. For scattered waveforms with normal number density, simulation results were obtained using TTHG phase function and the model considering uppermost haze (Karyu et al. (2024)). For scattered waveforms with modified number density, simulation results were obtained using OTHG phase function and the standard model of Haus et al. (2014), scaled by factors of 0.1, 3, and 10 across the entire altitude range. This study calculated the correlation coefficient between the folded and integrated results of both components and the LAC observation results.

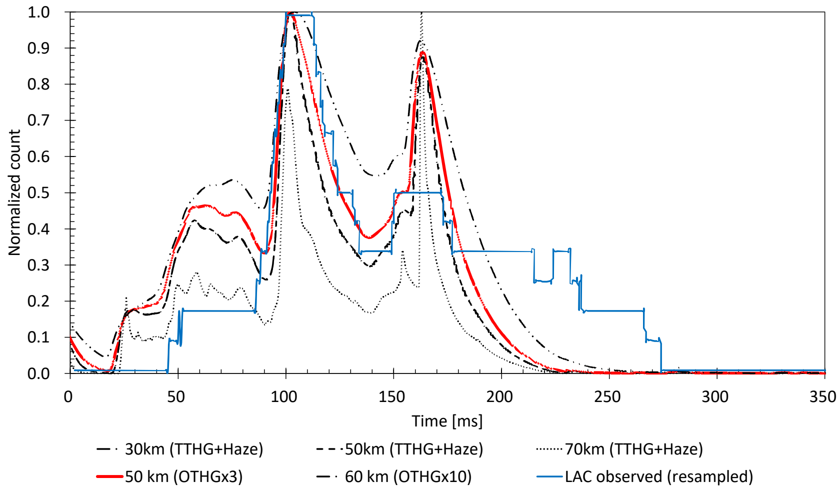

Figure 4.12: Comparison between the waveform observed by LAC and the simulated waveform. The simulation assumes a long-duration lightning discharge based on terrestrial characteristics observed by JEM-GLIMS. The blue line indicates the LAC observed results. The red line indicates that the simulated results reproduced the same FWHM as the initial peak in the long-duration waveform observed by LAC. For the normal density, results are shown for lightning occurring at altitudes of 30 km, 50 km, and 70 km. For the adjusted number density, results are shown for lightning occurring at altitudes of 50 and 60 km.

By utilizing the scattered waveform of Venusian lightning occurring at a density three times higher and an altitude of 50 km, we reproduced the same FWHM as the initial peak in the long-duration waveform observed by LAC (red line, Figure 4.12). The clouds with three times the number density were consistent with previous infrared observations (Belton et al. (1991), Tsang et al. (2009)). The change in number density was within the range reported in previous studies. Therefore, the hundreds-of-millisecond lightning discharges observed by LAC suggested that processes similar to those occurring in long-duration discharges on Earth may have taken place. This result was the first verification of the possibility that the LAC-observed light curve of Venusian lightning was caused by an Earth-like long-duration discharge.

4.4 Limitations of this model

Our model can represents the event similar to previous result. However, our model has limitations. Dependence on the input cloud structure model

Based on the results of one-dimensional cloud formation numerical simulations incorporating chemical reactions and probe observations, we developed a lightning scattering model considering the cloud structure of cumulonimbus clouds. However, the cylindrical cloud shape assumed in this study may cause discrepancies with reference research. In previous studies, models considering parallel plates failed to reproduce the lightning images observed by Galileo. Therefore, models incorporating a three-dimensional hemispherical cloud structure were introduced to provide a consistent explanation of the observational results. It has been suggested that the HWHM and the lightning occurrence altitude are proportional. Our model employs a cylindrical cloud structure equivalent to parallel plates. Consequently, deviations from the proportional relationship were observed around 2 bar, likely due to assumptions about cloud generation without cumulonimbus clouds. Methods for setting cloud shapes as spherical or arbitrary forms are implemented in CloudScat.jl, the simulation model foundation we use. We are currently advancing investigations using models incorporating these functionalities.

When rigorously comparing with previous studies, it is important to note that the altitude at which model calculations were performed in this study is limited. When the model in this study targets altitudes up to 5 bar, the maximum HWHM value is below 50 km. In contrast, observations by the Juno probe estimate the HWHM maximum to be below 59 km. Furthermore, observations by the Galileo probe report the HWHM as widely distributed within the range of 32 to 87 km. Since this study limits the examined altitude to a maximum of 5 bar (or 4 bar for some models), it is insufficient for comparing results with observations from depths below 5 bar or with prior research. Model calculations considering deeper altitudes up to 10 bar are currently underway. This will enable verification of the reproducibility of the large HWHM suggested by probe observations and advance the estimation of the FWHM of the light curve.

Furthermore, there are issues with the dependency of the cloud number density distribution. There are thunderstorms that the Sugiyama model fails to explain their intermittency. (Brueshaber et al. (2025)) Recent radio observations suggest lightning may occur outside the immediate sub-cloud deck of cumulonimbus structures. (Imai et al. (2020)) As demonstrated by the model results, there is a four times difference in the duration of lightning strikes occurring at depths of several bars or less between cumulonimbus clouds and stable clouds. Regarding the lightning brightness curves of Venus and Jupiter, it will be necessary to clarify the relationship between future cloud structures and lightning light curves.

Actual lightning discharges are not necessarily point sources. They exhibit spatial spread in both horizontal and vertical directions. Furthermore, the discharge propagates at a velocity. Both the light source position and the offset relative to the emission start time must be considered. The temporal evolution of the discharge can be reproduced using the convolution integral of the current waveform and the scattered waveform.

Regarding the spatial spread, it is expected that this can be reproduced by placing light sources at multiple positions, performing model calculations, and then superimposing the results. Using images from the LSI onboard JEM-GLIMS as reference, this study will evaluate the relationship between horizontal discharge progression and luminosity curves, and consider verification using a model.

4.5 Future observations by PLD

We apply the inverse correlation to the Venus results. Based on Hansel's results, if the duration of a 10^9 J event is 50 msec, the duration of a 10^7 J event is 1 second. This expected duration time is longer than the LAC results. However, if the duration of a 10^9 J event is 1 msec, as inferred from PLD and our model results, the duration of a 10^7 J event is 100 msec. The predicted duration time would be consistent with the LAC (and Venera) results. Venusian lightning discharges would exhibit characteristics similar to those of Earth's lightning.

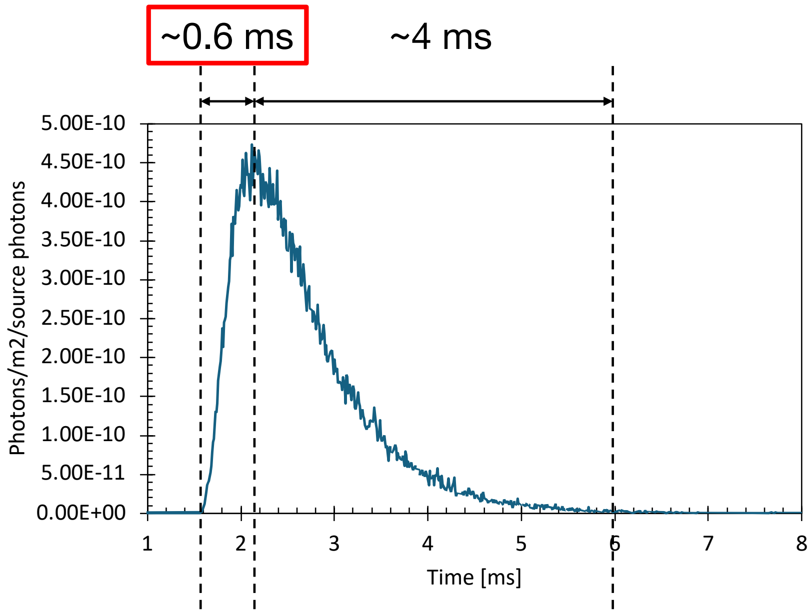

Figure 4.13: Simulation results of the light curve of Venusian lightning assuming an occurrence altitude of 50 km.

Our model have suggested the prior time resolution is 0.3 msec. Based on our model results (Figure 4.13), 0.3 msec is necessary to fully resolve the waveform for Venusian lightning. The rise time was about 0.6 msec if lightning occur at 50 km on Venus. To resolve it, at least half of its time resolution would be required. Using this model results, we can improved time resolution and signal to noise ratio for future observations.

The observed trends on Earth may not be consistent with Jovian lightning with respect to time constants. We apply the inverse relationship to Jupiter, too. Based on our model results, if the duration of the 10^9 J event is 1 msec, the duration of a 10^7 J event would be 100 ms. The expected duration time is longer than the Juno results. On the other hand, based on SRU results, the duration of a 10^9 J event would be submillisecond. The predicted duration is shorter than that simulated by this model, considering the structure of cumulonimbus clouds. Some stable cloud structure models can simulate scattered-light curves on the submillisecond timescale. More complex discharges may be occurring on Jupiter. It is necessary to clarify the waveform with a high signal-to-noise ratio.

To confirm the multiple-discharge hypothesis and observe the component 10^7 to 10^8

J events, a reduction in noise variance and an increase in sensitivity are required. Currently, the apparatus can only reliably observe 10^9 J class events when using a 4σ trigger threshold. We propose two options for upgrading the PLD. First,Incorporate two units operating at the 656 nm wavelength, with background fluctuations measured simultaneously by the CCD. This configuration would significantly reduce noise variance and is highly feasible, requiring only a filter exchange. Second, Select and integrate a new sensor with inherently lower dispersion noise characteristics. The implementation of Option 1 is currently being prioritized and studied, as it offers the quickest route to achieving the necessary sensitivity to observe the component 10^7 to 10^8 J events and definitively test the multiple-discharge hypothesis.

The modified PLD should be set to either 2.3 msec or 0.35 msec, based on the model results of this study. Considering cumulonimbus clouds, the rise time of the light curve for lightning occurring at 2 bar pressure was 4.5 msec (4.14a). Considering stable clouds, the rise time of the light curve for lightning occurring at 2 bar pressure was 0.7 msec (4.14b). To observe the rise time with temporal resolution, observations should be made with a resolution exceeding half the period. Therefore, this study suggested that observations should be made with a temporal resolution of 2.3 msec or higher for lightning assumed to originate from cumulonimbus clouds, and with a resolution of 0.35 msec or higher for observations in stable conditions.

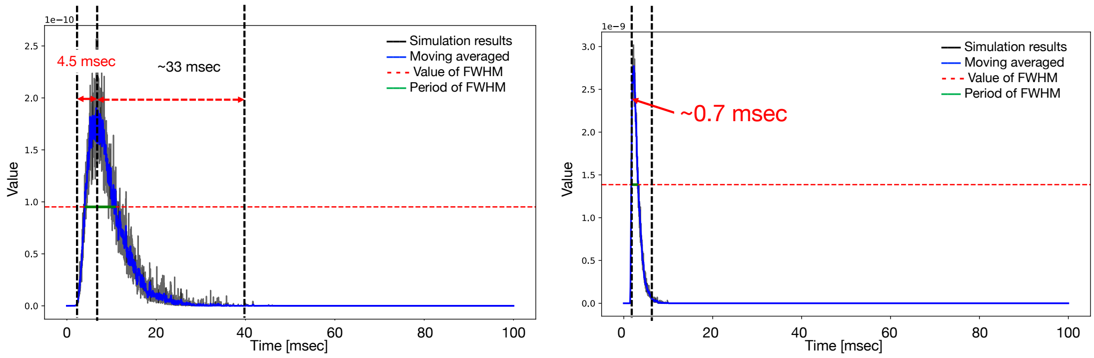

(a) Simulated light curve in cumulonimbus (b) Simulated light curve in stable cloud

Figure 4.14: Simulation results of the light curve of Jovian lightning assuming an occurrence altitude at 2 bar atmospheric pressure. (a) considered cumulonimbus clouds. (b) considered a stable cloud. Both simulation models were obtained by R10S3 with TTHG.

5 Conclusion

This study developed an observational instrument (PLD) and a simulation model to obtain new findings on the light curves of Venusian and Jovian lightning that previous studies could not investigate. PLD observed Venus and Jupiter with 2 msec temporal resolution, which is higher than the 50 msec exposure time of previous ground-based telescope observations. This model was validated by reproducing the light curves observed by JEM-GLIMS, as well as the altitude-dependent differences in transmittance and FWHM.

This study provided new constraints on the temporal characteristics of the light curves of Venusian and Jovian lightning. This study revealed that the time constant of the Venus lightning light curve originating from submillisecond discharges is less than 2 msec. Although it would be necessary to investigate the dependence of cloud structure on this model, it validates Juno's 2-bar-level lightning using the time constant rather than the spatial extent in 2D images studied by previous studies for the first time. This study suggested that a lightning light curve observed by the LAC onboard Akatsuki was generated by an Earth-like long-duration discharge. This study verified that, assuming long-term discharge on Earth, it is reproducible under conditions with cloud particle number densities several times higher than those of the standard cloud structure on Venus. This study focused on the low detection frequency of Jovian lightning and the near-invisibility of its light curves, buried in noise. It indicated that the lightning observed by Galileo, with an energy exceeding 10^9 J, has a timescale of at least 13 msec and could be interpreted as the superposition of multiple lightning events. While previous studies have discussed the possibility of multiple lightning events, this study focused on the timescale and, based on visible-light observations, organized the interpretation into a framework with specific temporal characteristics.

This study suggested that the prior temporal resolution for the Venusian lightning light curve is higher than 0.3 msec. This model's results indicated that the rise time of Venusian lightning would be 0.6 msec. Given the prior temporal resolution required to resolve this rise waveform, the necessary time resolution would be half this period. This study demonstrated that reducing instrument noise is crucial for additional observations of Jupiter using PLD and presented specific modification proposals.

This study has been fundamental research applicable not only to future Venus and Jupiter exploration missions but also to missions to other planets where lightning is suggested to occur. The results of this study could be incorporated not only into future PLD observations but also into future exploration plans. The JANUS camera onboard the JUICE, scheduled for arrival in 2031, plans to conduct video observations of Jupiter lightning. Based on the observational and modeling results of this study, we can provide reference values for selecting exposure durations and observational methods for Jupiter lightning video observations. We can interpret the Janus observational results and re-evaluate this study by re-verification and rerunning the model calculations.

Appendix

AppendixA Planetary lightning emission spectrum and wavelength band of the PLD

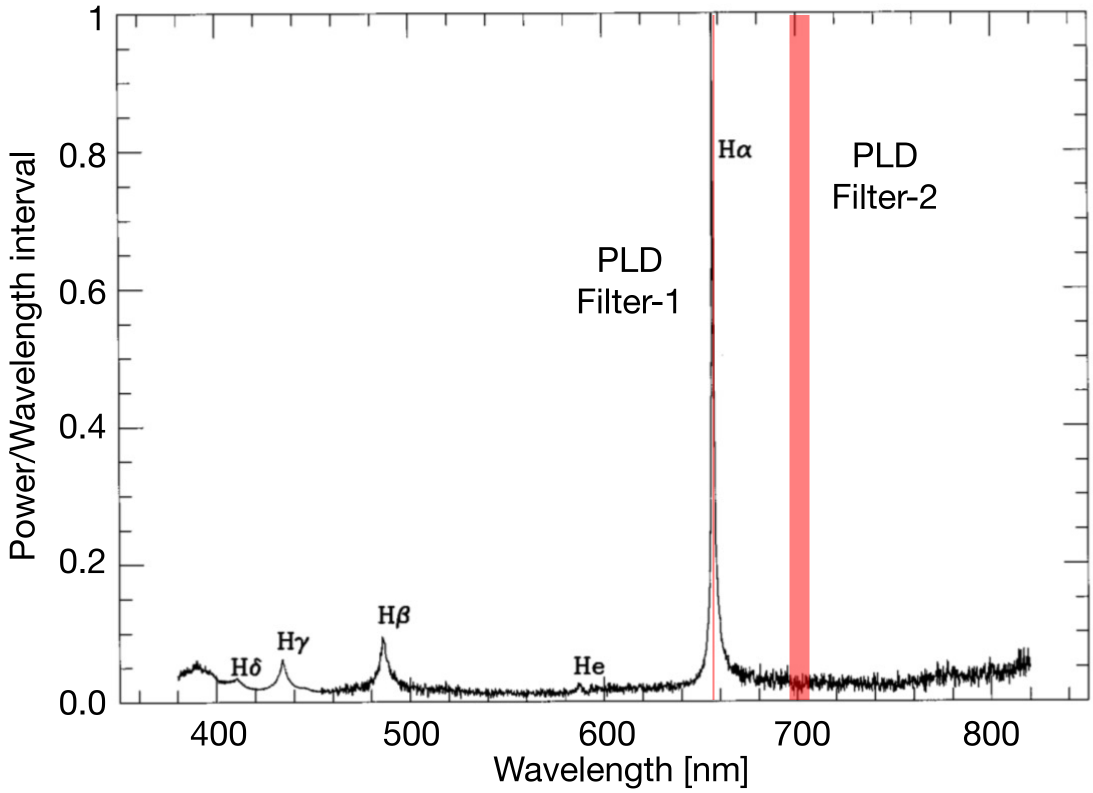

Figure A.1: Comparison between the Jovian lightning emission spectrum obtained from laboratory experiments (W. Borucki et al. (1985)) and the observational wavelength band of the Planetary Lightning Detector (PLD) for Jupiter (red shaded area).

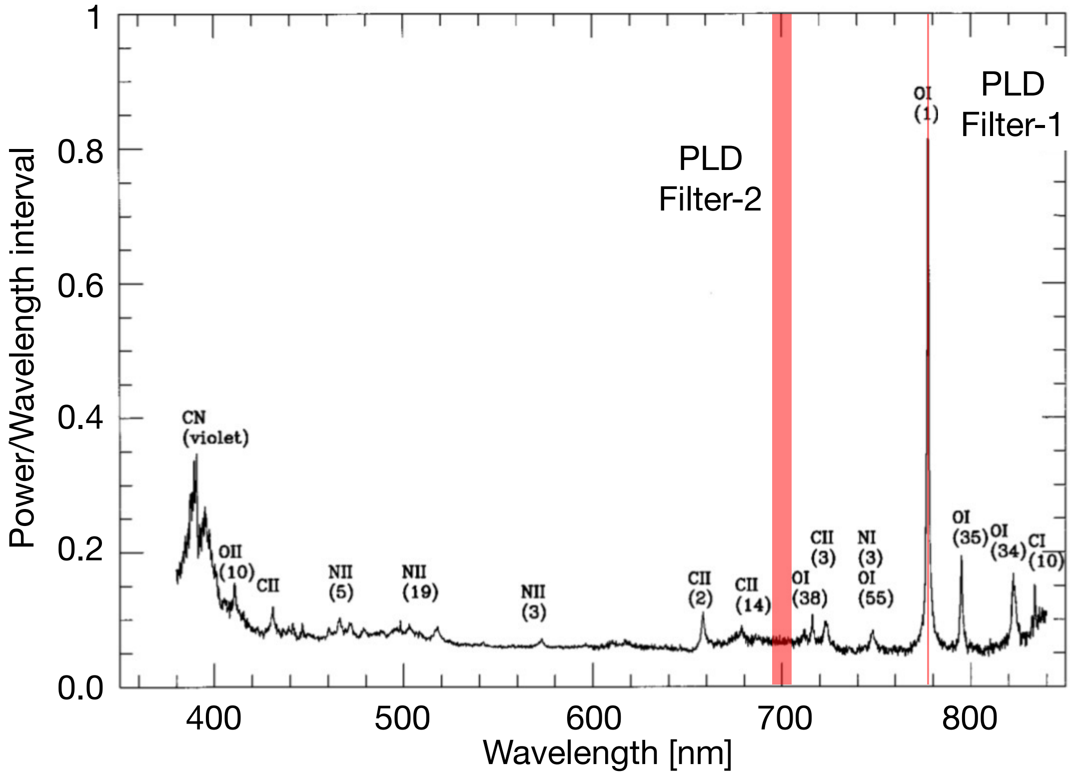

Figure A.2: Comparison between the Venusian lightning emission spectrum obtained from laboratory experiments (W. Borucki et al. (1985)) and the observational wavelength band of the Planetary Lightning Detector (PLD) for Venus (red shaded area).

AppendixB Images of this model results

Jupiter model results

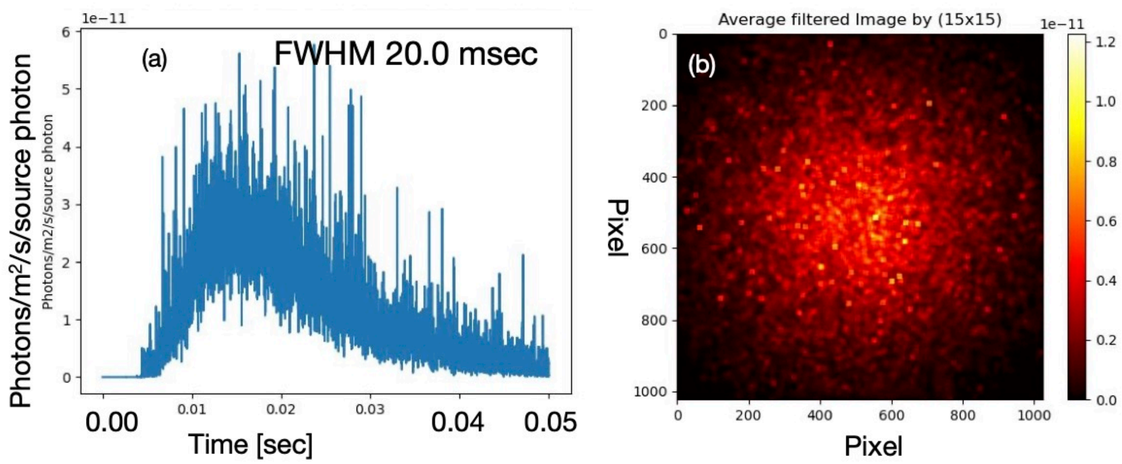

Figure B.1: Simulated results of R10S10Q using TTHG with $z = 35$km lightning. (a) Simulated light curve, (b) Simulated images

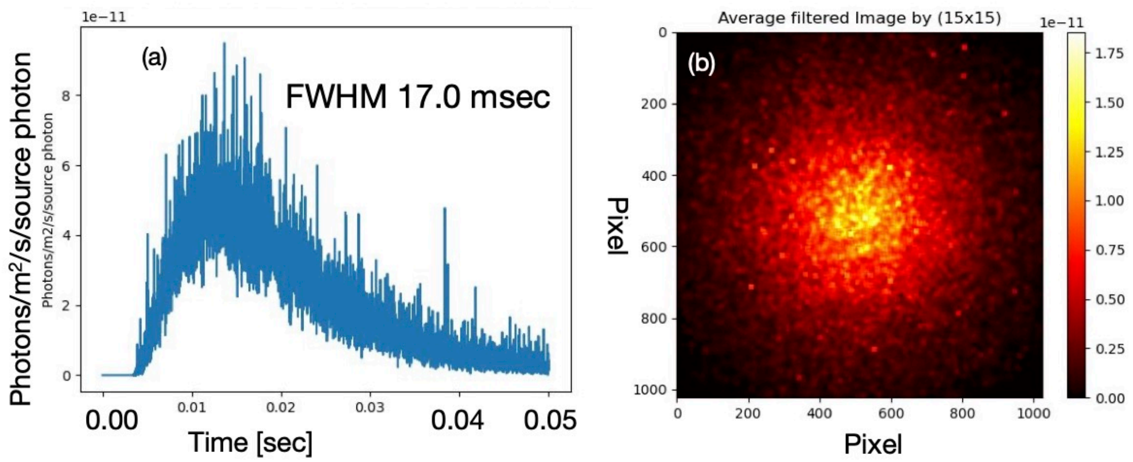

Figure B.2: Simulated results of R10S10Q using TTHG with $z = 59$km lightning. (a) Simulated light curve, (b) Simulated images

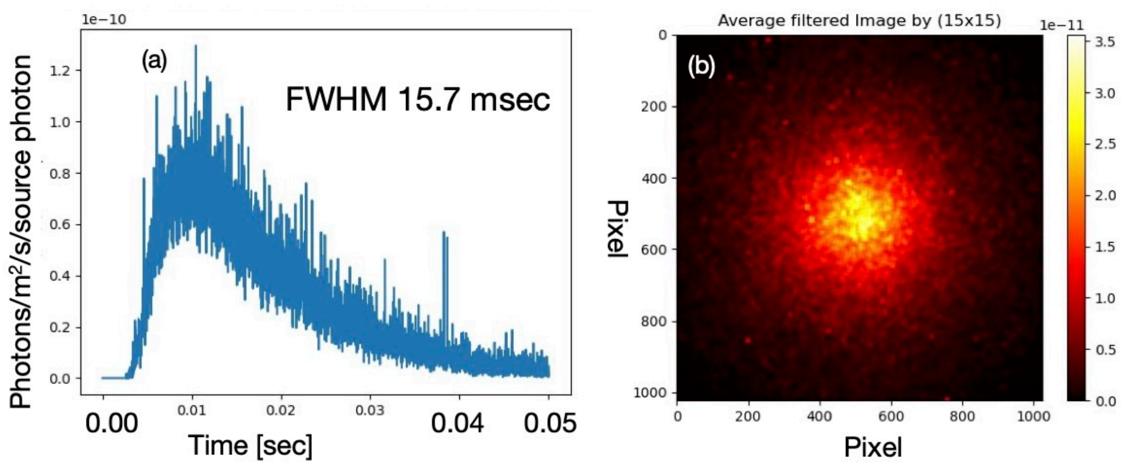

Figure B.3: Simulated results of R10S10Q using TTHG with $z = 80$km lightning. (a) Simulated light curve, (b) Simulated images

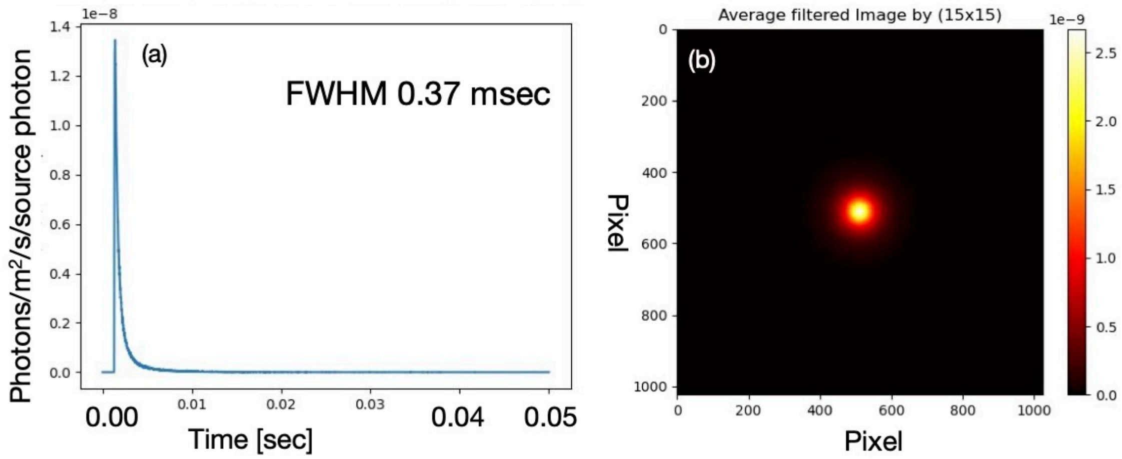

Figure B.4: Simulated results of R10S10Q using TTHG with $z = 111$km lightning. (a) Simulated light curve, (b) Simulated images

AppendixC Analysis of Juno Stellar Reference Unit (SRU)

The Stellar Reference Unit (SRU) utilized the rotation of the Juno spacecraft during 100-millisecond exposures to estimate the duration and spacing of lightning flashes. This observational method mirrors the technique used in late 19th-century photography to study lightning discharge paths by moving the camera and altering the imaging position on the film, predating the development of cameras capable of high-time-resolution observations. Therefore, we estimate the upper limit of the FWHM for Jupiter's lightning light curve by creating cross-sectional diagrams of the uncorrected SRU scan data, as shown in Becker et al. (2020), which does not account for the spacecraft's rotation. In Becker et al. (2020), verification was performed by removing solar components and estimating FWHM. However, for the target images, only one bright waveform that could be separated from the background was extractable. Therefore, to estimate the upper limit of FWHM, we simply treat cross-sectional images as light curves to increase the number of waveform examples. Following the procedure in Becker et al. (2020), the optical system effects of the SRU are corrected by performing an inverse convolution integral of the SRU's Point Spread Function on the raw data. The number of deconvolution iterations was set to 300. Figure C.1 shows the image obtained from the PSF convolution result in Figure 1.4 from Becker et al. (2020).

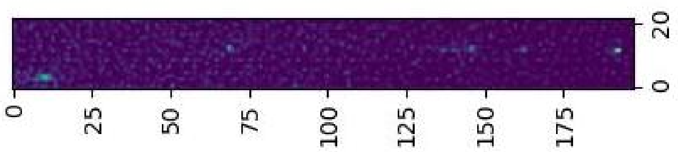

Figure C.1: Deconvoluted image sccaned by SRU shown in Becker et al. (2020)

The cross-sectional image $I(x, y)$ (y = 0,1,..., number of image pixel) closely matches the light curve of the lightning flash. However, when the probe's rotation speed is sufficiently slow relative to the spreading speed of the scattered light from the lightning, smear occurs between adjacent pixels on the cross-sectional image. To remove this smear effect, this study assumes that the pixels immediately adjacent to the acquired image also suffer smear effects equivalent to those in the vertical direction. The average value of these adjacent pixels was calculated as the smear light curve. Furthermore, correction was performed by subtracting the resulting smear component from the light curve of the pixel exhibiting the maximum value.

$$L(x, y) = I(x, y) - \frac{I(x-1, y) + I(x+1, y)}{2} \tag{35}$$

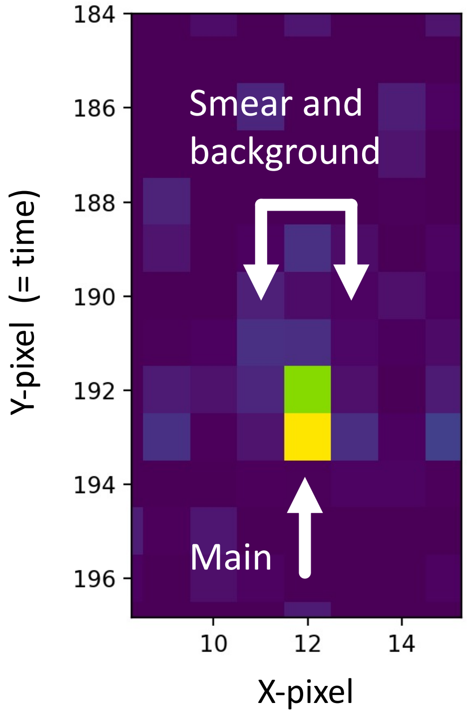

Figure C.2: Diagram of light curve estimation from SRU images with no time integrated calibration.

The waveform at the location where the peak is confirmed is shown in Figure C.3.

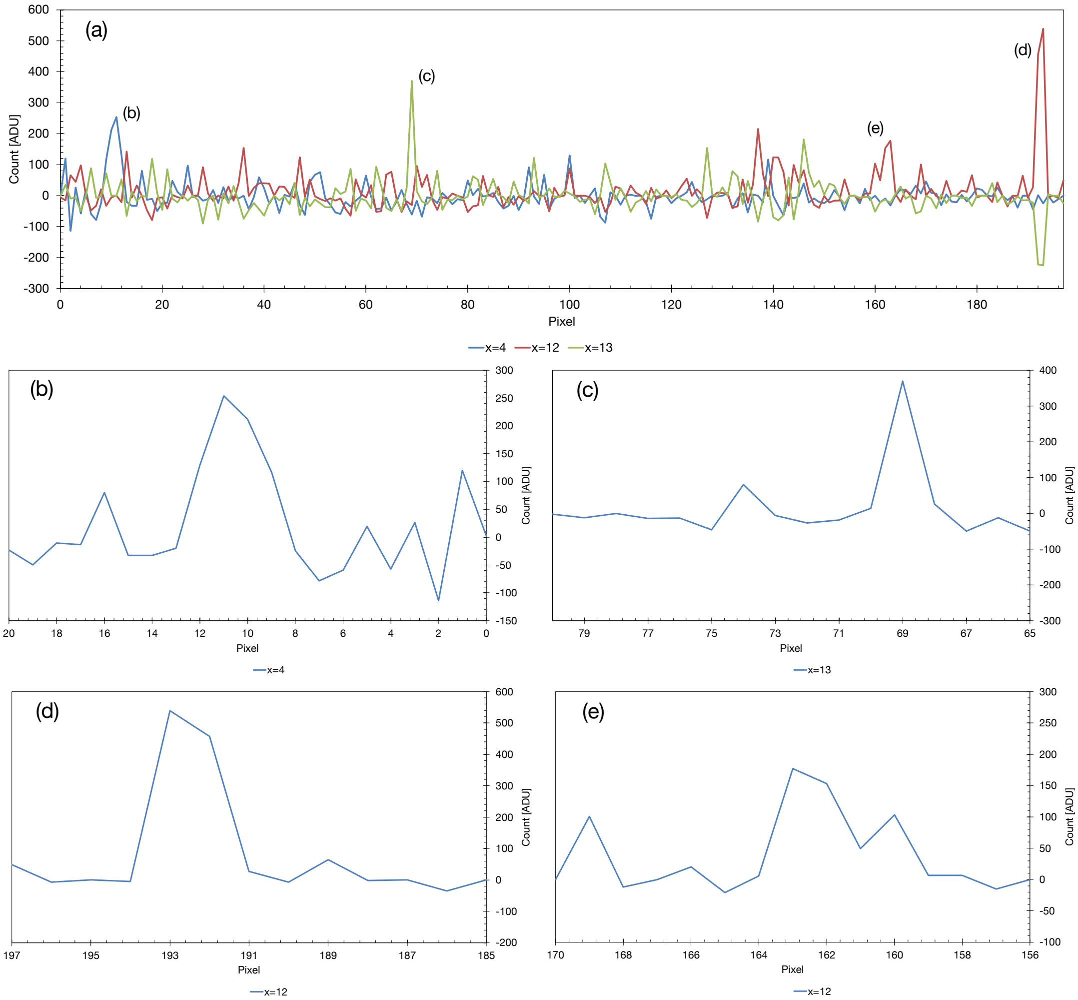

Figure C.3: Deconvoluted image cross section of SRU

Based on the probe JUNO's instantaneous velocity, the exposure time per pixel is estimated to be 2.7 msec. Therefore, multiplying the number of pixels in the acquired cross-sectional image by 2.7 msec defines the upper limit of the FWHM. As a result, the upper limit is defined here as 3.43 to 7.94 msec. Note that some waveforms exceed the upper duration limit of 5.4 msec estimated in previous studies using lightning images. This study uses these values solely as a reference for the upper limit.

References

Baines, K. H., Simon-Miller, A. A., Orton, G. S., Weaver, H. A., Lunsford, A., Momary, T. W., ... Ressler, M. E. (2007, October). Polar Lightning and Decadal-Scale Cloud Variability on Jupiter. *Science*, *318*(5848), 226. doi: 10.1126/science.1147912

Bandholnopparat, K., Sato, M., Adachi, T., Ushio, T., & Takahashi, Y. (2019, August). Optical properties of intracloud and cloud-to-ground discharges derived from JEM-GLIMS lightning observations. *Journal of Atmospheric and Solar-Terrestrial Physics*, *189*, 87-97. doi: 10.1016/j.jastp.2019.04.005

Bar-Nun, A., & Podolak, M. (1985). The contribution by thunderstorms to the abundances of co, c2h2, and hcn on jupiter. *Icarus*, *64*(1), 112-124. Retrieved from `https://www.sciencedirect.com/science/article/pii/0019103585900429` doi: https://doi.org/10.1016/0019-1035(85)90042-9

Becker, H. N., Alexander, J. W., Atreya, S. K., Bolton, S. J., Brennan, M. J., Brown, S. T., ... Steffes, P. G. (2020, August). Small lightning flashes from shallow electrical storms on Jupiter. Nature, *584*(7819), 55-58. doi: 10.1038/s41586-020-2532-1

Belo-Pereira, M. (2025, May). Forecasting Cumulonimbus Clouds: Evaluation of New Operational Convective Index Using Lightning and Precipitation Data. *Remote Sensing*, *17*(9), 1627. doi: 10.3390/rs17091627

Belton, M. J. S., Gierasch, P. J., Smith, M. D., Helfenstein, P., Schinder, P. J., Pollack, J. B., ... Pilcher, C. B. (1991). Images from galileo of the venus cloud deck. *Science*, *253*(5027), 1531-1536. Retrieved from `https://www.science.org/doi/abs/10.1126/science.253.5027.1531` doi: 10.1126/science.253.5027.1531

Blaske, C. H., O'Rourke, J. G., Desch, S. J., & Borrelli, M. E. (2023). Meteors may masquerade as lightning in the atmosphere of venus. *Journal of Geophysical Research: Planets*, *128*(9), e2023JE007914. Retrieved from `https://agupubs.onlinelibrary.wiley.com/doi/abs/10.1029/2023JE007914` (e2023JE007914 2023JE007914) doi: https://doi.org/10.1029/2023JE007914

Bodhaine, B. A., Wood, N. B., Dutton, E. G., & Slusser, J. R. (1999). On rayleigh optical depth calculations. *Journal of Atmospheric and Oceanic Technology*, *16*(11), 1854 - 1861. doi: 10.1175/1520-0426(1999)016¡1854:ORODC¿2.0.CO;2

Borucki, W., Mc Kenzie, R., McKay, C., Duong, N., & Boac, D. (1985). Spectra of simulated lightning on venus, jupiter, and titan. *Icarus*, *64*(2), 221-232. Retrieved from `https://www.sciencedirect.com/science/article/pii/0019103585900879` doi: https://doi.org/10.1016/0019-1035(85)90087-9

Borucki, W., McKay, C., Jebens, D., Lakkaraju, H., & Vanajakshi, C. (1996). Spectral irradiance measurements of simulated lightning in planetary atmospheres. *Icarus*, *123*(2), 336-344. Retrieved from `https://www.sciencedirect.com/science/article/pii/S0019103596901621` doi: https://doi.org/10.1006/icar.1996.0162

Borucki, W. J., Dyer, J. W., Phillips, J. R., & Pham, P. (1991). Pioneer venus orbiter search for venusian lightning. *Journal of Geophysical Research: Space Physics*, *96*(A7), 11033-11043. Retrieved from https://agupubs.onlinelibrary.wiley.com/doi/abs/10.1029/91JA01097 doi: https://doi.org/10.1029/91JA01097

Borucki, W. J., Dyer, J. W., Thomas, G. Z., Jordan, J. C., & Comstock, D. A. (1981). Optical search for lightning on venus. *Geophysical Research Letters*, *8*(3), 233-236. Retrieved from https://agupubs.onlinelibrary.wiley.com/doi/abs/10.1029/GL008i003p00233 doi: https://doi.org/10.1029/GL008i003p00233

Brown, S., Janssen, M., Adumitroaie, V., Atreya, S., Bolton, S., Gulkis, S., ... Connerney, J. (2018). Prevalent lightning sferics at 600 megahertz near jupiter's poles. *Nature*, *558*(7708), 87–90. Retrieved from https://doi.org/10.1038/s41586-018-0156-5 doi: 10.1038/s41586-018-0156-5

Brueshaber, S. R., Zhang, Z., Rogers, J. H., Eichstädt, G., Orton, G. S., Grassi, D., ... Bolton, S. (2025). Multi-instrument sounding of a jovian thunderstorm from juno. *Icarus*, *432*, 116465. Retrieved from https://www.sciencedirect.com/science/article/pii/S0019103525000120 doi: https://doi.org/10.1016/j.icarus.2025.116465

Cardesín Moinelo, A., Abildgaard, S., García Muñoz, A., Piccioni, G., & Grassi, D. (2016). No statistical evidence of lightning in venus night-side atmosphere from virtis-venus express visible observations. *Icarus*, *277*, 395-400. Retrieved from https://www.sciencedirect.com/science/article/pii/S0019103516302226 doi: https://doi.org/10.1016/j.icarus.2016.05.027

Christou, A. A. (2004). Prospects for meteor shower activity in the venusian atmosphere. *Icarus*, *168*(1), 23-33. Retrieved from https://www.sciencedirect.com/science/article/pii/S0019103503004275 doi: https://doi.org/10.1016/j.icarus.2003.12.006

Coffeen, D. L., & Gehrels, T. (1969, April). Wavelength Dependence of Polarization. XV. Observations of Venus. AJ, *74*, 433. doi: 10.1086/110822

Cook, A. F., Duxbury, T. C., & Hunt, G. E. (1979). First results on jovian lightning. *Nature*, *280*(5725), 794–794. Retrieved from https://doi.org/10.1038/280794a0 doi: 10.1038/280794a0

Daniels, J. T. M., Russell, C. T., Strangeway, R. J., Wei, H. Y., & Zhang, T. L. (2012, April). Whistler mode bursts in the Venus ionosphere due to lightning: Statistical properties using Venus Express magnetometer observations. *Journal of Geophysical Research (Planets)*, *117*(E4), E04004. doi: 10.1029/2011JE003897

Dyudina, U. A., Del Genio, A. D., Ingersoll, A. P., Porco, C. C., West, R. A., Vasavada, A. R., & Barbara, J. M. (2004, November). Lightning on Jupiter observed in the H_α line by the Cassini imaging science subsystem. *Icarus*, *172*(1), 24-36. doi: 10.1016/j.icarus.2004.07.014

Dyudina, U. A., Ingersoll, A. P., Vasavada, A. R., Ewald, S. P., & Galileo SSI Team. (2002, December). Monte Carlo Radiative Transfer Modeling of Lightning Observed in Galileo Images of Jupiter. *Icarus*, *160*(2), 336-349. doi: 10.1006/icar.2002.6977

Gibbard, S., Levy, E. H., & Lunine, J. I. (1995, December). Generation of lightning in Jupiter's water cloud. Nature, *378*(6557), 592-595. doi: 10.1038/378592a0

Gierasch, P. J., Ingersoll, A. P., Banfield, D., Ewald, S. P., Helfenstein, P., Simon-Miller, A., ... Team, G. I. (2000). Observation of moist convection in jupiter's atmosphere.

Nature, *403*(6770), 628–630. Retrieved from https://doi.org/10.1038/35001017 doi: 10.1038/35001017
Giles, R. S., Greathouse, T. K., Bonfond, B., Gladstone, G. R., Kammer, J. A., Hue, V., ... Levin, S. M. (2020). Possible transient luminous events observed in jupiter's upper atmosphere. *Journal of Geophysical Research: Planets*, *125*(11), e2020JE006659. Retrieved from https://agupubs.onlinelibrary.wiley.com/doi/abs/10.1029/2020JE006659 (e2020JE006659 2020JE006659) doi: https://doi.org/10.1029/2020JE006659
Gouda, S. (2014). **惑星観測用大気揺らぎ補償光学系のための惑星表面模様の相関追跡による波面測定方法の研究** (Master thesis). Department of Cosmosciences, Graduate School of Science, Hokkaido University.
Gurnett, D. A., Kurth, W. S., Roux, A., Gendrin, R., Kennel, C. F., & Bolton, S. J. (1991). Lightning and plasma wave observations from the galileo flyby of venus. *Science*, *253*(5027), 1522-1525. Retrieved from https://www.science.org/doi/abs/10.1126/science.253.5027.1522 doi: 10.1126/science.253.5027.1522
Gurnett, D. A., Zarka, P., Manning, R., Kurth, W. S., Hospodarsky, G. B., Averkamp, T. F., ... Farrell, W. M. (2001). Non-detection at venus of high-frequency radio signals characteristic of terrestrial lightning. *Nature*, *409*(6818), 313–315. Retrieved from https://doi.org/10.1038/35053009 doi: 10.1038/35053009
Hansell, S. A., Wells, W. K., & Hunten, D. M. (1995, October). Optical detection of lightning on Venus. Icarus, *117*(2), 345-351. doi: 10.1006/icar.1995.1160
Hansen, J. E., & Travis, L. D. (1974, October). Light scattering in planetary atmospheres. Space Sci. Rev., *16*(4), 527-610. doi: 10.1007/BF00168069
Hartmann, D. L., Gasparini, B., Berry, S. E., & Blossey, P. N. (2018). The life cycle and net radiative effect of tropical anvil clouds. *Journal of Advances in Modeling Earth Systems*, *10*(12), 3012-3029. Retrieved from https://agupubs.onlinelibrary.wiley.com/doi/abs/10.1029/2018MS001484 doi: https://doi.org/10.1029/2018MS001484
Haus, R., Kappel, D., & Arnold, G. (2013). Self-consistent retrieval of temperature profiles and cloud structure in the northern hemisphere of venus using virtis/vex and pmv/venera-15 radiation measurements. *Planetary and Space Science*, *89*, 77-101. Retrieved from https://www.sciencedirect.com/science/article/pii/S0032063313002596 doi: https://doi.org/10.1016/j.pss.2013.09.020
Haus, R., Kappel, D., & Arnold, G. (2014). Atmospheric thermal structure and cloud features in the southern hemisphere of venus as retrieved from virtis/vex radiation measurements. *Icarus*, *232*, 232-248. Retrieved from https://www.sciencedirect.com/science/article/pii/S0019103514000517 doi: https://doi.org/10.1016/j.icarus.2014.01.020
Haus, R., Kappel, D., & Arnold, G. (2015, January). Lower atmosphere minor gas abundances as retrieved from Venus Express VIRTIS-M-IR data at 2.3 μm. Planet. Space Sci., *105*, 159-174. doi: 10.1016/j.pss.2014.11.020
Hodosán, G., Helling, C., & Vorgul, I. (2021). Exploring terrestrial lightning parameterisations for exoplanets and brown dwarfs.

Planetary and Space Science, *204*, 105247. Retrieved from https://www.sciencedirect.com/science/article/pii/S0032063321000866 doi: https://doi.org/10.1016/j.pss.2021.105247

Imai, M., Kolmašová, I., Kurth, W. S., Santolík, O., Hospodarsky, G. B., Gurnett, D. A., ... Levin, S. M. (2019, June). Evidence for low density holes in Jupiter's ionosphere. *Nature Communications*, *10*, 2751. doi: 10.1038/s41467-019-10708-w

Imai, M., Santolík, O., Brown, S. T., Kolmašová, I., Kurth, W. S., Janssen, M. A., ... Levin, S. M. (2018, August). Jupiter Lightning-Induced Whistler and Sferic Events With Waves and MWR During Juno Perijoves. Geophys. Res. Lett., *45*(15), 7268-7276. doi: 10.1029/2018GL078864

Imai, M., Wong, M. H., Kolmašová, I., Brown, S. T., Santolík, O., Kurth, W. S., ... Levin, S. M. (2020, August). High-Spatiotemporal Resolution Observations of Jupiter Lightning-Induced Radio Pulses Associated With Sferics and Thunderstorms. Geophys. Res. Lett., *47*(15), e88397. doi: 10.1029/2020GL088397

Karyu, H., Kuroda, T., Imamura, T., Terada, N., Vandaele, A. C., Mahieux, A., & Viscardy, S. (2024, mar). One-dimensional microphysics model of venusian clouds from 40 to 100 km: Impact of the middle-atmosphere eddy transport and soir temperature profile on the cloud structure. *The Planetary Science Journal*, *5*(3), 57. Retrieved from https://dx.doi.org/10.3847/PSJ/ad25f3 doi: 10.3847/PSJ/ad25f3

Kattawar, G. W. (1975). A three-parameter analytic phase function for multiple scattering calculations. *Journal of Quantitative Spectroscopy and Radiative Transfer*, *15*(9), 839-849. Retrieved from https://www.sciencedirect.com/science/article/pii/0022407375900953 doi: https://doi.org/10.1016/0022-4073(75)90095-3

Knollenberg, R. G., & Hunten, D. M. (1980). The microphysics of the clouds of venus: Results of the pioneer venus particle size spectrometer experiment. *Journal of Geophysical Research: Space Physics*, *85*(A13), 8039-8058. Retrieved from https://agupubs.onlinelibrary.wiley.com/doi/abs/10.1029/JA085iA13p08039 doi: https://doi.org/10.1029/JA085iA13p08039

Kokhanovsky, A. (2004). Optical properties of terrestrial clouds. *Earth-Science Reviews*, *64*(3), 189-241. Retrieved from https://www.sciencedirect.com/science/article/pii/S0012825203000424 doi: https://doi.org/10.1016/S0012-8252(03)00042-4

Kolmašová, I., Imai, M., Santolík, O., Kurth, W. S., Hospodarsky, G. B., Gurnett, D. A., ... Bolton, S. J. (2018). Discovery of rapid whistlers close to jupiter implying lightning rates similar to those on earth. *Nature Astronomy*, *2*(7), 544–548. Retrieved from https://doi.org/10.1038/s41550-018-0442-z doi: 10.1038/s41550-018-0442-z

Kolmašová, I., Santolík, O., Imai, M., Kurth, W. S., Hospodarsky, G. B., Connerney, J. E. P., ... Lán, R. (2023, May). Lightning at Jupiter pulsates with a similar rhythm as in-cloud lightning at Earth. *Nature Communications*, *14*, 2707. doi: 10.1038/s41467-023-38351-6

Krasnopolskii, V. A. (1983). Venus spectroscopy in the 3000 - 8000 Å region by Veneras 9 and 10. In D. M. Hunten, L. Colin, T. M. Donahue, & V. I. Moroz (Eds.), *Venus* (p. 459-483).

Krasnopolsky, V. (1983). Lightnings and nitric oxide on venus.

Planetary and Space Science, *31*(11), 1363-1369. Retrieved from https://www.sciencedirect.com/science/article/pii/0032063383900727 doi: https://doi.org/10.1016/0032-0633(83)90072-7

Ksanfomaliti, L., Vasilchikov, N., Canpantzerova, O., Petrova, E., Suvorov, A., Filippov, G., ... Yabrova, L. (1980). Electrical discharges in the venusian atmosphere. In M. Rycroft (Ed.), *Space research* (Vol. 20, p. 223-226). Pergamon. Retrieved from https://www.sciencedirect.com/science/article/pii/S0964274913600463 doi: https://doi.org/10.1016/S0964-2749(13)60046-3

Ksanfomaliti, L. V., Scarf, F. L., & Taylor, W. W. L. (1983). The electrical activity of the atmosphere of Venus. In D. M. Hunten, L. Colin, T. M. Donahue, & V. I. Moroz (Eds.), *Venus* (p. 565-603).

Ksanfomaliti, L. V., Vasilchikov, N. M., Goroshkova, N. V., Petrova, E. V., Suvorov, A. P., & Khondyrev, V. K. (1982, August). The low-frequency electromagnetic field in the Venus atmosphere - Evidence from Venera 13 and Venera 14. *Pisma v Astronomicheskii Zhurnal*, *8*, 424-428.

Ksanfomality, L. V. (2024, March). Lightning Flares in the Cloud Layer of Venus Detected in the Near-Infrared Range. *Cosmic Research*, *62*(1), 60-72. doi: 10.1134/S001095252370082X

Kumar, V. R. D., Pabari, J. P., Acharyya, K., & Russell, C. T. (2021, September). Venus lightning: Estimation of charge and dimensions of charge regions for lightning initiation. Icarus, *365*, 114473. doi: 10.1016/j.icarus.2021.114473

Light, T. E., Suszcynsky, D. M., Kirkland, M. W., & Jacobson, A. R. (2001). Simulations of lightning optical waveforms as seen through clouds by satellites. *Journal of Geophysical Research: Atmospheres*, *106*(D15), 17103-17114. Retrieved from https://agupubs.onlinelibrary.wiley.com/doi/abs/10.1029/2001JD900051 doi: https://doi.org/10.1029/2001JD900051

LIN, X., JIANG, T., ZHANG, W., ZHENG, X., CUI, M., & FAN, N. (2025). Lightning activity in the outer rainbands of typhoon doksuri（2023）and its relationship with the microphysical structure of heavy rainfall. *Acta Meteorologica Sinica*, *83*(1), 80-95. Retrieved from https://www.sciopen.com/article/10.11676/qxxb2025.20240057 doi: 10.11676/qxxb2025.20240057

Little, B., Anger, C. D., Ingersoll, A. P., Vasavada, A. R., Senske, D. A., Breneman, H. H., ... Galileo SSI Team (1999, December). Galileo Images of Lightning on Jupiter. Icarus, *142*(2), 306-323. doi: 10.1006/icar.1999.6195

Luque, A., Gordillo-Vázquez, F. J., & Pallé, E. (2015, May). Ground-based search for lightning in Jupiter with GTC/OSIRIS fast photometry and tunable filters. A&A, *577*, A94. doi: 10.1051/0004-6361/201425406

Luque, A., José Gordillo-Vázquez, F., Li, D., Malagón-Romero, A., Pérez-Invernón, F. J., Schmalzried, A., ... Østgaard, N. (2020, November). Modeling lightning observations from space-based platforms (CloudScat.jl 1.0). *Geoscientific Model Development*, *13*(11), 5549-5566. doi: 10.5194/gmd-13-5549-2020

Maggio, C. R., Marshall, T. C., & Stolzenburg, M. (2009). Estimations of charge transferred and energy released by lightning flashes. *Journal of Geophysical Research: Atmospheres*, *114*(D14). Retrieved from https://agupubs.onlinelibrary.wiley.com/doi/abs/10.1029/2008JD011506 doi: https://doi.org/10.1029/2008JD011506

Michael, M., Tripathi, S. N., Borucki, W. J., & Whitten, R. C. (2009). Highly charged cloud particles in the atmosphere of venus. *Journal of Geophysical Research: Planets*, *114*(E4). Retrieved from https://agupubs.onlinelibrary.wiley.com/doi/abs/10.1029/2008JE003258 doi: https://doi.org/10.1029/2008JE003258

Morrison, H., van Lier-Walqui, M., Fridlind, A. M., Grabowski, W. W., Harrington, J. Y., Hoose, C., … Xue, L. (2020). Confronting the challenge of modeling cloud and precipitation microphysics. *Journal of Advances in Modeling Earth Systems*, *12*(8), e2019MS001689. Retrieved from https://agupubs.onlinelibrary.wiley.com/doi/abs/10.1029/2019MS001689 (e2019MS001689 2019MS001689) doi: https://doi.org/10.1029/2019MS001689

Niemann, H. B., Atreya, S. K., Carignan, G. R., Donahue, T. M., Haberman, J. A., Harpold, D. N., … Way, S. H. (1998, September). The composition of the Jovian atmosphere as determined by the Galileo probe mass spectrometer. J. Geophys. Res., *103*(E10), 22831-22846. doi: 10.1029/98JE01050

Park, S.-Y., Lim, K.-S. S., Kim, K., Lee, G., & Milbrandt, J. A. (2024). Introducing graupel density prediction in weather research and forecasting (wrf) double-moment 6-class (wdm6) microphysics and evaluation of the modified scheme during the ice-pop field campaign. *Geoscientific Model Development*, *17*(18), 7199–7218. Retrieved from https://gmd.copernicus.org/articles/17/7199/2024/ doi: 10.5194/gmd-17-7199-2024

Peck, E. R., & Reeder, K. (1972, Aug). Dispersion of air. *J. Opt. Soc. Am.*, *62*(8), 958–962. doi: 10.1364/JOSA.62.000958

Pérez-Invernón, F. J., Luque, A., & Gordillo-Vázquez, F. J. (2017, July). Three-dimensional modeling of lightning-induced electromagnetic pulses on Venus, Jupiter, and Saturn. *Journal of Geophysical Research (Space Physics)*, *122*(7), 7636-7653. doi: 10.1002/2017JA023989

Quick, M. G., & Krider, E. P. (2013). Optical power and energy radiated by natural lightning. *Journal of Geophysical Research: Atmospheres*, *118*(4), 1868-1879. Retrieved from https://agupubs.onlinelibrary.wiley.com/doi/abs/10.1002/jgrd.50182 doi: https://doi.org/10.1002/jgrd.50182

Rinnert, K., & Lanzerotti, L. J. (1998). Radio wave propagation below the jovian ionosphere. *Journal of Geophysical Research: Planets*, *103*(E10), 22993-22999. Retrieved from https://agupubs.onlinelibrary.wiley.com/doi/abs/10.1029/98JE01968 doi: https://doi.org/10.1029/98JE01968

Rinnert, K., Lanzerotti, L. J., Uman, M. A., Dehmel, G., Gliem, F. O., Krider, E. P., & Bach, J. (1998). Measurements of radio frequency signals from lightning in jupiter's atmosphere. *Journal of Geophysical Research: Planets*, *103*(E10), 22979-22992. Retrieved from https://agupubs.onlinelibrary.wiley.com/doi/abs/10.1029/98JE00830 doi: https://doi.org/10.1029/98JE00830

Rostami, M., Fallah, B., & Fazel-Rastgar, F. (2025). Dynamics of jupiter's equatorial zone: Instability analysis and a mechanism for y-shaped structures. *Icarus*, *429*, 116414. Retrieved from https://www.sciencedirect.com/science/article/pii/S0019103524004743 doi: https://doi.org/10.1016/j.icarus.2024.116414

Russell, C., Zhang, T., Strangeway, R., Wei, H., Delva, M., & Magnes, W. (2008). Electromagnetic waves observed by venus express at periapsis: Detection and analysis techniques. *Advances in Space Research*, *41*(1), 113-117. Retrieved from https://www.sciencedirect.com/science/article/pii/S0273117707009295 doi: https://doi.org/10.1016/j.asr.2007.08.032

Russell, C. T. (1991). Venus lightning. *Space Science Reviews*, *55*(1), 317–356. Retrieved from https://doi.org/10.1007/BF00177140 doi: 10.1007/BF00177140

Russell, C. T., Luhmann, J. G., Cravens, T. E., Nagy, A. F., & Strangeway, R. J. (2007). Venus upper atmosphere and plasma environment: Critical issues for future exploration. In *Exploring venus as a terrestrial planet* (p. 139-156). American Geophysical Union (AGU). Retrieved from https://agupubs.onlinelibrary.wiley.com/doi/abs/10.1029/176GM09 doi: https://doi.org/10.1029/176GM09

Ryohei Misumi, K. M. (2008). Effects of low-level convergence on convective precipitation: numerical study with special attention to the role of low-level clouds. *The Meteorological Society of Japan (MSJ)*, *55*((7)), 567-580.

Sagdeev, R. Z., Linkin, V. M., Kerzhanovich, V. V., Lipatov, A. N., Shurupov, A. A., Blamont, J. E., ... Selivanov, A. S. (1986). Overview of vega venus balloon in situ meteorological measurements. *Science*, *231*(4744), 1411-1414. Retrieved from https://www.science.org/doi/abs/10.1126/science.231.4744.1411 doi: 10.1126/science.231.4744.1411

Salut, M. M., Cohen, M. B., Ali, M. A. M., Graf, K. L., Cotts, B. R. T., & Kumar, S. (2013). On the relationship between lightning peak current and early vlf perturbations. *Journal of Geophysical Research: Space Physics*, *118*(11), 7272-7282. Retrieved from https://agupubs.onlinelibrary.wiley.com/doi/abs/10.1002/2013JA019087 doi: https://doi.org/10.1002/2013JA019087

Sato, M., Ushio, T., Morimoto, T., Kikuchi, M., Kikuchi, H., Adachi, T., ... Kawasaki, Z. I. (2015, May). Overview and early results of the Global Lightning and Sprite Measurements mission. *Journal of Geophysical Research (Atmospheres)*, *120*(9), 3822-3851. doi: 10.1002/2014JD022428

Scarf, F. L., Jordan, K. F., & Russell, C. T. (1987). Distribution of whistler mode bursts at venus. *Journal of Geophysical Research: Space Physics*, *92*(A11), 12407-12411. Retrieved from https://agupubs.onlinelibrary.wiley.com/doi/abs/10.1029/JA092iA11p12407 doi: https://doi.org/10.1029/JA092iA11p12407

Scarf, F. L., Taylor, W. W. L., Russell, C. T., & Brace, L. H. (1980). Lightning on venus: Orbiter detection of whistler signals. *Journal of Geophysical Research: Space Physics*, *85*(A13), 8158-8166. Retrieved from https://agupubs.onlinelibrary.wiley.com/doi/abs/10.1029/JA085iA13p08158 doi: https://doi.org/10.1029/JA085iA13p08158

Sugiyama, K., Nakajima, K., Odaka, M., Kuramoto, K., & Hayashi, Y. Y. (2014, February). Numerical simulations of Jupiter's moist convection layer: Structure and dynamics in statistically steady states. Icarus, *229*, 71-91. doi: 10.1016/j.icarus.2013.10.016

Takagi, S., Mahieux, A., Wilquet, V., Robert, S., Vandaele, A. C., & Iwagami, N. (2019). An uppermost haze layer above 100 km found over venus by the soir instrument onboard venus express. *Earth, Planets and Space*, *71*(1), 124. Retrieved from `https://doi.org/10.1186/s40623-019-1103-x` doi: 10.1186/s40623-019-1103-x

Takahashi, Y., Imai, M., Sato, M., & Lorenz, R. D. (2020, December). Optical flash in Venus observed by LAC onboard AKATSUKI. In *Agu fall meeting abstracts* (Vol. 2020, p. AE002-05).

Takahashi, Y., Yoshida, J., Yair, Y., Imamura, T., & Nakamura, M. (2008). Lightning detection by lac onboard the japanese venus climate orbiter, planet-c. *Space Science Reviews*, *137*(1), 317–334. Retrieved from `https://doi.org/10.1007/s11214-008-9400-x` doi: 10.1007/s11214-008-9400-x

Thomson, L. W., & Krider, E. P. (1982). The effects of clouds on the light produced by lightning. *Journal of Atmospheric Sciences*, *39*(9), 2051 - 2065. doi: 10.1175/1520-0469(1982)039¡2051:TEOCOT¿2.0.CO;2

Tomasko, M., West, R., & Castillo, N. (1978). Photometry and polarimetry of jupiter at large phase angles: I. analysis of imaging data of a prominent belt and a zone from pioneer 10. *Icarus*, *33*(3), 558-592. Retrieved from `https://www.sciencedirect.com/science/article/pii/0019103578901914` doi: https://doi.org/10.1016/0019-1035(78)90191-4

Tsang, C., Taylor, F., Wilson, C., Liddell, S., Irwin, P., Piccioni, G., ... Calcutt, S. (2009). Variability of co concentrations in the venus troposphere from venus express/virtis using a band ratio technique. *Icarus*, *201*(2), 432-443. Retrieved from `https://www.sciencedirect.com/science/article/pii/S0019103509000104` doi: https://doi.org/10.1016/j.icarus.2009.01.001

Wilkman, O. (2013, September). *Miescatter.jl.* Retrieved 14 October 2015, from `https://github.com/dronir/MieScatter.jl`

Wong, M. H., Orton, G. S., de Pater, I., Simon, A. A., & Stephens, A. W. (2019, September). High-resolution UV/optical/IR imaging of Jupiter in 2016-2019 with HST/WFC3 and Gemini/NIRI. In *Epsc-dps joint meeting 2019* (Vol. 2019, p. EPSC-DPS2019-165).

Yair, Y., Levin, Z., & Tzivion, S. (1995, June). Lightning generation in a Jovian thundercloud: Results from an axisymmetric numerical cloud model. Icarus, *115*(2), 421-434. doi: 10.1006/icar.1995.1108

You, J., Zheng, D., Zhang, Y., Yao, W., & Meng, Q. (2019). Duration, spatial size and radiance of lightning flashes over the asia-pacific region based on trmm/lis observations. *Atmospheric Research*, *223*, 98-113. Retrieved from `https://www.sciencedirect.com/science/article/pii/S0169809518310846` doi: https://doi.org/10.1016/j.atmosres.2019.03.013